Università degli Studi di Padova

Department of Mathematics "Tullio Levi-Civita"
Doctoral Program in Mathematics
Curriculum: Mathematics
(Cycle XXXIV)

Ph.D. Thesis

Flow-type dependence and simulation techniques for non-Newtonian complex fluids

Coordinator
Ch.mo Prof. Giovanni Colombo

Supervisor
Dott. Giulio Giuseppe Giusteri

Candidate
Francesca Tedeschi

Abstract

This work is devoted to the investigation of planar flows of complex fluids in non specific geometries through techniques of computer simulation.

Firstly, we developed a new heterogeneous multi-scale method that combines micro-scale data from Non-Equilibrium Molecular Dynamics (NEMD) with a macro-scale CFD solver to achieve a data-driven prediction of complex non-uniform planar flows in macroscopic complex geometries. The microscopic data were employed to reconstruct the stress tensor that determines the evolution associated with the equations of motion at the macroscopic level. At the continuum level, the method is model-free, since the Cauchy stress tensor is determined locally in space and time from NEMD data. The modelling effort is thus limited to the identification of suitable interaction potentials at the micro-scale. The method has been tested successfully onto three paradigmatic flows of polymeric fluids: the straight channel, the contraction 4:1 and the flow past a deep hole. However, it is applicable only when the time-scale of changes in the local state of a fluid element is greater than the microscopic relaxation time necessary to achieve a statistically steady state of the molecular conformation and interactions. Compared to previous proposals, our approach takes into account the fact that the material response of polymeric fluids can depend strongly on the local flow type and we show that this is a necessary feature to correctly capture the macroscopic dynamics.

Secondly, we have been able to extend reproducibility conditions of a lattice of points in $\mathbb{R}^2$ under planar extension (found by Kraynik & Reinelt [38]) to the case of mixed flows (combination of simple shear and extension). These conditions are linked to the possibility of extending indefinitely the time duration of the simulation and this is very important to be able to extract steady properties of the system. It results that, for each fixed homogeneous mixed flow, we must take a specific orientation and aspect ratio for the simulation box to display the periodic behavior. In correspondence to the time period, the simulation box can be re-initialized without loosing any meaningful physical property.

Thirdly, the algorithm has been successfully implemented in the `PMF` software package, written in C++ and devoted to NEMD simulations of Planar Mixed Flows in `LAMMPS`

(Large-scale Atomic/Molecular Massively Parallel Simulator). We also managed to carry out a complete set of simulations of mixed motions and, for this reason, the software can be a reliable tool for exploring the rheological properties of this class of flows.

Sommario

Questo lavoro è dedicato all'indagine dei flussi planari di fluidi complessi in geometrie non specifiche attraverso tecniche di simulazione computazionali.

In primo luogo, abbiamo sviluppato un nuovo metodo multiscala eterogeneo che accoppia i dati su microscala della Dinamica Molecolare Non all'Equilibrio (NEMD) con un solutore CFD su macroscala per ottenere una previsione data-driven di flussi planari complessi non uniformi in geometrie macroscopiche complesse. A livello del continuo, il metodo è privo di modello, poiché il tensore di Cauchy che determina l'evoluzione del moto è determinato localmente nello spazio e nel tempo dai dati NEMD. Lo sforzo di modellazione è quindi limitato all'identificazione dei potenziali di interazione adatti alla microscala. Il metodo è stato testato con successo su tre flussi paradigmatici di fluidi polimerici: il canale, la contrazione 4:1 e il flusso oltre un foro profondo. Tuttavia, è applicabile solo quando la scala temporale dei cambiamenti dello stato locale di un elemento fluido è maggiore del tempo di rilassamento microscopico necessario per ottenere uno stato della conformazione molecolare e delle interazioni statisticamente stazionario. Rispetto alle proposte precedenti, il nostro approccio tiene conto del fatto che la risposta dei fluidi polimerici può dipendere fortemente dal tipo di flusso locale e dimostriamo che questa è una caratteristica necessaria per catturare correttamente la dinamica macroscopica.

In secondo luogo, abbiamo esteso le condizioni di riproducibilità di un reticolo di punti in $\mathbb{R}^2$ sottoposto ad estensione planare (trovate da Kraynik & Reinelt [38]) al caso dei flussi misti (combinazione di simple shear ed estensione). Queste condizioni sono legate alla possibilità di estendere indefinitamente la durata temporale della simulazione e questo è molto importante per poter estrarre proprietà stazionarie del sistema. Risulta che, per ogni flusso misto fissato, dobbiamo prendere un orientazione e un rapporto d'aspetto specifico per la scatola di simulazione al fine di visualizzare un suo comportamento periodico. In corrispondenza del periodo, la scatola viene reinizializzata senza perdere alcuna proprietà fisica significativa.

In terzo luogo, l'algoritmo è stato implementato con successo nel pacchetto software `PMF`, scritto in C++ e dedicato alle simulazioni NEMD di Flussi Planari Misti in `LAMMPS` (Large-scale Atomic/Molecular Massively Parallel Simulator). Siamo anche riusciti a re-

alizzare una serie completa di simulazioni significative di moti misti e, per questo motivo, il software può essere uno strumento affidabile per esplorare le proprietà reologiche di questa classe di flussi.

Contents

Introduction **1**

1 Complex flows and complex fluids **7**

1.1 Mathematical framework . . . 9

1.1.1 Conservation of mass and incompressibility . . . 10

1.1.2 Equations of motion . . . 11

1.2 Rheological properties . . . 14

1.2.1 Viscosity . . . 15

1.2.2 Normal Stress Differences . . . 16

1.2.3 Extensional Flows . . . 18

1.2.4 Mixed Flows . . . 19

2 Kinematics and constitutive laws **21**

2.1 Velocity gradient and flow classification . . . 22

2.2 Classical constitutive laws . . . 25

2.2.1 Ideal Fluid . . . 25

2.2.2 Reiner-Rivlin fluids . . . 25

2.2.3 Second order fluids . . . 27

2.3 New decomposition of the stress . . . 28

2.3.1 New material functions . . . 30

2.4 Advantages of new material functions . . . 35

3 Non-Equilibrium Molecular Dynamics **37**

3.1 Basics of MD . . . 38

3.1.1 Interaction potentials . . . 40

3.1.2 Initialization . . . 41

3.2 Ensembles . . . 42

3.3 Periodic Boundary Conditions (PBCs) . . . 43

3.3.1 PBCs in simple shear and extensional flows . . . 44

3.4 Reproducibility and compatibility . . . 48
3.5 Force calculation . . . 50
3.6 Integration of the equations of motion . . . 51
3.7 Computation of the stress . . . 52

4 NEMD in mixed flows **53**
4.1 The velocity gradient in the flow frame . . . 55
4.1.1 The evolution operator . . . 58
4.2 PBCs for planar mixed motions . . . 59
4.2.1 Reproducibility condition . . . 59
4.2.2 Parameters for mixed flows . . . 62
4.3 PMF: a LAMMPS package for Planar Mixed Flows . . . 67
4.3.1 QR decomposition for the simulation box . . . 68
4.3.2 Implementation issues . . . 69
4.4 User's Guide for the USER-PMF package . . . 71
4.4.1 Contents . . . 72
4.4.2 Usage . . . 73
4.4.3 fix nvt/pmf . . . 73
4.4.4 compute temp/pmf . . . 74
4.4.5 compute pressure/pmf . . . 74
4.4.6 dump cfg/pmf . . . 75
4.4.7 Implementation details . . . 76
4.4.8 Error and Warning Messages . . . 76

5 The multiscale method **77**
5.1 Micro-scale data and macro-scale simulations . . . 78
5.2 Micro-scale NEMD simulation . . . 79
5.2.1 Interaction potentials . . . 80
5.2.2 Average stress coefficients . . . 80
5.3 Fitting procedure for the micro-scale NEMD data . . . 83
5.3.1 Data-driven material functions . . . 84
5.4 Macro-scale simulation . . . 85
5.5 Multi-scale coupling in the code . . . 86
5.6 Numerical results for different geometries . . . 89
5.6.1 Channel flow . . . 90
5.6.2 Flow through a contraction . . . 91
5.6.3 Flow past a deep hole . . . 92
5.7 An analytical solution . . . 93

6 NEMD simulations with PMF package **105**
6.1 Settings 105
6.2 Average stress coefficients 106
6.2.1 Viscosity and reorientation of eigenvectors 106
6.2.2 The other coefficients 108

7 Conclusions **111**

Bibliography **113**

Introduction

Complex fluids, such as suspensions of hard particles in a Newtonian solvent or polymeric melts, often reveal *non-Newtonian* effects such as viscoelasticity, shear-thinning or shear-thickening behavior of viscosity with respect to the velocity of the deformation.

Viscoelasticity is the property of a material to behave as elastic solid or as viscous fluid, depending on temperature, shear rate or time scale of observation. Polymeric solutions are typically viscoelastic because of the presence of elastic chains that elongate, tumble and realign, depending on the condition of flow, breaking the linearity in the stress-strain relation of the Newtonian case. Another non-Newtonian phenomenon is the non-constant viscosity: for low values of the shear rate the particles tend to orientate in the direction of the flow, structuring partially, and causing the decreasing of the viscosity (*shear-thinning*) at low concentrations. For high values of the shear rate and volume fractions of the dispersed phase near the jamming point (critical value), the elastic structures tend to form clusters much more structured and the viscosity increases (*shear-thickening*). So, the molecular structure of the fluid is modified in different ways according to the type of flow: shear motion with its rotatory component encourages the aggregation and disaggregation of particles, elongation instead promotes the orientation in the direction of the extension. For this reason it is important to study also the local rheology and the microscopic changes, to understand the macroscopic response of these fluids to applied forces. We are going to restrict the field of our investigation to fluids which are, to a good extent, incompressible, thus liquids and to mention, firstly, their main rheological properties, called *material functions*, in simple shear (*shear viscosity* η and *Normal Stress Differences* N_1 and N_2) and in the extension flow (*extensional viscosity* η_E). In Chapter 1 we are going to illustrate the main rheological properties of non-Newtonian fluids in a mathematical approach.

The class of *Newtonian* fluids represents a good approximation for some substances such as water, air and plasma in the blood in several relaxed conditions of flow (large arteries, wide tubes, ...). Material functions have classically been extracted and observed in the, so called, *viscometric flows*, i.e. with velocity gradient locally equivalent to that of a simple shear. In recent decades, extensional flows have acquired more and

more importance for the rheological characterization of complex fluids. However, *simple flows* turn out to be only mathematical idealizations of the reality because they are often completely uniform and develop in regular geometries. Real processes, instead, occur in flow geometries that are rarely regular: they often have restrictions, holes, barriers, obstructions, deviations, angles and this gives rise to complex flows characterized by regions with different flow-types and non-homogeneous velocity gradients, hard to investigate and classify. For this reason, we are interested in studying properties of complex fluids under generic flow conditions and it becomes necessary to develop techniques able to take into account the flow-type dependence of the response of the fluid through the stress tensor to applied pressure gradients.

In the characterization of fluids and the construction of macroscopic models, rheology, as the science that investigates (both computationally and experimentally) properties of materials (both solids and liquids) under deformations and flows, helps us. In recent years, numerical methods are becoming increasingly common in the investigation of fluids, because they make it possible to go beyond the typical limits of laboratory experiments and to obtain data even under conditions that are difficult to reproduce in the laboratory, in a much shorter time, see Crochet [9] for a discussion on numerical methods for complex fluids.

Regarding fluids and deformable systems, the relevant kinematic information are encoded in the derivatives of the velocity $\boldsymbol{u}$. In this discussion we start by considering only the first derivative, the *velocity gradient tensor* $\nabla \boldsymbol{u}$, representing it in a frame–invariant form through the eigenvectors of its symmetric part, the strain rate tensor, $\mathbf{D}$, as illustrated in Chapter 2. The local kinematics of the fluid in planar flows turns out to be described by two parameters: the *rate of strain* $\dot{\varepsilon}$ and the *out-of-flow component of the vorticity* β_3. The parameter β_3 detects the presence of rotational components in the flow, thus our classification of planar flows will be made on its basis. In particular, $|\beta_3| = 0$ corresponds to extensional planar motion, $|\beta_3| = 1$ to a simple shear and $|\beta_3| \to \infty$ to rotational rigid motions, where intermediate values of $|\beta_3|$ are associated to mixed flow-types.

Then, the rigorous mathematical link between the kinematic and the dynamic state of the fluid is given through the constitutive law for the *Cauchy stress tensor* $\boldsymbol{\sigma}$, appearing in the equation of motion of the fluid. It quantifies the internal stresses that are generated on a fluid element as a consequence of external actions. We give a brief and not exhaustive overview of classical choices in literature on *constitutive laws* illustrating Ideal, Newtonian, Power-law, Reiner–Rivlin and Second order fluids.

However, for the realization of this study we deviate from classical representations and we prefer to use a *data-driven approach*, without postulating any "a priori" constitutive

laws. We make use of the decomposition of the stress illustrated in Giusteri & Seto [25] (and in Chapter 2) to project and organize microscopic data that are used to reconstruct the stress at the macroscopic level, in a way that we explain in detail in Chapter 2 and Chapter 5.

This decomposition gives a mechanically invariant (with respect to the reference system) meaning to the various terms, thus it has a tensor-type form. The stress tensor is here represented by a linear combination of basis tensors built starting from $\mathbf{D}$. This decomposition is adaptable to any flow and to any fluid in every geometry. It is a local representation both in time and space, because depends on the eigenvectors of $\mathbf{D}$ that are changing in time and in every point. But the representation of each basis tensor is the same at any time in any point. The model requires only that $\mathbf{D}$ is non-zero.

Microscopic data are retrieved thanks to *Molecular Dynamics* (MD) simulations, a widely used technique to compute equilibrium and transport properties of many-body systems. The particles that make up the system obey to the laws of classical mechanics, for example Newton's second law where the acting forces are empirical forces, deriving from suitable interaction potential functions. The mainly used interaction potentials are the classical Lennard Jones (LJ) potential, the Weeks-Chandler-Andersen potential (WCA), which takes only the repulsive part of LJ, and the FENE (Finitely Extensible Nonlinear Elastic) potential for elastic covalent bonds. More details on basic notions on MD are reported in Chapter 3. We made NEMD (Non-Equilibrium Molecular Dynamics) simulations with a coupling between the WCA and the FENE potential to model polymers as bead-spring systems. The MD simulation of motion is conducted in the main or primitive box, which is surrounded by periodic copies of itself (called *images*) to achieve a representation of the *bulk flow*. This technique is called Periodic Boundary Conditions (PBCs).

In our NEMD simulations the flow is applied with a deformation of the box through its boundaries. At each timestep we compute interacting forces on each particle that belongs to the main cell, using all the particles that fall in the interaction radius, also image particles, if it is necessary.

Once forces are computed for all particles in the main box, the program proceeds with the integration of the equations of motion. Particles obey to Newton's second law, but we make use of another formulation, called SLLOD, in which we consider the velocity relative to the streaming velocity, instead of the actual one. Daivis and Todd [10] proved the validity of this equations in the entire class of homogeneous flows, and not only for simple shear motion. Usually these equations are coupled with a thermostat that is needed to keep the average temperature around a chosen value, allowing to simulate the flow in the desired statistical ensemble.

When a situation is reached in which the measured average properties of the system no longer vary with time, we are in the steady state. And for example, the microscopic pressure tensor at steady state is calculated with the virial theorem. It also happens that if N is sufficiently large the statistics observed is independent of N and of the periodicity.

In Chapter 5, we show our NEMD results that reproduce and extend published data of the research group of the University of Mainz, reported in Stalter *et al* [56]. We collected microscopic data about mean flow quantities in a simple shear motion using `LAMMPS` (Large-scale Atomic/Molecular Massively Parallel Simulator), a well-known molecular dynamics parallel simulator. However, data obtained are of limited applicability because few motions are local shear and it appeared necessary to study types of flow other than simple shear.

Using `LAMMPS`, we went beyond the article mentioned above, simulating the planar extensional flow through the `UEF` package by David Nicholson [51], obtaining data about the mean pressure tensor, energy and temperature. We organized the data by projecting the average stress $\boldsymbol{\sigma}$ on the tensorial basis adapted to the local flow $(\hat{\mathbf{I}}, \hat{\mathbf{D}}, \hat{\mathbf{G}}_3)$ illustrated in Chapter 3, but independent of the flow type and of the reference system, as we already mentioned. The coefficients of the decomposition of the stress tensor are p the pressure of the fluid, η the generalized viscosity and λ_3, related to non-Newtonian effects and normal stress differences. MD data have been fitted using principles of Gaussian Process Regression (GPR) and `pyGPs`, a devoted library in Python [49].

This microscopic results has been used, trying to extend the applicability of the Stalter's work to extensional and mixed flows. Substantially, with MD data we can associate to each node of the macroscopic computational domain the appropriate stress $\boldsymbol{\sigma}$ at each time step. Such a stress features flow-type dependent viscosity $\eta(\dot{\varepsilon}, \beta_3)$ and normal stress differences $\lambda_3(\dot{\varepsilon}, \beta_3)$.

Moreover, in a first study, we interpolated linearly the values of the parameters of the model, using the new data relative to simple shear and extension to obtain the values in intermediate situation of mixed motions $0 < |\beta_3| < 1$, important to complete the study of real fluids that are just complex. The method is usable when separation of scales (micro-macro) occurs and has been applied to the analysis of some paradigmatic examples of non-uniform planar flows, such as the flow through a 4:1 contraction and the flow past a deep hole. In doing so, we made use of `FEniCS`, a well-known Python library for numerical integration of Partial Differential Equations, that makes use of techniques of Finite Element Methods (FEM). Our results emphasize the need of considering the flow-type dependence of the material response of polymeric fluids.

Subsequently, we tried to use `LAMMPS` to get data about mixed flow, combining shear and extensional modules, already implemented on that software. This was done to avoid

the approximation introduced with linear interpolation of MD data. Unfortunately, these modules allowed us to explore only a limited range of values for the parameters of the model.

This prompted us to study various algorithms and to consider the idea proposed by Kraynik and Reinelt [38], with the aim to extend it to mixed motions cases. Substantially, it is about seeing the simulation box as a lattice that is deforming in time due to a stress applied to its walls. In 1992 they found the reproducibility conditions for square and hexagonal lattices under extensional flows. Starting from this work, we found the reproducibility equations in situations of planar mixed flows with rectangular simulation lattices, extending their algorithm and implementing these results in a software package `PMF` written in C++ language, thought to be inserted in the `LAMMPS` framework. The achievement of our boundary conditions is illustrated in Chapter 4.

Practically, choosing the sides in certain proportions, represented by the aspect ratio a, and orienting the box at a certain angle ϑ we obtained, at a critic time τ, a lattice identical to the initial one, thus through a careful remapping of the box, we can proceed with the simulation. This turns to be a clever trick to extend simulations of extensional flow to infinite times, as it already is for the shear motion, without having a box too "stretched".

The main difficulty was in identifying the decomposition of the matrix of the sides of the simulation box which allows to pass from the so-called `LAMMPS` frame to the flow frame. `LAMMPS` uses a reference in which one side of the box is always aligned with the first coordinate direction and performs all operations in that frame, except for the actual deformation which can be done in the flow frame. In our case, this frame has an eigenvector of the velocity gradient conveniently aligned with the first coordinate direction.

Hunt *et al* [31] in 2013 and Todd and Daivis [62] in 2017 had already succeeded in extending KR's work to the case of mixed motions by producing a simulation algorithm. The substantial difference of our work lies in the different parameterization used which essentially derives from the new decomposition of the velocity gradient (presented in Chapter 2). It turns out to be advantageous since at the level of the continuum we have the same parameterization and therefore the coupling becomes easier.

After implementing the code, we have been able to realize a complete set of MD simulations that cover the field of mixed flows, between simple shear and planar extension, for values $0 \leq |\beta_3| < 1$ and of the strain rate $0.0001\ \mathrm{s}^{-1} < \dot{\varepsilon} \leq 0.22\ \mathrm{s}^{-1}$.

1

Complex flows and complex fluids

The work of this thesis focuses on the concept of *complex incompressible non-Newtonian fluid* with an approach that is intended to be mathematical. A fluid is said to be non-Newtonian if the stress experienced by the fluid is not proportional to the strain rate and the relationship between the two quantities can take various forms.

The mathematical model of non-Newtonian fluid has attracted considerable scientific and technological interest. On the one hand, there is a growing and urgent scientific need to investigate, model and predict the behaviour of many natural and biological phenomena such as landslides, avalanches, blood clots, etc. On the other hand, there is an even stronger technological interest in manipulation and production of complex fluids. Among the most common non-Newtonian fluids in the food industry, that belong to our daily-life, are mayonnaise, ice-cream, mustard, cheese, chocolate and sweets. Also many personal care products can be described by non-Newtonian fluid models: shampoo, nail polish, lipstick, deodorant, toothpaste. Electronic and optical devices such as liquid crystals and solder paste belong to this category too. Molten polymers used industrially to create plastics, packaging and pharmaceutical casings, encapsulants for drug delivery, etc., are classic examples of complex materials that can be considered non-Newtonian fluids during their manufacturing process. Materials and mixtures used in building and construction science are complex fluids: cement, asphalt, bitumen. Some biological substances are (natural) non-Newtonian fluids, for example blood, mucin, synovial fluid and cannot be treated with mathematical models related to simple fluids. Among complex materials

there are also viscoelastic fluids and heterogeneous mixtures. A good introduction to the topic can be found in the book by Phan-Thien [52].

Complex fluids can display a very different behavior, spanning from solid-like to liquid-like, when subjected to different environmental conditions, due to their microstructural internal rearrangements. This is well illustrated by Larson [42] in his book. On the contrary, simple fluids are materials in which the stress resulting from the current deformation depends only on the past history of its deformation and not from external sources. The class of *Newtonian* fluids belongs to this category and represents a good approximation for some substances such as water, air and plasma in the blood in several relaxed conditions of flow (large arteries and wide tubes, for example).

Fluids of all kinds have historically been studied and observed in *viscometric flows*, i.e. flows, not necessarily uniform in space, whose velocity gradient is locally always equivalent to that of a simple shear. Coleman, Markovitz and Noll give an extensive characterisation of them in their book [8]. In recent decades, extensional flows have also been studied extensively and considered important for the rheological characterization of the fluid. Simple flows turn out to be only mathematical idealizations of the reality because they are often completely uniform and develop in regular geometries. Real processes, instead, occur in flow geometries that are rarely regular and that give rise to complex non-uniform motions, hard to investigate and classify. For this reason, we are interested to study complex fluids under generic flow conditions, considering the effect of the flow-type dependence on the macroscopic motion. We want to develop techniques able to take into account both the flow-type and the strain-rate dependence of non-Newtonian fluids properties. We are going to restrict the field of our investigation to fluids which are, to a good extent, incompressible, thus liquids.

In the characterization of fluids and the construction of macroscopic models, rheology, as the science that investigates (both computationally and experimentally) properties of materials (solids, liquids or gasses) under deformations and flows, helps us. Basically, it exploits simple flows to extract material functions, that are generally related only to such type of flow and to a particular frame of reference. However, rheometry is not sufficient for the complete characterization of non-Newtonian materials. To make available more quantitative and qualitative measurements, other sophisticated techniques such as microscopy, x-ray and neutron scattering or polarimetry are used, see Larson [42]. In recent years, computational methods are becoming increasingly common in the investigation of fluids, because they make it possible to go beyond the typical limits of laboratory experiments, to obtain data even under conditions that are difficult to reproduce in the laboratory and to do the task in a much shorter time.

1.1 Mathematical framework

In this section we are going to introduce the basic concepts of continuum mechanics that will be useful to build macroscopic flow equations.

We introduce a fixed rectangular coordinate system $Oxyz$ and a parameter $t \in \mathbb{R}^+$ describing the time. Let $\mathscr{B} \subset \mathbb{R}^3$ be the *reference configuration* of a fluid which is considered as a continuous set of particles, whose positions in the reference configuration are denoted by vectors $\boldsymbol{X} = (X, Y, Z)$ of *Lagrangian* (or *material*) coordinates. And let us assume, for sake of simplicity, that $\mathscr{B}$ is realized at time $t = 0$. We describe the movement of the particles by an injective function φ called *placement* that, at each instant t, associates the position at time t, denoted with *Eulerian* (or *spatial*) coordinates $\boldsymbol{x} = (x, y, z)$, function of the time, of the particle that at the initial time was in $\boldsymbol{X}$, as represented in Fig.1.1

$$\begin{aligned} \varphi : \mathscr{B} \times \mathbb{R}^+ &\to \mathbb{R}^3 \\ (\boldsymbol{X}, t) &\to \boldsymbol{x} := \varphi(\boldsymbol{X}, t). \end{aligned}$$

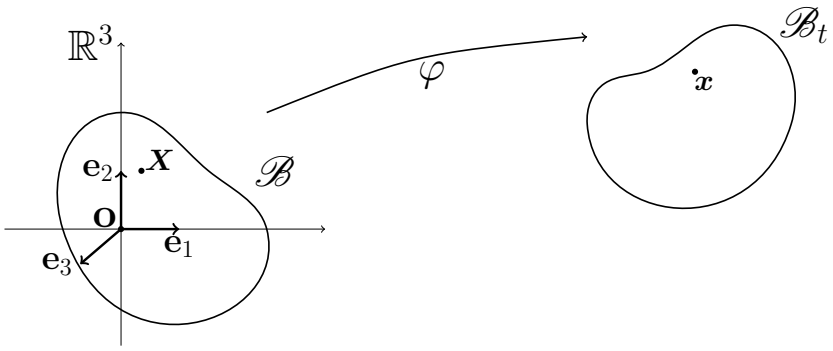

Figure 1.1: The link between the reference configuration $\mathscr{B}$ and the current configuration $\mathscr{B}_t$ is provided by the injective function placement φ.

We assume that φ, φ^{-1} are functions of class C^3 (so that acceleration field can be defined and that every position $\boldsymbol{x}$ must correspond to a unique particle $\boldsymbol{X}$) in both variables and we will call *current configuration* the set of particles $\mathscr{B}_t := \varphi(\mathscr{B}, t)$ at time t.

The *velocity* fields in material and spatial coordinates, respectively, are defined as

$$\boldsymbol{U}(\boldsymbol{X}, t) := \frac{\partial \varphi}{\partial t}(X, t), \qquad \boldsymbol{u}(\boldsymbol{x}, t) := \boldsymbol{U}(\varphi^{-1}(\boldsymbol{x}, t), t) = \frac{d\boldsymbol{x}}{dt} = \frac{\partial \varphi}{\partial t} + \boldsymbol{u} \cdot \nabla \varphi.$$

and also the *acceleration* fields become

$$\boldsymbol{A}(\boldsymbol{X},t) := \frac{\partial^2 \varphi}{\partial^2 t}(X,t), \qquad \boldsymbol{a}(\boldsymbol{x},t) := \boldsymbol{A}(\varphi^{-1}(\boldsymbol{x},t),t) = \frac{d\boldsymbol{u}}{dt} = \frac{\partial \boldsymbol{u}}{\partial t} + \boldsymbol{u}\cdot\nabla\boldsymbol{u}.$$

where $\nabla\varphi$ and $\nabla\boldsymbol{u}$ are the placement and velocity gradients and $\frac{d\boldsymbol{x}}{dt}, \frac{d\boldsymbol{u}}{dt}$ are the *material derivatives*, meaning "along particle trajectories". Lagrangian coordinates are typically employed in the theory of elasticity, while in fluid dynamics it is customary to refer to the Eulerian description (velocity and acceleration fields as functions of the current position). For this reason, from now on we will make use of Eulerian notation, even for gradient, divergence and rotor operators.

We report here a theorem of derivation under the integral sign that is useful to derive the balance equations.

Theorem 1.1.1. (Reynolds Transport Theorem)*: Let $\Omega_t \subset \mathscr{B}_t \subset \mathbb{R}^3$ be an open and limited set of particles in the current configuration with $\Omega_t := \varphi(\Omega_0, t)$, so that $\Omega_0 = \Omega(0)$. Given a scalar, vectorial or tensorial field $F(\boldsymbol{x},t)$, we have*

$$\frac{d}{dt}\int_{\Omega_t} F dV = \int_{\Omega_t}\left(\frac{\partial F}{\partial t} + \boldsymbol{u}\nabla F + F\nabla\cdot\boldsymbol{u}\right)dV \tag{1.1}$$

where the left-hand-side term is the temporal derivative of the function

$$\left\{t \mapsto \int_{\Omega_t} F(\boldsymbol{x},t)dV\right\}.$$

Further details about the proof of the theorem can be found in many different books, see for example Gurtin [26].

1.1.1 Conservation of mass and incompressibility

The mass of a continuum system Ω_t at time $t \in \mathbb{R}^+$ is obtained through the volume integral of the *mass density* per unit volume ρ at time t

$$M(\Omega_t) = \int_{\Omega_t} \rho(\boldsymbol{x},t)\, dV.$$

We are going to consider situations in which there is neither accumulation nor dispersion of mass, therefore the *Principle of conservation of mass* is valid: the mass is preserved through the motion of the fluid $\forall \Omega_t \subset \mathscr{B}_t, \quad \forall t \in \mathbb{R}^+$

$$M(\Omega_t) = M(\Omega_0).$$

By making the mass explicit and applying Theorem 1.1.1, we obtain the following condition holding $\forall \Omega_t \subset \mathscr{B}_t, \forall t \in \mathbb{R}^+$

$$\frac{d}{dt} M(\Omega_t) = \frac{d}{dt} \int_{\Omega_t} \rho(\boldsymbol{x}, t)\, dV = \int_{\Omega_t} \left(\frac{\partial \rho}{\partial t} + \nabla \cdot (\rho \boldsymbol{u}) \right) dV = 0$$

and, since Ω_t is arbitrary, the integrand is locally null, namely, $\forall t \in \mathbb{R}^+, \forall \Omega_t, \forall \boldsymbol{x} \in \Omega_t$

$$\frac{\partial \rho}{\partial t} + \nabla \cdot (\rho \boldsymbol{u}) = 0. \tag{1.2}$$

The previous equation is called *continuity equation* and expresses the *local* conservation of the mass.

At this point, we restrict ourselves to the class of *incompressible* materials because we want to investigate liquid properties, neglecting the study of gases. In these fluids, the variations in time of the density function are not relevant for the single particle, thus the density is constant along particle's trajectories, meaning $\forall \boldsymbol{X} \in \Omega_0, \forall t \in \mathbb{R}^+$

$$\rho(\varphi(\boldsymbol{X}, t), t) \equiv \text{const}$$

and, thanks to the continuity equation, we obtain a solenoidal velocity vector field

$$\frac{\partial \rho}{\partial t} + (\boldsymbol{u} \cdot \nabla)\rho = 0 \quad \Rightarrow \quad \rho(\nabla \cdot \boldsymbol{u}) = 0 \quad \Rightarrow \quad \nabla \cdot \boldsymbol{u} = 0.$$

1.1.2 Equations of motion

Dynamics implies that there is some force acting on the fluid element under consideration. The forces exerting on the body are either *surface forces* $\boldsymbol{t}$ (tractions) that acts on short ranges, and *body (volume) forces* $\boldsymbol{b}$, that act on long ranges. An example of body force is the gravitational, while the hydrodynamic pressure or the frictions between fluid elements are examples of tractions. The resultant of volume forces is expressed with the volume integral of the *density of volume forces* per unit mass $\boldsymbol{b}(\boldsymbol{x}, t)$ over the fluid element Ω_t

$$\int_{\Omega_t} \rho \boldsymbol{b}\, dV.$$

For the tractions we make the following assumption, called *Cauchy principle*: let S be an internal surface in the current configuration of the continuum body $\mathscr{B}_t$, oriented with the outward normal $\boldsymbol{n}$. There exists a distribution of forces

$$\boldsymbol{t}(\boldsymbol{x}, t; S)$$

that represents the force density per unit (current) area exerted through S by the part of the material $\mathscr{B}_t^+$ that is from the side of $\boldsymbol{n}$ towards the part of the material $\mathscr{B}_t^-$ on the side of $-\boldsymbol{n}$. The vector $\boldsymbol{t}$ acts as a sort of flux through S, see Figure 1.2. We also assume that $\boldsymbol{t}$ depends continuously on S only through the normal $\boldsymbol{n}$ with

$$\boldsymbol{t}(\boldsymbol{x}, t; S) = \boldsymbol{t}(\boldsymbol{x}, t; \boldsymbol{n}).$$

Thus, the resultant of surface forces can be expressed by the integral over the surface S

$$\int_S \boldsymbol{t}\, ds.$$

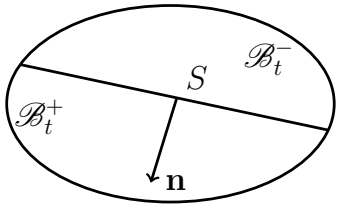

Figure 1.2: The traction $\boldsymbol{t}(\boldsymbol{x}, t; \boldsymbol{n})$ in point $\boldsymbol{x}$ is the force per unit area exerted by $\mathscr{B}_t^+$ onto $\mathscr{B}_t^-$, where S is a surface internal to the current configuration of a body.

The *principle of linear momentum balance* is also assumed: the rate of change of linear momentum of a material volume Ω_t with boundary $\partial\Omega_t$ equals the total resultant of forces acting on the body

$$\frac{d}{dt}\int_{\Omega_t} \rho\boldsymbol{u}\, dV = \int_{\Omega_t} \rho\boldsymbol{b}\, dV + \int_{\partial\Omega_t} \boldsymbol{t}\, dS \tag{1.3}$$

and, thanks to the Theorem 1.1.1, becomes

$$\int_{\Omega_t} \rho\frac{d\boldsymbol{u}}{dt}\, dV = \int_{\Omega_t} \rho\boldsymbol{b}\, dV + \int_{\partial\Omega_t} \boldsymbol{t}\, dS. \tag{1.4}$$

We are going now to state a fundamental theorem of continuum mechanics.

Theorem 1.1.2. *(Cauchy Stress Tensor): $\forall(\boldsymbol{x}, t) \in \Omega_t \times \mathbb{R}^+$, the vectorial field $\boldsymbol{t}(\boldsymbol{x}, t; \boldsymbol{n})$ is linear in $\boldsymbol{n}$, i.e. there exists a second-order tensor $\boldsymbol{\sigma}$ such that*

$$\boldsymbol{t}(\boldsymbol{x}, t; \boldsymbol{n}) = \boldsymbol{\sigma}(\boldsymbol{x}, t)\boldsymbol{n}$$

that is called Cauchy Stress Tensor.

The proof of the theorem can be found in Landau [40]. This tensor encodes the state of stress at a point inside the fluid element in the deformed (current) configuration, thus

codifies the different way this element responds to external stimuli in different directions. Thanks to the previous results and to the Divergence Theorem, the resultant of surface forces takes now the form

$$\int_{\partial\Omega_t} \boldsymbol{t}\, dS = \int_{\partial\Omega_t} \boldsymbol{\sigma}\boldsymbol{n}\, dS = \int_{\Omega_t} \nabla\cdot\boldsymbol{\sigma}\, dV$$

so that we can re-write the balance of linear momentum in terms of all volume integrals

$$\int_{\Omega_t} \rho\frac{d\boldsymbol{u}}{dt}\, dV = \int_{\Omega_t} \rho\boldsymbol{b}\, dV + \int_{\Omega_t} \nabla\cdot\boldsymbol{\sigma}\, dV.$$

For the regularity of the considered fields and, by the arbitrariness of the integration domain, we obtain this relation, holding $\forall t \in \mathbb{R}^+, \forall \boldsymbol{x} \in \Omega_t$

$$\rho\frac{d\boldsymbol{u}}{dt} = \rho\boldsymbol{b} + \nabla\cdot\boldsymbol{\sigma} \tag{1.5}$$

that is the *local equation of motion*, valid in any point of the fluid element Ω_t.

Analogously, we assume the *balance of angular momentum* to complete the previous physical hypothesis, valid $\forall\Omega_t \subset \mathscr{B}$ and $\forall t \in \mathbb{R}^+$

$$\frac{d}{dt}\int_{\Omega_t} \rho\boldsymbol{x}\times\boldsymbol{u}\, dV = \int_{\Omega_t} \rho\boldsymbol{x}\times\boldsymbol{b}\, dV + \int_{\partial\Omega_t} \boldsymbol{x}\times\boldsymbol{t}\, dS.$$

The following theorem can be proved, for details see Phan-Thien [52].

Theorem 1.1.3. *If the equation of continuity and the conservation of linear momentum hold, then the conservation of angular momentum is verified if and only if the Cauchy Stress Tensor is symmetric* $\boldsymbol{\sigma} = \boldsymbol{\sigma}^\mathsf{T}$.

In isothermal flows the equations governing the fluid-dynamics of an incompressible fluid of density $\rho(\boldsymbol{x})$ are the following

$$\nabla\cdot\boldsymbol{u} = 0 \tag{1.6}$$

$$\rho\frac{d\boldsymbol{u}}{dt} = \rho\boldsymbol{b} + \nabla\cdot\boldsymbol{\sigma} \tag{1.7}$$

$$\boldsymbol{\sigma} = \boldsymbol{\sigma}^\mathsf{T} \tag{1.8}$$

where (1.6) and (1.7) represent a system of 4 scalar equations in the 10 unknowns ρ, $\boldsymbol{u}$ and $\boldsymbol{\sigma}$. In order to have a closed problem, we need to specify further properties for the fluid. One could provide a static form for sigma and close the problem, but we prefer to keep it as a function of the other unknowns. Classically, this is done by providing a

constitutive law for the Cauchy stress tensor $\boldsymbol{\sigma}$

$$\boldsymbol{\sigma} = -p\mathbf{I} + \boldsymbol{\tau}\left(t, \rho, \nabla\rho, \dots, \boldsymbol{u}, \nabla\boldsymbol{u}, \dots\right) \tag{1.9}$$

where p is the isotropic pressure and $\boldsymbol{\tau}$ the *extra (or deviatoric) stress*, the non-isotropic part of $\boldsymbol{\sigma}$. The constitutive law is a differential operator depending on the unknowns, their derivatives and time that represents the bridge between the dynamics and the kinematics of the fluid.

In constitutive modelling we distinguish two approaches: the *continuum approach* and the *microstructure approach*. It is generally believed that relevant constitutive equations should be based on a (simplified) model of the microstructure. But, when the physics governing the microstructure interactions is complicated, one must not hesitate to introduce elements of continuum modelling, however the continuum approach should not completely replace the microstructure modelling. In Chapter 2 we will recap well-known examples of continuum constitutive models. On the contrary, the method proposed in this thesis aims to reconstruct the stress tensor at the level of the continuum without prescribing a particular functional form for it, letting rheological properties of the fluid emerging from simulations on the micro-scale.

Rheology helps us to make $\boldsymbol{\tau}$ explicit for each type of fluid considered. In the next sections we are going to illustrate the main rheological properties of fluids and the derivation of classical material functions, taking inspiration from Phan-Thien [52]. For more details we can always refer also to Larson [42].

1.2 Rheological properties

Fluids with simple microstructures are well described by the *Newtonian* constitutive equation, for which the stress tensor is proportional to the rate of the deformation. In the liquid state the mechanical properties of a Newtonian fluid are represented by only the density ρ and the shear viscosity η, which is only pressure, density and temperature-dependent while is constant in space and time. However, a constant viscosity does not qualify a fluid to be Newtonian. The term Newtonian is much more restrictive in its meaning, see Chapter 2 for some mathematical detail. The mechanical behavior of many real fluids appears to be accurately described by the theory of Newtonian fluids over a wide range of circumstances. There are natural substances such as water and air, but also biological substances, such as plasma in the blood, that can be considered in good approximation as Newtonian fluids. However, in most of the cases, the Newtonian fluid model represents an almost exclusively mathematical simplification of reality. In fact, real fluids show, generally, a *complex* behavior due to the presence of relevant microstructures

between their molecules. Polymer melts and solutions (molten plastics, fibre-reinforced or particulate plastics), suspensions of particles or droplets (blood, paint, ink, asphalt, bitumen, foodstuffs, etc.) exhibit a wide variety of *non-Newtonian effects*, that are briefly recalled here.

1.2.1 Viscosity

Shear-rate dependent viscosity

The most important property for engineering calculation is the *fluid viscosity* measured in simple shear. As shown in Fig. 1.3, the simple shear flow is generated by sliding the top wall with respect to the bottom, with the fluid in between. The quantities of interest are the *shear rate* $\dot{\gamma}$ and the *shear stress* σ_{xy}

$$\dot{\gamma} = \frac{U}{h}, \qquad \sigma_{xy} = \frac{F}{A},$$

where x is the direction of the sliding, y the direction of the velocity gradient, U the velocity of the top plate, h the sample thickness, F the tangential force on the top plate and A the fluid contact area. In the case of non-Newtonian fluids, the shear stress is an odd function of the shear rate $\sigma_{xy}(\dot{\gamma})$. The shear rate in any point can be computed also as the derivative of the horizontal component of the velocity with respect to the vertical direction $\dot{\gamma} = \partial u_x / \partial y$. The velocity gradient of this type of flow is, thus, represented by the matrix

$$\nabla \boldsymbol{u} = \begin{bmatrix} 0 & \dot{\gamma} & 0 \\ 0 & 0 & 0 \\ 0 & 0 & 0 \end{bmatrix}.$$

In addition, there may be a normal force on the plates.

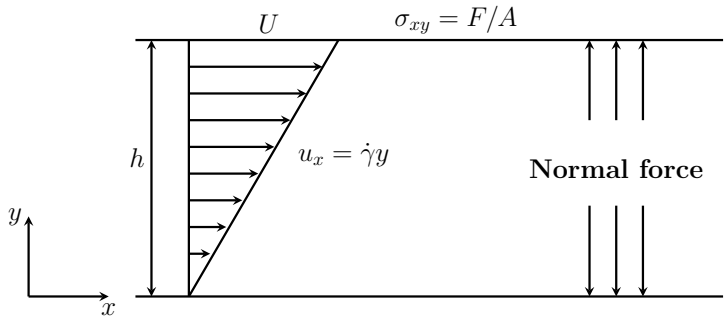

Figure 1.3: Shear flow generated by sliding one plate on top of another with velocity U. A linear velocity profile is formed $u_x = \dot{\gamma} y$, a shear stress σ_{xy} and normal pressures at the walls.

When a steady flow can be achieved, the *steady shear viscosity* is defined as the ratio of the shear stress to the shear rate

$$\eta = \frac{\sigma_{xy}}{\dot{\gamma}}. \tag{1.10}$$

and has units $\text{Pa} \cdot \text{s}$. From the rheometric measurements it appears that for most fluids with long chain microstructure (polymer melts and solutions), the viscosity exhibited under simple shear is a decreasing function of the shear rate. This type of behavior is called *shear- thinning* and is due, prevalently, to two factors: the spheroidal shape assumed by the molecules of the fluid (due to the rotational part of the flow) and the tendency of the flow, at low concentrations, to orient and structure molecules in the direction of the sliding. The opposite *shear-thickening* behavior is sometimes observed with some suspensions especially at high concentration and high shear rate deformations, due to the sudden formation of clusters which provokes the hardening of the fluid. In Chapter 5 we will discuss these facts more in relation to our results.

For some materials with solid-like behavior (for example, bread dough, biological tissues), viscosity measurement makes no sense, since the shear stress just keeps increasing with time until the sample breaks or flows out of the test cell, and what has been measured is not a material property, but an indication of the friction between the sample and the test apparatus. With suspensions of particles with surface charges, one can get viscosity to behave in many different ways; even a discontinuity at a particular shear rate may be induced.

1.2.2 Normal Stress Differences

As reported in Phan-Thien [52], normal stress differences are the differences between the unequal normal stresses that are generated in a non-Newtonian fluid under a shear flow. For a Newtonian fluid, instead, the normal stresses are always equal, so, normal differences are null. We define the *first* and the *second normal stress difference* as

$$\mathrm{N}_1 = \sigma_{xx} - \sigma_{yy} \qquad \mathrm{N}_2 = \sigma_{yy} - \sigma_{zz} \tag{1.11}$$

where, as usual, x is the direction of the sliding, y the direction of the velocity gradient and z the vorticity direction of the flow. $\mathrm{N}_1, \mathrm{N}_2$ are even functions of the shear rate and we can, alternatively, use the *first and second normal stress coefficients* as the ratios

$$\Psi_1 = \frac{\mathrm{N}_1}{\dot{\gamma}^2}, \qquad \Psi_2 = \frac{\mathrm{N}_2}{\dot{\gamma}^2} \tag{1.12}$$

that are also even functions of the shear rate, but give us additional information on the (quadratic, quartic, ...) trend of the functions N_1 and N_2.

Instead of N_2, the real parameter usually measured in laboratory is N_0, a combination of N_1 and N_2

$$N_0 = \frac{N_1}{2} + N_2 = \frac{\sigma_{xx} + \sigma_{yy}}{2} - \sigma_{zz}.$$

In the shear flow the response of a non-Newtonian fluid is characterized by three degrees of freedom of the symmetric stress tensor $\boldsymbol{\sigma}$, represented by the normal stress differences N_1 and N_2 (or their coefficients) and the steady shear viscosity η. All of them are classically called *viscometric material functions*.

In the work of Seto & Giusteri [55], they investigated the presence and the microscopic origin of normal stress differences in dense suspensions under simple shear flows in the high-Péclet-number limit (advection phenomena prevail over conduction ones). As they said, in viscoelastic fluids, a non-vanishing N_1 is a signature of elastic effects. And the convection determined by the rotational component of the flow leads to positive values of N_1. While in suspensions, since suspended particles are usually very rigid, there is no elastic component. Most of the experimental results reported a negative N_1 for moderately dense suspensions at high shear rates. Few of them also reported a transition from negative to positive values of N_1 at high shear rates in very dense suspensions. A misconception is widespread that the sign of N_1 discriminates between regimes in which either hydrodynamic interactions are dominant (negative N_1) or contact interactions are (positive N_1). However, Seto & Giusteri proved that positive values of N_1 are only associated to artefacts of the numerical approximation needed in a computational model that aims at simulating hard-sphere suspensions. Moreover N_1 is used as a measure of the misalignment between the eigenvectors of the stress $\boldsymbol{\sigma}$ and the ones of $\mathbf{D}$. The quantity N_0, instead, measures a stress anisotropy caused by the planarity of simple shear flows. The flow generates more pressure in the flow plane than in the vorticity direction (stress contribution is globally anisotropic). Differently from the standard N_2, the quantity N_0 is fully independent of N_1, thus N_0 is more informative than N_2.

Weissenberg Rod-Climbing Effect

When a rod is rotating in a viscoelastic fluid, the fluid moves up the rod rather than depressing the free surface near the rod. This phenomenon is called the *Weissenberg rod-climbing effect*. Rod climbing is due to the fluid element being able to support a tension along a streamline (first normal stress difference) that forces the fluid up the rod.

Die Swell

When a viscoelastic fluid exits from a capillary of diameter D, it tends to swell considerably more than a Newtonian fluid. For highly viscous Newtonian fluids, the swell ratio, $\frac{D_E}{D}$, where D_E is the extrudate diameter, is at most 13%. For a polymer melt, the extrudate diameter could be a few times the capillary diameter. This phenomenon is called *die swell*, and the dominant mechanism causing this is the first normal stress difference. In fact, Tanner [57] proposed the simple rule for capillary die swell, based on a simple analysis

$$\frac{D_E}{D} = 0.13 + \left[1 + \frac{1}{2}\left(\frac{\mathrm{N}_1}{2\sigma_{xy}}\right)_w^2\right]^{1/6}, \tag{1.13}$$

where N_1 and σ_{xy} are the first normal stress difference and the shear stress, both evaluated at the wall (subscript w). Die swell is mainly due to the fluid elasticity, but it can also occur with the shear-thinning induced by viscous heating. Inertia tends to reduce the amount of swell, and to delay it.

Flow down an inclined channel

The second normal stress difference N_2, although small in magnitude, is important in some cases. In the flow down an inclined channel, a Newtonian fluid is seen to have a nearly flat free surface, whereas a convex surface is seen for a viscoelastic fluid with a negative N_2. Viscoelasticity is also responsible for the reversal of the secondary flow pattern.

1.2.3 Extensional Flows

Extensional viscosity

Stretching or elongating a sample fluid specimen leads to diagonal velocity gradient, coinciding with its symmetrized part

$$\nabla \boldsymbol{u} = \begin{bmatrix} a & 0 & 0 \\ 0 & b & 0 \\ 0 & 0 & c \end{bmatrix}$$

where, in the incompressible case $\mathrm{tr}\,(\nabla \boldsymbol{u}) = a + b + c = 0$. There are three different types of extensional flow: when $b = -a$ and $c = 0$ one has a *planar elongational flow*, we have a *uni-axial elongational flow* when $a = b = -c/2$ and a *bi-axial elongation* when $a \neq b$ and $c = -(a + b)$. Usually, a equals the dominant eigenvalue $a = \dot{\varepsilon}$ which is called

elongational (or strain) rate and it physically corresponds to the rate of the deformation in a point.

The gradient is here expressed in a different frame of reference with respect to the simple shear case: the x-axis corresponds, in fact, to the direction of the extension (or of the dominant eigenvector). For the simple shearing motion, the most convenient frame to use is the one that has the contraction and expansion directions oriented at 45° with respect to the reference axes.

The viscosity in the extensional motion is defined differently from that in simple shear and is called *elongational viscosity*

$$\eta_E = \frac{\sigma_{xx} - \sigma_{yy}}{\dot{\varepsilon}}.$$

being the ratio between the first normal stress N_1 and the strain rate $\dot{\varepsilon}$.

Except at very low elongational rates, elongational viscosity does not usually reach a steady state (the sample elongates and fails). The elongational viscosity of a Newtonian fluid is a few times its shear viscosity, but for a polymer solution, the elongational viscosity can be orders of magnitude greater. Classically, the *Trouton ratio* (Tr) is defined as the ratio of the elongation viscosity to the shear viscosity of the fluid

$$\mathrm{Tr} = \frac{\eta_E}{\eta}. \tag{1.14}$$

For a Newtonian fluid, the Trouton ratio is $\mathrm{Tr} = 3$ in dimension three and $\mathrm{Tr} = 4$ in the planar case.

1.2.4 Mixed Flows

Mixed flows combine characteristics of shearing and extensional flows. We represent here the most general velocity gradient (in two dimensions for convenience) through the following matrix

$$\nabla \boldsymbol{u} = \frac{1}{2} G \begin{bmatrix} 1+\alpha & 1-\alpha \\ -(1-\alpha) & -(1+\alpha) \end{bmatrix}$$

where α is a "flow-type" parameter , $\alpha = 0$ for simple shear and $\alpha = 1$ for planar extension; G corresponds to the shear rate $\dot{\gamma}$ if $\alpha = 0$ while to the extension rate $\dot{\varepsilon}$ if the flow is a planar extension. A general 2D flow (thus, every type of flow) can be generated in an apparatus called *four-roll mill*, see Larson [42] for details.

For mixed flows, rheometric standards for material functions are not yet defined, so a new theoretical framework is needed to characterize non-Newtonian fluids in every type of flow. We will see in the next chapter how this framework is mathematically formalized

and how new and more generic material functions defined.

2

Kinematics and constitutive laws

The concept of constitutive law is key in fluid dynamics: it expresses in rigorous mathematical terms the link between the fluid's kinematic state and its corresponding dynamic state, dissecting how it responds to external stimuli through the generation of internal stresses. In deformable bodies, therefore also in fluids, the relevant kinematics is represented in a first approximation by the velocity gradient tensor $\nabla \boldsymbol{u}$, that encodes the relative velocity around a point. It is usually expressed by separating the symmetric part $\mathbf{D}$, related to the deformation, from the skew part $\mathbf{W}$, related to the rotational components of the flow. We choose to represent $\nabla \boldsymbol{u}$ on the basis of the eigenvectors of $\mathbf{D}$ because this representation is independent of the reference system.

Our study is restricted to the case of planar flows and, in doing so, two kinematic parameters $\dot{\varepsilon}$ and β_3 emerge. The first is the rate of strain, while the second is the component of vorticity in the direction orthogonal to the flow and will be our flow-type parameter. On the basis of β_3 we make a classification of flows associating to each of its values a type of motion: extensional, simple shear, rigid rotational or mixed. The details of this classification are illustrated in Giusteri & Seto [25], which we take as reference for this chapter. There are many other classification theories, that have been overviewed by Thompson & Mendes [60], such as those by Astarita [1] and Schunk & Scriven [54].

Mathematically, the dynamic response of the fluid is expressed with the Cauchy stress tensor $\boldsymbol{\sigma}$ which quantifies the internal stresses that are generated on a fluid element as a consequence of external actions. Rheology aims at codifying this fluid response

through mathematical laws, linking the stress to the kinematic parameters. These laws should be simple, understandable and easy to use, but are often not very general and not applicable to different contexts if they are designed for specific flows. We will review the main classical constitutive laws such as Ideal, Newtonian, Power-law, Reiner–Rivlin and Second order fluids.

However, in the development of this work we will follow a data-driven approach without postulating constitutive laws. To this end, we take as reference the decomposition introduced by Giusteri & Seto [25]. This decomposition is adaptable to any flow and fluid and requires only that $\mathbf{D}$ is non-zero. It has a local nature in both space and time and does not depend on the geometry of the flow. Precursors to that decomposition and to the methods that we will employ can be found in the works by Miller *et al.* [47] and by Hartkamp *et al.* [27].

2.1 Velocity gradient and flow classification

The *velocity gradient* tensor $\nabla \boldsymbol{u}$ is the most fundamental kinematic variable of the fluid dynamics. In fact, in the theory of deformable bodies, the relevant kinematic quantity is not the velocity itself $\boldsymbol{u}(\boldsymbol{x}, t)$ in a geometrical point $\boldsymbol{x}$, but the relative velocity between nearby points, expressed through the velocity gradient. If $\nabla \boldsymbol{u} = \mathbf{0}$, there is no difference in nearby point velocities and the body is moving with a rigid translation of constant velocity. If we change inertial observer, the system is not moving at all, no internal forces are arising and we don't have any fluid dynamics. So we, obviously, assume $\nabla \boldsymbol{u} \neq \mathbf{0}$ in our discussion.

Some ideal flows display homogeneous gradients, maybe varying over time. Anyway real fluxes are characterized by non-uniform velocity gradients, that can change drastically from one point to another, and for this reason, we are interested in their *local kinematics*, analyzing the velocity gradient computed at a point.

The symmetric part $\mathbf{D}$ of the velocity gradient $\nabla \boldsymbol{u}$ is called *strain rate tensor*, and its skew-symmetric part $\mathbf{W}$ is called *vorticity tensor*. We have

$$\nabla \boldsymbol{u} = \mathbf{D} + \mathbf{W}$$

with $\mathbf{D} = \frac{1}{2}\left(\nabla \boldsymbol{u} + \nabla \boldsymbol{u}^{\mathsf{T}}\right)$ and $\mathbf{W} = \frac{1}{2}\left(\nabla \boldsymbol{u} - \nabla \boldsymbol{u}^{\mathsf{T}}\right)$. In this way, we can distinguish the contribution of the stretching part (due to the flowing of the material) from the contribution of the rotational part to the velocity gradient.

The multiscale method we have implemented is centered around the decomposition of the stress tensor illustrated in the work of Giusteri & Seto [25]. Their starting point is $\mathbf{D}$ and the representation of tensors $\mathbf{D}, \mathbf{W}$ onto the basis of eigenvectors of $\mathbf{D}$. They

consider cases in which $\mathbf{D}$ has a non-vanishing dominant eigenvalue, corresponding to the strain rate $\dot{\varepsilon}$, related to the eigenvector $\hat{\boldsymbol{d}}_1$, while $\hat{\boldsymbol{d}}_2$ and $\hat{\boldsymbol{d}}_3$ are the other two orthonormal eigenvectors. Moreover, for incompressible fluids the trace of the velocity gradient is null, $\mathrm{tr}\,(\nabla \boldsymbol{u}) = \mathrm{tr}\,(\mathbf{D}) = 0$, and it can be proved that the most generic symmetric part of $\nabla \boldsymbol{u}$ is represented as

$$\mathbf{D} = \frac{2\dot{\varepsilon}}{\sqrt{3+4\alpha^2}}\left[\hat{\boldsymbol{d}}_1 \otimes \hat{\boldsymbol{d}}_1 - (1/2+\alpha)\hat{\boldsymbol{d}}_2 \otimes \hat{\boldsymbol{d}}_2 - (1/2-\alpha)\hat{\boldsymbol{d}}_3 \otimes \hat{\boldsymbol{d}}_3\right]$$

with $0 \leq \alpha \leq 1/2$ an asymmetry parameter. Then, the most generic skew-symmetric part of $\nabla \boldsymbol{u}$ is represented by this combination

$$\mathbf{W} = \dot{\varepsilon}\left[\beta_1(\hat{\boldsymbol{d}}_3 \otimes \hat{\boldsymbol{d}}_2 - \hat{\boldsymbol{d}}_2 \otimes \hat{\boldsymbol{d}}_3) + \beta_2(\hat{\boldsymbol{d}}_1 \otimes \hat{\boldsymbol{d}}_3 - \hat{\boldsymbol{d}}_3 \otimes \hat{\boldsymbol{d}}_1) + \beta_3(\hat{\boldsymbol{d}}_2 \otimes \hat{\boldsymbol{d}}_1 - \hat{\boldsymbol{d}}_1 \otimes \hat{\boldsymbol{d}}_2)\right]$$

with β_k, $k = 1, 2, 3$, (dimensionless) components of the (normalized) vorticity vector along the directions $\hat{\boldsymbol{d}}_k$

$$\beta_k = \frac{1}{2\dot{\varepsilon}}\hat{\boldsymbol{d}}_k \cdot \nabla \times \boldsymbol{u}. \tag{2.1}$$

The *strain rate* $\dot{\varepsilon}$ quantifies the intensity of the deformation. For us, it corresponds to the tensorial Frobenius[1] norm of the matrix $\mathbf{D}$

$$\mathrm{II}_{\mathbf{D}} = \frac{1}{2}\left((\mathrm{tr}\,\mathbf{D})^2 + \mathrm{tr}\,(\mathbf{D}^2)\right) = \frac{\mathrm{tr}\,\mathbf{D}^2}{2} \qquad \Rightarrow \quad |\dot{\varepsilon}| = ||\mathbf{D}|| = \sqrt{\frac{\mathbf{D}:\mathbf{D}}{2}} = \sqrt{\mathrm{II}_{\mathbf{D}}} = \sqrt{\frac{\mathrm{tr}\,\mathbf{D}^2}{2}}.$$

The inverse of $\dot{\varepsilon}$ is the local timescale of the deformation t_D, for any value of the dimensionless parameters α and β_k.

In this three dimensional representation the nine degrees of freedom of $\nabla \boldsymbol{u}$ reduce to eight because of the incompressibility condition, and are represented by $\dot{\varepsilon}$, β_k, α, $\hat{\boldsymbol{d}}_i$, that are our independent descriptors of the local state of the system. Since each of these parameters depends on time and space $(\boldsymbol{x}, t)$, at any given time, it is possible to associate to each point $\boldsymbol{x}$ of the (continuum) flow domain a unique value for them.

In our discussion we focus on the two-dimensional case, but in the future we may extend the discussion and results to the three-dimensional case. Thus, in planar motions $\alpha = 1/2$ (maximal asymmetry) and $\beta_1 = \beta_2 = 0$ because the vorticity has components only in the out-of-flow-plane direction, thus, the representation of the velocity gradient becomes

$$\mathbf{D} = \dot{\varepsilon}\left[\hat{\boldsymbol{d}}_1 \otimes \hat{\boldsymbol{d}}_1 - \hat{\boldsymbol{d}}_2 \otimes \hat{\boldsymbol{d}}_2\right], \qquad \mathbf{W} = \dot{\varepsilon}\beta_3\left[\hat{\boldsymbol{d}}_2 \otimes \hat{\boldsymbol{d}}_1 - \hat{\boldsymbol{d}}_1 \otimes \hat{\boldsymbol{d}}_2\right].$$

In this framework it is clear that, up to rotations of $\hat{\boldsymbol{d}}_i$, $\dot{\varepsilon}$ and β_3 are unique representatives

[1] The Frobenius inner product of two matrices $\mathbf{A}$ and $\mathbf{B}$ is defined as $\mathbf{A} : \mathbf{B} := \mathrm{tr}\,(\mathbf{A}^{\mathsf{T}} \cdot \mathbf{B})$.

of the local kinematics. $\dot{\varepsilon}$ works as weight for the deformation and β_3 works as weight of the amount of rotation relative to the deformation.

In particular, the parameter β_3 is going to be, for us, the *flow-type parameter* because is useful to classify all the *steady homogeneous flows*. According to Giusteri and Seto [25], doing a proper classification means to group flow conditions that are, at the microscopic level, physically equivalent entailing equivalent material responses at the macroscopic level. For a fixed $\dot{\varepsilon}$, our parametrization with β_3 measures the tendency of the fluid to protect from strong deformations increasing its vorticity. Precisely, $\beta_3 = 0$ corresponds to *planar extension*, because it is not reacting at all through vorticity, $|\beta_3| = 1$ corresponds to *simple shear* flows (equivalent components of rotation and deformation), $|\beta_3| \gg 1$ *highly rotational flows*, when the body clearly prefers to rotate rather than deform, and *mixed flows* for $0 < |\beta_3| < 1$ in which there are different intakes from the two types of motion. In Fig. 2.1 we report the illustration of the vectorial velocity fields of homogeneous flows, spanning from extension to rotation, on the basis the classification just illustrated.

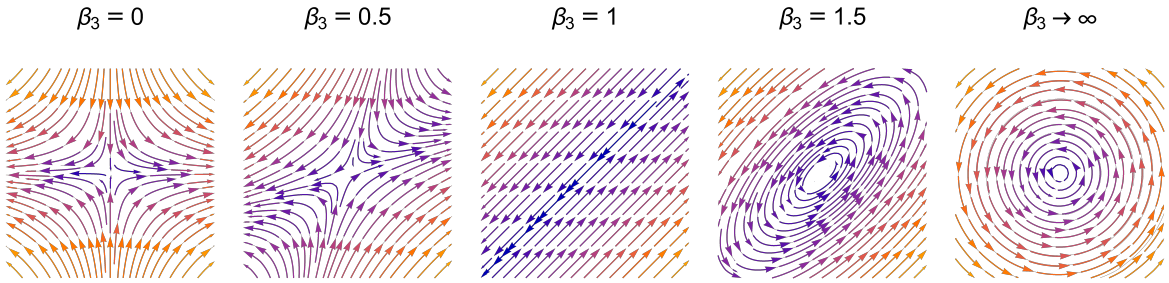

Figure 2.1: Streamlines of the velocity gradient fields of five types of flow, classified on the basis of the parameter β_3, which is the vorticity component in the out-of-flow direction. From the left side we have: planar extension $|\beta_3| = 0$, intermediate (extensional) motion ($0 < |\beta_3| < 1$), simple shear $|\beta_3| = 1$, intermediate (rotational) motion ($1 < |\beta_3| < \infty$) and purely rotation.

Flow characterization has a long history, overviewed by Thompson & Mendes [60]. Astarita [1] also gave his important contribution to this theory, proposing criteria and the following scalar parameter as flow-type parameter

$$R = -\frac{\mathrm{tr}\,(\mathbf{W}^2)}{\mathrm{tr}\,(\mathbf{D}^2)}.$$

The scheme offered by Schunk and Scriven [54] includes among the kinematic parameters the material derivative of the eigenvectors $\hat{\boldsymbol{d}}_k$ of $\mathbf{D}$ through the so called Jaumann derivative, for example.

Among all the choices, the simplest we can make is considering only the dependence of the stress tensor onto the velocity gradient: all constitutive prescriptions will be, in

such a case, combinations of the two parameters $\dot{\varepsilon}$ and β_3, up to rotations of the $\hat{\boldsymbol{d}}_i$. No one forbids us to go beyond the mere dependence on the velocity gradient. In more complicated fluids there are dependencies also from higher order derivatives of $\boldsymbol{u}$, for example see Schunk & Scriven [54], the history of the deformation, or the amount of volume fraction of the dilute phase into the solvent and many other factors. Doing this, would require the introduction of further kinematic parameters.

2.2 Classical constitutive laws

The constitutive law, also called *rheological equation of state*, makes the linkage between the stress response and the kinematic local state of the material, providing the missing information to have a closed mathematical problem for the fluid. Finding this model for each fluid is the central concern of rheology. In this section we give a brief overview of the main well-known constitutive laws for incompressible fluids.

2.2.1 Ideal Fluid

The first and simplest choice we can make in modeling a fluid is to neglect the tangential stress, responsible of viscosity. This leads to the model of *Ideal (or Ideal) Fluids*. In this case every direction is eigenvector for $\boldsymbol{\sigma}$ and therefore the stress tensor is an isotropic tensor, multiple of the Identity tensor $\mathbf{I}$

$$\boldsymbol{\sigma} = -p\mathbf{I}$$

where $p > 0$ is the pressure coefficient, that is assumed to be a function of $(\boldsymbol{x}, t)$.

In the static regime all the fluids can be, approximately, considered ideal, while in the dynamic regime, this choice corresponds to neglect the viscosity of the fluid and consider only the category of inviscid fluids, which is not consistent with reality, but is only a mathematical idealization. For biological and industrial fluids, it is fundamental to find constitutive equations for $\boldsymbol{\sigma}$ which take into account the viscosity.

2.2.2 Reiner-Rivlin fluids

Among the class of viscous fluids there is a special class of incompressible fluids whose extra-stress tensor depends only on the strain-rate tensor $\boldsymbol{\tau} = \boldsymbol{\tau}(\mathbf{D})$. These fluids are called *Reiner-Rivlin* fluids and are represented by equation

$$\boldsymbol{\sigma} = -p\mathbf{I} + f_1(\mathrm{II}_{\mathbf{D}}, \mathrm{III}_{\mathbf{D}})\mathbf{D} + f_2(\mathrm{II}_{\mathbf{D}}, \mathrm{III}_{\mathbf{D}})\left[\mathbf{D}^2 - (\mathrm{II}_{\mathbf{D}}/3)\mathbf{I}\right]$$

with f_1, f_2 arbitrary scalar functions of the invariants of matrix $\mathbf{D}$ with $\mathrm{II}_{\mathbf{D}} = \mathrm{tr}\,(\mathbf{D}^2)$ and $\mathrm{III}_{\mathbf{D}} = \det \mathbf{D}$. $\mathbf{D}$ is encoding information about deformation and how the fluid is flowing, thus, the dependence of $\boldsymbol{\sigma}$ onto $\mathbf{D}$ is the simplest one we can make.

Newtonian Fluid

If we consider Reiner-Rivlin fluids with $f_2 = 0$ and $f_1 = 2\eta$ constant in space and time, we obtain the model of *Newtonian fluids*, the most famous and investigated class of viscous fluids. For them, the relation between the stress $\boldsymbol{\sigma}$ and $\mathbf{D}$ is linear and represented by the following equation

$$\boldsymbol{\sigma} = -p\mathbf{I} + 2\eta\mathbf{D}$$

where η is the *shear viscosity*, codifying the amount of mechanical energy that is dissipating through the motion of the fluid. The second principle of the thermodynamics leads to a restriction on its sign $\eta \geq 0$.

The substitution of this expression in the Cauchy stress tensor of the equation of motion leads to the popular *Navier-Stokes problem* of the fluid dynamics.

Generalized Newtonian Fluid

The two characteristic features of the Newtonian model are the linear dependence of the stress tensor $\boldsymbol{\sigma}$ on $\mathbf{D}$, and the fact that the shear viscosity η is constant.

A natural way of generalizing the constitutive equation is to drop the linearity assumption, as well as to allow the dependency of η on the tensor $\mathbf{D}$. Thus, another particular case of Reiner-Rivlin fluids are the, so-called, *Generalized Newtonian fluids*, for which

$$f_2 = 0 \qquad \text{and} \qquad f_1 = \eta(\mathrm{II}_{\mathbf{D}}) \tag{2.2}$$

so, the stress tensor $\boldsymbol{\sigma}$ becomes

$$\boldsymbol{\sigma} = -p\mathbf{I} + \eta(\mathrm{II}_{\mathbf{D}})\mathbf{D}, \qquad \eta \geq 0. \tag{2.3}$$

There are several choices we can make for the function η. A very popular one is the so-called "*Power-law*" model, introduced by W. Ostwald as early as 1925, where η is a power function of the strain rate $\dot{\varepsilon}$

$$\eta(\mathrm{II}_{\mathbf{D}}) = k|\dot{\varepsilon}|^{s-2}$$

with k a dimensional coefficient, $s > 1$ a non-dimensional constant which is called *flow behavior index*. Changing s means to consider different models of Power-Law fluids:

- if $1 < s < 2$ we have *shear thinning (or pseudo-plastic) fluids*, i.e., the viscosity decreases as $\dot{\varepsilon}$ increases
- if $s > 2$ we have *shear thickening (or dilatant) fluids*, i.e., the viscosity increases as $\dot{\varepsilon}$ increases
- if $s = 2$ we have *Newtonian fluids.*

2.2.3 Second order fluids

Suppose that the particle $\boldsymbol{X}$, that is in position $\boldsymbol{\xi}$ at time τ, occupies the position $\boldsymbol{x}$ at time t. The *deformation gradients* between old and new positions are expressed as

$$\mathbf{F}(t) = \left(\frac{\partial \boldsymbol{x}}{\partial \boldsymbol{X}}\right)^{\mathsf{T}}, \qquad \mathbf{F}(\tau) = \left(\frac{\partial \boldsymbol{\xi}}{\partial \boldsymbol{X}}\right)^{\mathsf{T}}$$

and the *relative deformation gradient* as

$$\mathbf{F}_t(\tau) = \left(\frac{\partial \boldsymbol{\xi}}{\partial \boldsymbol{x}}\right)^{\mathsf{T}} = \left(\frac{\partial \boldsymbol{\xi}}{\partial \boldsymbol{X}}\right)^{\mathsf{T}} \cdot \left(\frac{\partial \boldsymbol{X}}{\partial \boldsymbol{x}}\right)^{\mathsf{T}} = \mathbf{F}(\tau)\mathbf{F}(t)^{-1} = \mathbf{I} + (\tau - t)\nabla \boldsymbol{u} + \mathcal{O}\left((\tau - t)^2\right).$$

We can now define the (Right) Cauchy-Green tensor through the relative deformation gradient

$$\mathbf{C}_t(\tau) = \mathbf{F}_t(\tau)^{\mathsf{T}}\mathbf{F}_t(\tau). \tag{2.4}$$

We are going now to see an example of a class of fluids out of the category of Reiner-Rivlin fluids: the *Second Order fluids*, whose stress tensor is built from the velocity field with up to two derivatives. We can express now the, so called, n-th *Rivlin-Eriksen* tensor through material derivatives of $\mathbf{C}_t(\tau)$

$$\mathbf{A}_n(t) = \frac{d^n}{d\tau^n}\mathbf{C}_t(\tau)|_{\tau=t}, \qquad n = 0, 1, 2, \ldots \tag{2.5}$$

and, since $\mathbf{F}_t(\tau) = \mathbf{I}$ and $\mathbf{C}_t(\tau)|_{\tau=t} = \mathbf{I}$, we obtain the first Rivlin-Eriksen tensor

$$\mathbf{A}_0 = \mathbf{I}.$$

The higher order tensors can be obtained through the following recursive formula

$$\mathbf{A}_{n+1} = \frac{d}{dt}\mathbf{A}_n + \mathbf{A}_n\nabla \boldsymbol{u} + (\nabla \boldsymbol{u})^{\mathsf{T}}\mathbf{A}_n \qquad n = 1, 2, \ldots$$

that we can prove being equivalent to (2.5) (see Phan-Thien [52]). For example, we have

$$\mathbf{A}_1 = \mathbf{0} + \mathbf{I}\nabla \boldsymbol{u} + (\nabla \boldsymbol{u})^{\mathsf{T}}\mathbf{I} = 2\mathbf{D}, \qquad \mathbf{A}_2 = 2(\dot{\mathbf{D}} + \mathbf{D}\nabla \boldsymbol{u} + (\nabla \boldsymbol{u})^{\mathsf{T}}\mathbf{D}).$$

At this point, as reported in Phan-Thien [52], the stress tensor of a *second-order fluid* is an isotropic function of the Rivlin-Eriksen tensors $\mathbf{A}_n$ until the second order represented by

$$\boldsymbol{\sigma} = -p\mathbf{I} + \eta\mathbf{A}_1 + \alpha_1\mathbf{A}_1^2 + \alpha_2\mathbf{A}_2$$

where η is the zero-shear viscosity and α_1, α_2 are the constant material moduli usually referred to as normal stress moduli, with $\alpha_1 \geq 0$ and $\alpha_1 + \alpha_2 = 0$. It represents another attempt to go beyond the linear Newtonian model, considering, moreover, some *memory effects*, related to the history of the material, as we take into account $\dot{\mathbf{D}}$, the time derivative of the strain tensor. This can be useful when we want to consider the fact that the current behavior of the fluid can depend not only on its current state, but also on past events.

2.3 New decomposition of the stress

The stress decomposition proposed in the work of Giusteri and Seto [25] is adapted to the local flow because the coefficients are not given *a priori*, but are functions of the kinematic state of the fluid. These coefficients generalize the classical concept of viscosity and normal stress differences, born within the simple shear framework, for flows other than simple shear.

Let us start building an orthogonal basis in the space of three dimensional symmetric tensors, starting from the identity tensor $\mathbf{I}$ and $\mathbf{D}$. $\mathbf{D}$ is traceless, thus orthogonal to $\mathbf{I}$ and we take $\mathbf{E}$ orthogonal to both $\mathbf{D}$ and $\mathbf{I}$ and diagonal on the basis of the eigenvectors $(\hat{\boldsymbol{d}}_1, \hat{\boldsymbol{d}}_2, \hat{\boldsymbol{d}}_3)$ of $\mathbf{D}$. Its expression on the basis of $\hat{\boldsymbol{d}}_i$ is uniquely determined by

$$\mathbf{E} = \frac{\dot{\varepsilon}}{\sqrt{3+4\alpha^2}}\left(-2\alpha\hat{\boldsymbol{d}}_1\hat{\boldsymbol{d}}_1 - (3/2-\alpha)\,\hat{\boldsymbol{d}}_2\hat{\boldsymbol{d}}_2 + (3/2+\alpha)\,\hat{\boldsymbol{d}}_3\hat{\boldsymbol{d}}_3\right).$$

To complete the orthogonal basis of symmetric tensors, we must consider the following off-diagonal tensors

$$\mathbf{G}_i = \dot{\varepsilon}\left(\hat{\boldsymbol{d}}_j\hat{\boldsymbol{d}}_k + \hat{\boldsymbol{d}}_k\hat{\boldsymbol{d}}_j\right), \quad i,j,k = \{1,2,3\}, \quad i \neq j \neq k.$$

Finally, considering the dimensionless formulation we get

$$\hat{\mathbf{D}} = \dot{\varepsilon}^{-1}\mathbf{D}, \quad \hat{\mathbf{E}} = \dot{\varepsilon}^{-1}\mathbf{E}, \quad \hat{\mathbf{G}}_i = \dot{\varepsilon}^{-1}\mathbf{G}_i$$

and we obtain a basis adapted to the local flow, in the sense that their expression is

linked to the local kinematic state of the fluid through the $\hat{\boldsymbol{d}}_i$

$$\mathscr{B} = (\hat{\mathbf{I}}, \hat{\mathbf{D}}, \hat{\mathbf{E}}, \hat{\mathbf{G}}_1, \hat{\mathbf{G}}_2, \hat{\mathbf{G}}_3). \tag{2.6}$$

This basis depends on time and space on the kinematic parameters, but the form of these tensors with respect to $\hat{\boldsymbol{d}}_k$ remains the same for each type of local flow. The Cauchy-Stress tensor $\boldsymbol{\sigma}$ is now decomposed onto such a basis, in the following way

$$\boldsymbol{\sigma} = -p\mathbf{I} + 2\dot{\varepsilon}\left(\eta\hat{\mathbf{D}} + \lambda_0\hat{\mathbf{E}} + \lambda_1\hat{\mathbf{G}}_1 + \lambda_2\hat{\mathbf{G}}_2 + \lambda_3\hat{\mathbf{G}}_3\right) \tag{2.7}$$

with p, η, λ_0, λ_1, λ_2, λ_3 called *response coefficients* being functions of the *local kinematic state* of the system $\dot{\varepsilon}$, β_k and $\hat{\boldsymbol{d}}_i$. They represent the new material functions of the non-Newtonian fluid. Sometimes, in the data analysis, the following representation will be more suitable

$$\boldsymbol{\sigma} = \mathrm{C_I}\hat{\mathbf{I}} + \mathrm{C_D}\hat{\mathbf{D}} + \mathrm{C_E}\hat{\mathbf{E}} + \mathrm{C_{G_1}}\hat{\mathbf{G}}_1 + \mathrm{C_{G_2}}\hat{\mathbf{G}}_2 + \mathrm{C_{G_3}}\hat{\mathbf{G}}_3$$

where the following correspondence between parameters holds

$$\mathrm{C_I} := -p, \quad \mathrm{C_D} := 2\dot{\varepsilon}\eta, \quad \mathrm{C_E} := 2\dot{\varepsilon}\lambda_0, \qquad \mathrm{C_{G_1}} := 2\dot{\varepsilon}\lambda_1, \quad \mathrm{C_{G_2}} := 2\dot{\varepsilon}\lambda_2, \quad \mathrm{C_{G_3}} := 2\dot{\varepsilon}\lambda_3.$$

The coefficients are just defined as orthogonal projections of $\boldsymbol{\sigma}$ onto the relative tensors

$$p := -\frac{\boldsymbol{\sigma} : \hat{\mathbf{I}}}{||\hat{\mathbf{I}}||^2} = -\frac{1}{3}\mathrm{tr}\,(\boldsymbol{\sigma}), \quad \eta := \frac{1}{2\dot{\varepsilon}}\frac{\boldsymbol{\sigma} : \hat{\mathbf{D}}}{||\hat{\mathbf{D}}||^2}, \quad \lambda_0 := \frac{1}{2\dot{\varepsilon}}\frac{\boldsymbol{\sigma} : \hat{\mathbf{E}}}{||\hat{\mathbf{E}}||^2}, \quad \lambda_k := \frac{1}{2\dot{\varepsilon}}\frac{\boldsymbol{\sigma} : \hat{\mathbf{G}}_k}{||\hat{\mathbf{G}}_k||^2} \tag{2.8}$$

where the orthogonality between these tensors is defined using the Frobenius inner product. This definition does not fix a particular form for the coefficients and is valid for every type of motion because there is no reference to any specific flow characteristic. Therefore also their physical meaning is no more strictly related to the local flow or the type of non-Newtonian fluid and remains the same in every reference system or geometry:

- p is the *isotropic pressure* of the fluid, combining two contributions: the proper hydrodynamic pressure p_h and the Lagrange multiplier p_l due to the incompressibility constraint, $p = p_h + p_l$
- η is the *generalized viscosity*: the rate of conversion of mechanical energy in internal energy. "Generalized" because we include irreversible dissipation and reversible elastic energy in this contribution
- λ_0 is the *anisotropy*: indicates that the intensity of the stress is not distributed along its principal directions proportionally to the distribution of the rate of deformation even if the eigenvectors of $\boldsymbol{\sigma}$ are still aligned with those of $\mathbf{D}$
- λ_i with $i = 1, 2, 3$ are the *reorientation factors*: their presence reveal that the

eigenvectors of $\boldsymbol{\sigma}$ are no more aligned with those of $\mathbf{D}$ due to the presence of elastic effects or rearrangements of the micro-structure.

So how do we characterize the form of these functions? Through MD simulations of homogeneous flows. We choose a non-Newtonian fluid, we simulate its homogeneous flows (simple shear, extensional, rigid or intermediate motions with fixed flow parameter and fixed strain rate). For each type of flow, we project the stress $\boldsymbol{\sigma}$ onto the basis tensors, making a sample of the coefficient's values and building a functional form from that. At the macroscopic level, the decomposition of $\boldsymbol{\sigma}$ just illustrated is used to re-compose $\boldsymbol{\sigma}$ from the coefficient functions and basis tensors at each point of the simulated domain.

Let us focus, for a moment, on the *planar* case. In this case, a reorientation of eigenvectors of $\boldsymbol{\sigma}$ can happen only in the flow plane, thus $\lambda_1 = \lambda_2 = 0$ and the stress decomposition reduces to

$$\boldsymbol{\sigma}(\dot{\varepsilon}, \beta_3) = -p(\dot{\varepsilon}, \beta_3)\mathbf{I} + 2\dot{\varepsilon}\left[\eta(\dot{\varepsilon}, \beta_3)\hat{\mathbf{D}} + \lambda_0(\dot{\varepsilon}, \beta_3)\hat{\mathbf{E}} + \lambda_3(\dot{\varepsilon}, \beta_3)\hat{\mathbf{G}}_3\right]. \tag{2.9}$$

The term $2\dot{\varepsilon}\lambda_0\hat{\mathbf{E}}$ induces an isotropic shift in the eigenvalues of $\boldsymbol{\sigma}$ of a factor $-\dot{\varepsilon}\lambda_0$ in each of the directions of the flow plane and of $2\dot{\varepsilon}\lambda_0$ in the out-of-flow plane. The anisotropy induced is measured through the *ellipsoidal factor* $2\dot{\varepsilon}\lambda_0/p$. The term $2\dot{\varepsilon}\lambda_3$ induces, instead, a reorientation of the eigenvectors of $\boldsymbol{\sigma}$ with respect to those of $\hat{\mathbf{D}}$ by an angle φ (called *reorientation angle*) whose tangent function is

$$\tan\varphi = \frac{\lambda_3}{\eta + \sqrt{\eta^2 + \lambda_3^2}} = \frac{\mathrm{C}_{G_3}}{\mathrm{C}_D + \sqrt{\mathrm{C}_D^2 + \mathrm{C}_{G_3}^2}} \qquad \underset{(\lambda_3 \ll \eta)}{\approx} \qquad \frac{\lambda_3}{2\eta} = \frac{\mathrm{C}_{G_3}}{2\mathrm{C}_D}. \tag{2.10}$$

2.3.1 New material functions

Now we can see how the proposal of this new framework completes and unifies the standard material functions and extend their meaning to the case of mixed motions.

In *simple shear* flows the shear rate is twice the strain rate, $\dot{\gamma} = 2\dot{\varepsilon}$, thus the velocity gradient and the basis tensors of the stress decomposition take the form

$$\nabla\boldsymbol{u} = \dot{\varepsilon}\begin{bmatrix}0 & 2 & 0\\ 0 & 0 & 0\\ 0 & 0 & 0\end{bmatrix}, \quad \mathbf{D} = \dot{\varepsilon}\begin{bmatrix}0 & 1 & 0\\ 1 & 0 & 0\\ 0 & 0 & 0\end{bmatrix}, \quad \mathbf{E} = \dot{\varepsilon}\begin{bmatrix}-\frac{1}{2} & 0 & 0\\ 0 & -\frac{1}{2} & 0\\ 0 & 0 & 1\end{bmatrix}$$

$$\mathbf{G}_1 = \dot{\varepsilon}\begin{bmatrix}0 & 0 & 1\\ 0 & 0 & -1\\ 1 & -1 & 0\end{bmatrix}, \quad \mathbf{G}_2 = \dot{\varepsilon}\begin{bmatrix}0 & 0 & 1\\ 0 & 0 & 1\\ 1 & 1 & 0\end{bmatrix}, \quad \mathbf{G}_3 = \dot{\varepsilon}\begin{bmatrix}-1 & 0 & 0\\ 0 & 1 & 0\\ 0 & 0 & 0\end{bmatrix}.$$

This brings the stress tensor to the following expression

$$\boldsymbol{\sigma} = \begin{bmatrix} -p - \dot{\varepsilon}\lambda_0 - 2\dot{\varepsilon}\lambda_3 & 2\dot{\varepsilon}\eta & 2\dot{\varepsilon}\lambda_1 + 2\dot{\varepsilon}\lambda_2 \\ 2\dot{\varepsilon}\eta & -p - \dot{\varepsilon}\lambda_0 + 2\dot{\varepsilon}\lambda_3 & -2\dot{\varepsilon}\lambda_1 + 2\dot{\varepsilon}\lambda_2 \\ 2\dot{\varepsilon}\lambda_1 + 2\dot{\varepsilon}\lambda_2 & -2\dot{\varepsilon}\lambda_1 + 2\dot{\varepsilon}\lambda_2 & -p + 2\dot{\varepsilon}\lambda_0 \end{bmatrix}.$$

From this representation and the definition of the normal stress differences ((1.2.2) and (1.11)) we can trivially retrieve the expression of $\mathrm{N}_1, \mathrm{N}_2, \mathrm{N}_0$ and of the steady shear viscosity η in terms of the new material functions

$$\mathrm{N}_1 = -4\dot{\varepsilon}\lambda_3 = -2\mathrm{C}_{\mathrm{G}3}, \qquad \mathrm{N}_2 = 2\dot{\varepsilon}\lambda_3 - \dot{\varepsilon}\lambda_0 = \mathrm{C}_{\mathrm{G}3} - \frac{3}{2}\mathrm{C}_{\mathrm{E}}, \qquad \mathrm{N}_0 = -\dot{\varepsilon}\lambda_0 = -\frac{3}{2}\mathrm{C}_{\mathrm{E}}$$

$$\eta = \frac{\sigma_{xy}}{2\dot{\varepsilon}} = \frac{\mathrm{C}_{\mathrm{D}}}{2\dot{\varepsilon}}$$

and we can observe that $\mathrm{C}_{\mathrm{G}_3}$ has the same meaning of the standard first normal stress difference N_1, while C_{E} is representative of N_0 and C_{D} is related to the shear stress. As they are defined for any type of flow and take on a meaning independent of the flow, it seems that they can generalize the concept of viscosity and express a measure of non-Newtonian effects in generic flows and geometries.

In the *planar extensional* flow the basis tensors of the decomposition take the form

$$\nabla\boldsymbol{u} = \mathbf{D} = \dot{\varepsilon}\begin{bmatrix} 1 & 0 & 0 \\ 0 & -1 & 0 \\ 0 & 0 & 0 \end{bmatrix}, \quad \mathbf{E} = \dot{\varepsilon}\begin{bmatrix} -\frac{1}{2} & 0 & 0 \\ 0 & -\frac{1}{2} & 0 \\ 0 & 0 & 1 \end{bmatrix}$$

$$\mathbf{G}_1 = \dot{\varepsilon}\begin{bmatrix} 0 & 0 & 0 \\ 0 & 0 & 1 \\ 0 & 1 & 0 \end{bmatrix}, \quad \mathbf{G}_2 = \dot{\varepsilon}\begin{bmatrix} 0 & 0 & 1 \\ 0 & 0 & 0 \\ 1 & 0 & 0 \end{bmatrix}, \quad \mathbf{G}_3 = \dot{\varepsilon}\begin{bmatrix} 0 & 1 & 0 \\ 1 & 0 & 0 \\ 0 & 0 & 0 \end{bmatrix}$$

thus, the stress tensor has the following expression

$$\boldsymbol{\sigma} = \begin{bmatrix} -p + 2\eta\dot{\varepsilon} - \dot{\varepsilon}\lambda_0 & 2\dot{\varepsilon}\lambda_3 & 2\dot{\varepsilon}\lambda_2 \\ 2\dot{\varepsilon}\lambda_3 & -p - 2\eta\dot{\varepsilon} - \dot{\varepsilon}\lambda_0 & 2\dot{\varepsilon}\lambda_1 \\ 2\dot{\varepsilon}\lambda_2 & 2\dot{\varepsilon}\lambda_1 & -p + 2\dot{\varepsilon}\lambda_0 \end{bmatrix}$$

and we retrieve the expression of the elongational viscosity from

$$\eta_E = \frac{\sigma_{xx} - \sigma_{yy}}{\dot{\varepsilon}} = \frac{2\mathrm{C}_{\mathrm{D}}}{\dot{\varepsilon}}$$

so the fact that the coefficient C_{D} is related to the viscosity is confirmed. And we take

as further material functions the coefficients $\mathrm{C_E}, \mathrm{C}_{G_3}$ with the same meaning that $\mathrm{N}_0, \mathrm{N}_1$ have in simple shear motion. We can retrieve these coefficients through their definition as projections, or in this way

$$\mathrm{C_E} = -\frac{2}{3}\left(\frac{\sigma_{xx}-\sigma_{yy}}{2} - \sigma_{zz}\right), \qquad \mathrm{C}_{G_3} = 2\dot{\varepsilon}\lambda_3 = \sigma_{xy}.$$

To sum up, the correspondences between standard and new material functions are as follows

$$\begin{aligned}
\beta_3 = 1 \qquad & \eta(\dot{\gamma} = 2\dot{\varepsilon}) = \eta(\dot{\varepsilon}, \beta_3 = 1) \\
& \mathrm{N}_1(\dot{\gamma} = 2\dot{\varepsilon}) = -4\dot{\varepsilon}\lambda_3(\dot{\varepsilon}, \beta_3 = 1) \\
& \mathrm{N}_2(\dot{\gamma} = 2\dot{\varepsilon}) = 2\dot{\varepsilon}\lambda_3(\dot{\varepsilon}, \beta_3 = 1) - 3\dot{\varepsilon}\lambda_0(\dot{\varepsilon}, \beta_3 = 1) \\
& \mathrm{N}_0(\dot{\gamma} = 2\dot{\varepsilon}) = -3\dot{\varepsilon}\lambda_0(\dot{\varepsilon}, \beta_3 = 1) \\
\beta_3 = 0 \qquad & \eta_E(\dot{\varepsilon}) = 4\eta(\dot{\varepsilon}, \beta_3 = 0)
\end{aligned}$$

but the new framework manages to extract functions that extend the meaning of N_1 and N_0 also to the extensional (and mixed) case.

Considering *planar mixed motions*, the representation of the velocity gradient in this new context (with respect to the basis $\mathcal{B}$ of the eigenvectors $\boldsymbol{d}_1, \boldsymbol{d}_2$ of the strain rate tensor $\mathbf{D}$) is done by

$$(\nabla \boldsymbol{u})_{\mathcal{B}} = \dot{\varepsilon}\begin{bmatrix} 1 & \beta_3 & 0 \\ -\beta_3 & -1 & 0 \\ 0 & 0 & 0 \end{bmatrix}.$$

However we are going to consider the representation of $\nabla \boldsymbol{u}$ with respect to the vectorial basis $\mathcal{B}'$ made of one eigenvector of the gradient and its orthogonal complement, because it will be more useful for our discussion. For more details about this change of basis see Chapter 4. Thus, we obtain the velocity gradient and its symmetric part

$$(\nabla \boldsymbol{u})_{\mathcal{B}'} = \begin{bmatrix} \dot{\varepsilon}\sqrt{1-\beta^2} & 2\dot{\varepsilon}\beta & 0 \\ 0 & -\dot{\varepsilon}\sqrt{1-\beta^2} & 0 \\ 0 & 0 & 0 \end{bmatrix}, \qquad \mathbf{D}_{\mathcal{B}'} = \begin{bmatrix} \dot{\varepsilon}\sqrt{1-\beta^2} & \dot{\varepsilon}\beta & 0 \\ \dot{\varepsilon}\beta & -\dot{\varepsilon}\sqrt{1-\beta^2} & 0 \\ 0 & 0 & 0 \end{bmatrix}$$

where $\beta = -\beta_3$. The eigenvalues of $\mathbf{D}'_{\mathcal{B}}$ are $\lambda_{1,2} = \pm\dot{\varepsilon}$, $\lambda_3 = 0$ with relative unit-norm

eigenvectors $\hat{\boldsymbol{d}}_3 = [0, 0, 1]$ and

$$\mathbf{d}_1 = \left[-\frac{\left(1+\sqrt{1-\beta^2}\right)}{\beta} \quad 1 \quad 0 \right], \qquad \hat{\mathbf{d}}_1 = \sqrt{2\left(1+\sqrt{1-\beta^2}\right)} \left[-\frac{1}{2} \quad \frac{1-\sqrt{1-\beta^2}}{2\beta} \quad 0 \right]$$

$$\mathbf{d}_2 = \left[\frac{\left(1-\sqrt{1-\beta^2}\right)}{\beta} \quad 1 \quad 0 \right], \qquad \hat{\mathbf{d}}_2 = \sqrt{2\left(1-\sqrt{1-\beta^2}\right)} \left[\frac{1}{2} \quad \frac{1+\sqrt{1-\beta^2}}{2\beta} \quad 0 \right].$$

We change sign to $\hat{\mathbf{d}}_1$, to have a right-handed basis, getting the tensor products

$$\begin{aligned}
\hat{\mathbf{d}}_1 \otimes \hat{\mathbf{d}}_1 &= 2\left(1+\sqrt{1-\beta^2}\right) \left[\frac{1}{2} \quad \frac{\sqrt{1-\beta^2}-1}{2\beta} \quad 0 \right] \otimes \left[\frac{1}{2} \quad \frac{\sqrt{1-\beta^2}-1}{2\beta} \quad 0 \right] \\
&= 2\left(1+\sqrt{1-\beta^2}\right) \begin{bmatrix} \frac{1}{4} & \frac{\sqrt{1-\beta^2}-1}{4\beta} & 0 \\ \frac{\sqrt{1-\beta^2}-1}{4\beta} & \frac{\left(\sqrt{1-\beta^2}-1\right)^2}{4\beta^2} & 0 \\ 0 & 0 & 0 \end{bmatrix} = \begin{bmatrix} \frac{1+\sqrt{1-\beta^2}}{2} & -\frac{\beta}{2} & 0 \\ -\frac{\beta}{2} & \frac{1-\sqrt{1-\beta^2}}{2} & 0 \\ 0 & 0 & 0 \end{bmatrix}
\end{aligned}$$

$$\begin{aligned}
\hat{\mathbf{d}}_2 \otimes \hat{\mathbf{d}}_2 &= 2\left(1-\sqrt{1-\beta^2}\right) \left[\frac{1}{2} \quad \frac{1+\sqrt{1-\beta^2}}{2\beta} \quad 0 \right] \otimes \left[\frac{1}{2} \quad \frac{1+\sqrt{1-\beta^2}}{2\beta} \quad 0 \right] \\
&= 2\left(1-\sqrt{1-\beta^2}\right) \begin{bmatrix} \frac{1}{4} & \frac{1+\sqrt{1-\beta^2}}{4\beta} & 0 \\ \frac{1+\sqrt{1-\beta^2}}{4\beta} & \frac{\left(1+\sqrt{1-\beta^2}\right)^2}{4\beta^2} & 0 \\ 0 & 0 & 0 \end{bmatrix} = \begin{bmatrix} \frac{1-\sqrt{1-\beta^2}}{2} & \frac{\beta}{2} & 0 \\ \frac{\beta}{2} & \frac{1+\sqrt{1-\beta^2}}{2} & 0 \\ 0 & 0 & 0 \end{bmatrix}
\end{aligned}$$

$$\begin{aligned}
\hat{\mathbf{d}}_1 \otimes \hat{\mathbf{d}}_2 &= \sqrt{2\left(1-\sqrt{1-\beta^2}\right) \cdot 2\left(1+\sqrt{1-\beta^2}\right)} \left[\frac{1}{2} \quad \frac{\sqrt{1-\beta^2}-1}{2\beta} \quad 0 \right] \otimes \left[\frac{1}{2} \quad \frac{1+\sqrt{1-\beta^2}}{2\beta} \quad 0 \right] \\
&= 2\beta \begin{bmatrix} \frac{1}{4} & \frac{1+\sqrt{1+\beta^2}}{4\beta} & 0 \\ \frac{\sqrt{1-\beta^2}-1}{4\beta} & -\frac{1}{4} & 0 \\ 0 & 0 & 0 \end{bmatrix} = \begin{bmatrix} \frac{\beta}{2} & \frac{1+\sqrt{1-\beta^2}}{2} & 0 \\ \frac{\sqrt{1-\beta^2}-1}{2} & -\frac{\beta}{2} & 0 \\ 0 & 0 & 0 \end{bmatrix}
\end{aligned}$$

$$\begin{aligned}
\hat{\mathbf{d}}_2 \otimes \hat{\mathbf{d}}_1 &= \sqrt{2\left(1-\sqrt{1-\beta^2}\right) \cdot 2\left(1+\sqrt{1-\beta^2}\right)} \left[\frac{1}{2} \quad \frac{1+\sqrt{1-\beta^2}}{2\beta} \quad 0 \right] \otimes \left[\frac{1}{2} \quad \frac{\sqrt{1-\beta^2}-1}{2\beta} \quad 0 \right] \\
&= 2\beta \begin{bmatrix} \frac{1}{4} & \frac{\sqrt{1-\beta^2}-1}{4\beta} & 0 \\ \frac{1+\sqrt{1-\beta^2}}{4\beta} & -\frac{1}{4} & 0 \\ 0 & 0 & 0 \end{bmatrix} = \begin{bmatrix} \frac{\beta}{2} & \frac{\sqrt{1-\beta^2}-1}{2} & 0 \\ \frac{1+\sqrt{1-\beta^2}}{2} & -\frac{\beta}{2} & 0 \\ 0 & 0 & 0 \end{bmatrix}
\end{aligned}$$

$$\hat{\mathbf{d}}_2 \otimes \hat{\mathbf{d}}_3 = \sqrt{2\left(1-\sqrt{1-\beta^2}\right)}\begin{bmatrix}\frac{1}{2} & \frac{1+\sqrt{1-\beta^2}}{2\beta} & 0\end{bmatrix} \otimes \begin{bmatrix}0 & 0 & 1\end{bmatrix}$$
$$= \sqrt{2\left(1-\sqrt{1-\beta^2}\right)}\begin{bmatrix}0 & 0 & \frac{1}{2}\\ 0 & 0 & \frac{1+\sqrt{1-\beta^2}}{2\beta}\\ 0 & 0 & 0\end{bmatrix}$$

$$\hat{\mathbf{d}}_3 \otimes \hat{\mathbf{d}}_2 = \sqrt{2\left(1-\sqrt{1-\beta^2}\right)}\begin{bmatrix}0 & 0 & 1\end{bmatrix} \otimes \begin{bmatrix}\frac{1}{2} & \frac{1+\sqrt{1-\beta^2}}{2\beta} & 0\end{bmatrix}$$
$$= \sqrt{2\left(1-\sqrt{1-\beta^2}\right)}\begin{bmatrix}0 & 0 & 0\\ 0 & 0 & 0\\ \frac{1}{2} & \frac{1+\sqrt{1-\beta^2}}{2\beta} & 0\end{bmatrix}$$

$$\hat{\mathbf{d}}_1 \otimes \hat{\mathbf{d}}_3 = \sqrt{2\left(1+\sqrt{1-\beta^2}\right)}\begin{bmatrix}\frac{1}{2} & \frac{\sqrt{1-\beta^2}-1}{2\beta} & 0\end{bmatrix} \otimes \begin{bmatrix}0 & 0 & 1\end{bmatrix}$$
$$= \sqrt{2\left(1+\sqrt{1-\beta^2}\right)}\begin{bmatrix}0 & 0 & \frac{1}{2}\\ 0 & 0 & \frac{\sqrt{1-\beta^2}-1}{2\beta}\\ 0 & 0 & 0\end{bmatrix}$$

$$\hat{\mathbf{d}}_3 \otimes \hat{\mathbf{d}}_1 = \sqrt{2\left(1+\sqrt{1-\beta^2}\right)}\begin{bmatrix}0 & 0 & 1\end{bmatrix} \otimes \begin{bmatrix}\frac{1}{2} & \frac{\sqrt{1-\beta^2}-1}{2\beta} & 0\end{bmatrix}$$
$$= \sqrt{2\left(1+\sqrt{1-\beta^2}\right)}\begin{bmatrix}0 & 0 & 0\\ 0 & 0 & 0\\ \frac{1}{2} & \frac{\sqrt{1-\beta^2}-1}{2\beta} & 0\end{bmatrix}$$

and the tensor basis are functions of the kinematic parameters $\dot{\varepsilon}$ and β and assumes the following form

$$\mathbf{E} = \dot{\varepsilon}\begin{bmatrix}-\frac{1}{2} & 0 & 0\\ 0 & -\frac{1}{2} & 0\\ 0 & 0 & 1\end{bmatrix}, \qquad \mathbf{G}_1 = \dot{\varepsilon}\sqrt{2\left(1-\sqrt{1-\beta^2}\right)}\begin{bmatrix}0 & 0 & \frac{1}{2}\\ 0 & 0 & \frac{1+\sqrt{1-\beta^2}}{2\beta 3}\\ \frac{1}{2} & \frac{1+\sqrt{1-\beta^2}}{2\beta 3} & 0\end{bmatrix}$$

$$\mathbf{G}_2 = \dot{\varepsilon}\sqrt{2\left(1+\sqrt{1-\beta^2}\right)}\begin{bmatrix}0 & 0 & \frac{1}{2}\\ 0 & 0 & \frac{\sqrt{1-\beta^2}-1}{2\beta}\\ \frac{1}{2} & \frac{\sqrt{1-\beta^2}-1}{2\beta} & 0\end{bmatrix}, \quad \mathbf{G}_3 = \begin{bmatrix}\dot{\varepsilon}\beta & \dot{\varepsilon}\sqrt{1-\beta^2} & 0\\ \dot{\varepsilon}\sqrt{1-\beta^2} & -\dot{\varepsilon}\beta & 0\\ 0 & 0 & 0\end{bmatrix}.$$

We check that this mixed formulation is consistent with the basis tensors found for simple shear and extensional motion.

For $\beta \to -1$ we retrieve exactly the same identical tensors found previously in the shear case

$$\mathbf{D} = \dot{\varepsilon} \begin{bmatrix} 0 & 1 & 0 \\ 1 & 0 & 0 \\ 0 & 0 & 0 \end{bmatrix}, \qquad \mathbf{E} = \dot{\varepsilon} \begin{bmatrix} -\frac{1}{2} & 0 & 0 \\ 0 & -\frac{1}{2} & 0 \\ 0 & 0 & 1 \end{bmatrix}$$

$$\mathbf{G}_1 = \dot{\varepsilon}\sqrt{2} \begin{bmatrix} 0 & 0 & \frac{1}{2} \\ 0 & 0 & -\frac{1}{2} \\ \frac{1}{2} & -\frac{1}{2} & 0 \end{bmatrix}, \qquad \mathbf{G}_2 = \dot{\varepsilon}\sqrt{2} \begin{bmatrix} 0 & 0 & \frac{1}{2} \\ 0 & 0 & \frac{1}{2} \\ \frac{1}{2} & \frac{1}{2} & 0 \end{bmatrix}, \qquad \mathbf{G}_3 = \dot{\varepsilon} \begin{bmatrix} -1 & 0 & 0 \\ 0 & 1 & 0 \\ 0 & 0 & 0 \end{bmatrix}$$

and also in the limit of $\beta \to 0$ we have $\lim_{\beta\to 0} \dot{\varepsilon}\sqrt{2\left(1-\sqrt{1-\beta^2}\right)}\left(\frac{1+\sqrt{1-\beta^2}}{2\beta}\right) = 1$, getting the tensors

$$\mathbf{D} = \dot{\varepsilon} \begin{bmatrix} 1 & 0 & 0 \\ 0 & -1 & 0 \\ 0 & 0 & 0 \end{bmatrix}, \qquad \mathbf{E} = \dot{\varepsilon} \begin{bmatrix} -\frac{1}{2} & 0 & 0 \\ 0 & -\frac{1}{2} & 0 \\ 0 & 0 & 1 \end{bmatrix}$$

$$\mathbf{G}_1 = \dot{\varepsilon} \begin{bmatrix} 0 & 0 & 0 \\ 0 & 0 & 1 \\ 0 & 1 & 0 \end{bmatrix}, \qquad \mathbf{G}_2 = \dot{\varepsilon} \begin{bmatrix} 0 & 0 & 1 \\ 0 & 0 & 0 \\ 1 & 0 & 0 \end{bmatrix}, \qquad \mathbf{G}_3 = \dot{\varepsilon} \begin{bmatrix} 0 & 1 & 0 \\ 1 & 0 & 0 \\ 0 & 0 & 0 \end{bmatrix}$$

previously recovered for the planar extensional flow. Therefore the formulation in the mixed case is consistent and the new mathematical framework is suitable for describing in a unified way all the types of flux intermediate between simple shear and planar extensional motion.

2.4 Advantages of new material functions

Each of the coefficients of the decomposition (2.7) represents a *material function* for the fluid and their characterization through MD simulation techniques is extremely powerful. Computational experiments, in fact, realize flow conditions that would not be accessible in the laboratory or that would not be easily or cheaply feasible.

This material functions $p(\dot{\varepsilon}, \beta_k), \eta(\dot{\varepsilon}, \beta_k), \lambda_k(\dot{\varepsilon}, \beta_k)$ are advantageous for these reasons:

- they are defined in the same way, as projections, in every flow condition
- they are the same in every frame of reference, because this framework is linked to eigenvectors of $\mathbf{D}$
- they can be used with every flow classification scheme, simply by changing independent descriptors, so it is extremely versatile. Independent descriptors should be

measurable quantities that avoid redundancy, in the sense that two distinct sets of values should label distinct kinematical states of the system.

The first property is very important for dealing with data that we have in great abundance in non-viscometric flows. The classical material functions are, in fact, defined in relation to a particular type of flow and in relation to a precise frame of reference. While our functions are simply defined as projections of the Cauchy Stress Tensor onto some tensors that are normalized with $\dot{\varepsilon}$ and are therefore flow/frame-independent.

The last property denotes their general applicability and the fact that they include the standard material functions, but extending them to a broader and more general set of flow conditions.

3

Non-Equilibrium Molecular Dynamics

In this Chapter we want to introduce basic concepts of Molecular Dynamics (MD) and the main ideas that we followed in doing MD simulations.

MD represent a well-established computational technique to simulate the microscopic interactions among the molecules of a material. In this context, Non-Equilibrium means that the simulated system is not in a state of thermodynamical equilibrium. And in our specific case, this is due to the fact that the motion of the particles is induced by a deformation applied to the simulation box that leads to the overheating of the system. A thermostatting routine is, thus, needed to reset the system to the desired value of average temperature.

In our particular case, at each timestep, an integration of SLLOD equations of motion for each particle is performed to update positions and velocities. This is done in conjunction with a thermostat (Nosé-Hoover in our case) which makes it possible to carry out the simulation under conditions of constant volume V, temperature T and total number of particles N. This creates a system trajectory consistent with the canonical ensemble, as explained in Sec. 3.3.1.

SLLOD equations of motion, originally proposed by Hoover and Ladd [39], were proven to be equivalent to Newton's equations of motion for shear flow by Evans & Morriss [19]. They were later shown to generate the desired velocity gradient and the correct production of work for all homogeneous flow by Daivis and Todd [10]. As implemented in LAMMPS, they are coupled to a Nosé-Hoover chain thermostat (typical for

box that are changing in shape) in a Velocity Verlet formulation.

MD simulations realize the so called *bulk flow* of a fluid element that is composed of infinitely many particles. This is done imposing Periodic Boundary conditions, i.e., surrounding the main cell with many other identical cells, following the same dynamics of the primitive one. This avoid boundary effects and let us to deal with hundreds, instead of millions, of particles. These choices give the correct dynamics because beyond a certain number of particles, the statistical effect observed in the main cell is the same as that which would be observed with (ideally) infinite molecules. PBCs make it possible to take down the computational costs that would be involved in calculating the trajectories of many thousands of different particles. It will therefore be sufficient to calculate the dynamics of the molecules in the main cell.

Finally, there are two requirements that the simulation box must meet in order to be able to support simulations with arbitrarily long timescales: compatibility and reproducibility, which we will explain in detail later. There are several open source available softwares to perform MD simulations, such as `GROMACS`, `AMBER`, `NAMD`, ... However we choose to make use of `LAMMPS` (Large-scale Atomic/Molecular Massively Parallel Simulator), a versatile and well-developed parallel particle simulator at the atomic, meso, or continuum scale of many materials such as metals, biomolecules, polymers, coarse-grained materials and so on.

`LAMMPS` makes it possible to carry out simulations of simple shear and extensional motion, which can be extended indefinitely thanks to algorithms for re-initialising the simulation box. Deformation causes particles to be extremely close to each other and sometimes to interact with periodic copies of themselves. It is therefore necessary that the system meets the requirements of compatibility and reproducibility so that reinitialization can take place and the simulation can continue undisturbed.

The contents illustrated in these chapters come from classic manuals such as Hoover [28, 29], Evans & Morris [34] and Leimkhuler [45].

3.1 Basics of MD

According to [24], Molecular Dynamics simulation is a technique for computing the equilibrium and transport properties of a classical many-body system. In this context, the word *classical* means that constituent nuclei of particles obey the laws of classical mechanics and this represents an excellent approximation for a wide range of materials. Only when we consider the translational or rotational motion of light atoms or molecules (He, H_2, D_2) or vibrational motion with a frequency ν such that $\hbar\nu > k_B T$ ($\hbar$ is the Planck constant, k_B the Boltzmann constant, T the target temperature) we should worry

about quantum effects.

It is possible to express the equations of motion in some domain of a system of nuclei, by use of Newton's Second Law

$$m\boldsymbol{a} = \mathbf{F}.$$

Therefore MD are carried out through Newton's equations integration, where the forces are empirical forces determined from a potential energy function φ. Denoting with $\boldsymbol{r}_i \in \mathbb{R}^3$ the position vector of atom i and the atomic mass by m_i, three ODE (one for each component) must be solved for each particle of a $N-$atom system

$$m_i \frac{d^2\boldsymbol{r}_i}{dt^2} = -\nabla\varphi \qquad \forall i = 1, \ldots, \mathrm{N}.$$

MD simulation techniques are becoming increasingly developed in recent years. Software simulations are considered proper virtual experiments, since they follow the same procedures as real experiments and have the same objectives.

When we perform a real experiment we follow, broadly speaking, these steps: we prepare the sample for the analysis, we connect it to a measuring instrument (manometer, viscosimeter, rheometer, thermometer, ...), we measure observables during a time interval and we average over that interval to extract meaningful statistical information. Then, to increase accuracy of the solution we try to eliminate statistical noise averaging on a longer time, or using signal noise techniques.

In Molecular Dynamics the same approach is used:

1. *selection of a model* for the interactions among N particles (is equivalent to the preparation of the sample)
2. *reading of the parameters* of the run, such as initial temperature, number of particles, density, timestep, number of iterations, ...
3. *initialization* of the system, through the selection of positions and velocities
4. *computation of the forces* on all the particles (equivalent to measuring initial quantities in real experiments)
5. *integration of Newton's equations* of motion (corresponding to making the experiment)
6. *performing measurements* and printing the averages of measured quantities.

Points 4), 5) and 6) are repeated at each timestep until equilibration is reached (at least), i.e until the properties of the system no longer change with time, and then, carried out for the desired length of time.

Numerical simulations are often used to support and complement real experiments and vice versa. The two methodologies have different strengths: simulations, for example,

provide access to all microscopic information and directly reveal molecular mechanisms and local properties, while experiments have access to much larger and more complicated systems as well as longer time scales.

3.1.1 Interaction potentials

When designing a classical potential energy function in the empirical approach, the modeller simply works within a defined framework using parameters and prescribed functional forms to match the properties of the system to experimental data.

In the most common situations, the potential energy function consists of a sum of 2-body, 3-body and/or 4-body terms

$$\varphi_{ij}(\boldsymbol{r}_i, \boldsymbol{r}_j), \qquad \varphi_{ijk}(\boldsymbol{r}_i, \boldsymbol{r}_j, \boldsymbol{r}_k), \qquad \varphi_{ijkl}(\boldsymbol{r}_i, \boldsymbol{r}_j, \boldsymbol{r}_k, \boldsymbol{r}_l).$$

The 2-body terms describe repulsion due to the impenetrability of the outer valence shell of atoms (*Pauli repulsion*), bonds between atoms which "share" electrons, and the Coulombic attractive and repulsive forces due to net charges accumulating on the atoms of bound groups. In this work, we are going to make use only of φ_{ij}, denoting it simply with φ. This is because in the case of the viscoelastic model we use (presented in the previous Chapter 2) the binary interactions are those that give the dominant contribution to the dynamics.

The *Lennard-Jones* (LJ) potential is the best known and most used of the empirical potentials to describe (non-Coulombic and non-bonded) interatomic and intermolecular interaction, both attraction and repulsion. At very small interatomic or intermolecular distances, the electron densities overlap, generating very intense repulsive forces, characterized by a very short range of action and by the fact that they grow rapidly as molecules approach. For them there is no theoretically derived equation that describes them, so we have to rely on some potential empirical functions. The LJ function also includes the attractive part due to the van der Waals interaction and is solely a function of the separation distance $r_{ij} = ||\boldsymbol{r}_i - \boldsymbol{r}_j||$ between two particles i and j whose position vectors are $\boldsymbol{r}_i$ and $\boldsymbol{r}_j$. It is independent of the relative orientation of their separation vector

$$\varphi_{\mathrm{LJ}}(r_{ij}) = \begin{cases} 4\epsilon\left[\left(\dfrac{\sigma}{r_{ij}}\right)^{12} - \left(\dfrac{\sigma}{r_{ij}}\right)^{6}\right] & r_{ij} \leq r_{\mathrm{cut}} \\ 0 & \text{otherwise} \end{cases} \tag{3.1}$$

where $-\epsilon$ is a minimum energy realized when the beads centers are at distance $r_{ij} = \sqrt[6]{2}\sigma$, σ is the length scale and the diameter of the beads. r_{cut} is the distance of null potential

that can be chosen arbitrarily, to include certain neighbouring particles in the force calculation. For proper scaling, during simulations, all calculations are performed in reduced units where $\epsilon/k_B = \sigma = m = 1$. This means we are measuring all distances in units of σ, all temperatures in units of ϵ/k_B and all masses in units of m.

The *Weeks–Chandler–Andersen* (WCA) potential is the Lennard-Jones potential truncated at the position of the minimum potential energy and then shifted up to have the cutoff at $r_{\text{cut}} = \sqrt[6]{2}\sigma$

$$\varphi_{\text{WCA}}(r_{ij}) = \begin{cases} 4\epsilon\left[\left(\dfrac{\sigma}{r_{ij}}\right)^{12} - \left(\dfrac{\sigma}{r_{ij}}\right)^{6}\right] + \epsilon & r_{ij} \leq \sqrt[6]{2}\sigma \\ 0 & \text{otherwise.} \end{cases} \tag{3.2}$$

It selects the repulsive part of the LJ potential and both of them are active between each pair of monomers. The main advantage of this potential is its extremely short range effect. This allows simulations to be carried out much more quickly than is possible with the longer-ranged LJ potential.

The third one, the *Finitely Extensible Nonlinear Elastic* (FENE) potential is only active between successive monomers and is representing elastic covalent bonds in a polymeric chain

$$\varphi_{\text{FENE}}(r_{ij}) = \begin{cases} -0.5KR_0^2 \ln\left[1 - \left(\dfrac{r_{ij}}{R_0}\right)^2\right] & r_{ij} < R_0 \\ 0 & \text{otherwise} \end{cases} \tag{3.3}$$

with K the elastic constant and R_0 the maximum extent of the bonds. Its name is self-explaining.

The work in this thesis has to do with simulations of polymer flows. They are usually modelled as bead-spring systems through a combination of the two previous types of potential: *FENE potential* (first attractive term) *and WCA potential* (second repulsive term), leading, for $r_{ij} < R_0$, to

$$\varphi_{\text{FENE+WCA}}(r_{ij}) = -0.5KR_0^2 \ln\left[1 - \left(\frac{r_{ij}}{R_0}\right)^2\right] + 4\epsilon\left[\left(\frac{\sigma}{r_{ij}}\right)^{12} - \left(\frac{\sigma}{r_{ij}}\right)^{6}\right] + \epsilon.$$

The potentials just described are illustrated in Figure 3.1.

3.1.2 Initialization

After reading parameters, choosing the shape of the box and the density of the fluid, the particles are placed on a lattice site at a distance such that they do not overlap and the system has the desired density. We set the temperature and the program assigns a

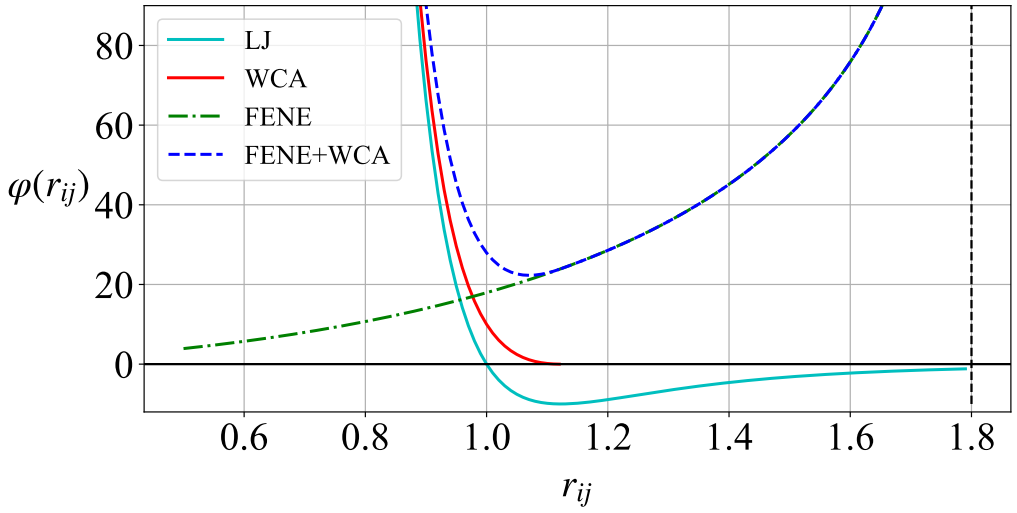

Figure 3.1: Trends of four interaction potentials with respect to the separation distance between the particles r_{ij}: the Lennard-Jones (LJ), the Weeks-Chandler-Andersen (WCA, repulsive part of LJ), the Finitely Extensible Non-linear Elastic (FENE) and a combination of the last two, tipically used to model polymers in MD simulations.

value drawn from a Maxwell-Boltzmann distribution to the velocity components. Subsequently, we shift all velocities, such that the total momentum is zero and we scale the resulting velocities to adjust the mean kinetic energy to the desired value. At the thermal equilibrium, the relation holds

$$\langle v_\alpha^2 \rangle = k_B \frac{T}{m} \tag{3.4}$$

where $k_B T$ is the wanted mean kinetic energy, v_α is one degree of freedom of the velocity and the previous equation is used to define the instantaneous temperature at time t

$$T(t) \equiv \frac{1}{k_B} \sum_{i=1}^{\mathrm{N}} \frac{m v_{\alpha,i}^2(t)}{\mathrm{N}_f}$$

where N is the total number of particles and N_f the total number of degrees of freedom. The adjustment of the instantaneous temperature $T(t)$ to match the target T is done by scaling all velocities with factor $(T/T(t))^{\frac{1}{2}}$.

3.2 Ensembles

The notion of *statistical mechanics ensemble* was introduced by J. W. Gibbs in 1902 and can be defined as a *probability distribution* for the state of the system. It formalises the idea that an experimenter repeating an experiment under the same macroscopic

conditions, but unable to control the microscopic details, may expect to observe a range of different outcomes.

The study of thermodynamics is concerned with systems that appear to human perception to be "static" (despite the motion of their internal parts), and which can be described simply by a set of macroscopically observable variables. These systems can be described by statistical ensembles that depend on a few observable parameters, and which are in statistical equilibrium (properties of the system do not change in time). Gibbs noted that different macroscopic constraints lead to different types of thermodynamical ensembles. He defined three

- *Microcanonical* (or NVE) ensemble, where the total energy and the number of particles of the system are fixed particular values; each member of the ensemble are required to have the same total energy and particle number. The system must remain totally *isolated* (unable to exchange energy or particles with its environment) in order to stay in statistical equilibrium.
- *Canonical* (or NVT) ensemble, where the energy is not known exactly but the number of particles is fixed. In place of the energy, the temperature and the volume are specified. The canonical ensemble is appropriate for describing a *closed* system which is in weak thermal contact with a heat bath. In order to be in statistical equilibrium, the system must remain totally closed (unable to exchange particles with its environment) and may come into weak thermal contact with other systems that are described by ensembles with the same temperature.
- *Grand canonical* ensemble when neither the energy nor the particle number are fixed, but the temperature and the chemical potential are specified. It is appropriate for describing an *open system*: one which is in weak contact with a reservoir (thermal, chemical, radiative and electrical contacts, ...). The ensemble remains in statistical equilibrium if the system comes into weak contact with other systems that are described by ensembles with the same temperature and chemical potential.

3.3 Periodic Boundary Conditions (PBCs)

Once the type and size of the main simulation cell, known as *primitive cell*, has been selected, it is filled with the number of particles required to achieve a certain density. This cell is then surrounded by identical cells containing particles, called *images*, which follow the same dynamics as the primitive particles. The structure of particles can be mathematically represented by a lattice of points and is schematically shown in Figure 3.2.

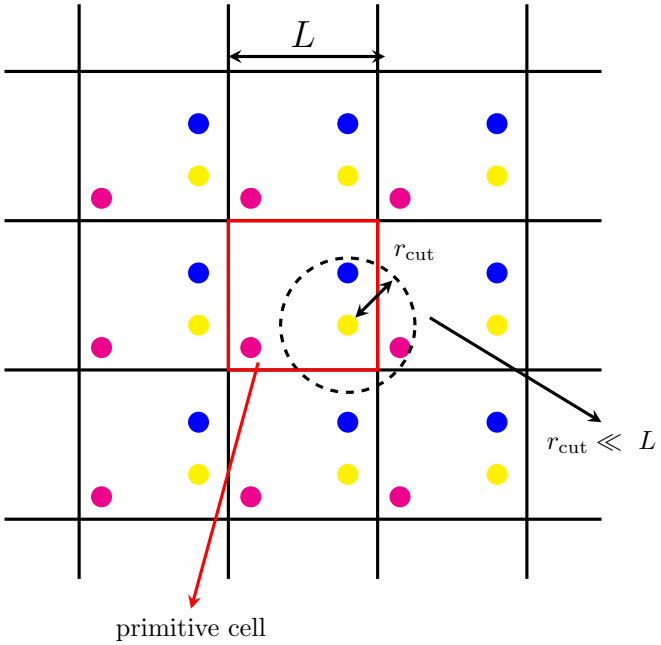

Figure 3.2: The primitive cell (red square) and the system of periodic boxes (black squares) is here represented. In the replicated boxes we have exactly a copy of each main particle, following exactly the same dynamics. Each particle is interacting, at each timestep, only with particles enclosed in the circle of radius r_{cut}.

3.3.1 PBCs in simple shear and extensional flows

We will begin by describing periodic boundary conditions devised by Lees & Edwards [44] for planar Couette flow, a boundary-driven shear flow.

Figure 3.3 shows a graphic representation of planar Couette flow in a periodic system with two particles per unit cell: this is a graphical simplification because in a computer simulation this number typically ranges from hundreds to hundreds of thousands. As the particles move under Newton's equations of motion, they feel the inter-atomic forces exerted by the particles within its cutoff radius whose positions are determined by the instantaneous lattice vectors of the periodic array of cells. The motion of the image cells defines the constant *shear rate*, $\dot{\gamma} \equiv \partial u_x / \partial y$. The origin of individual cells moves at the local *streaming velocity* of the fluid, given by

$$\boldsymbol{u}_{i,S}(\boldsymbol{r}) = \dot{\gamma} y \hat{\boldsymbol{x}}.$$

If the Reynolds number is sufficiently small and turbulence does not occur, we expect that the motion of image particles above and below any given cell will induce a linear velocity profile $\boldsymbol{u}(\boldsymbol{r})$ across the system. If particle moves out of the simulation cell it will be replaced by one of its periodic images. But if the particle moves through an upper

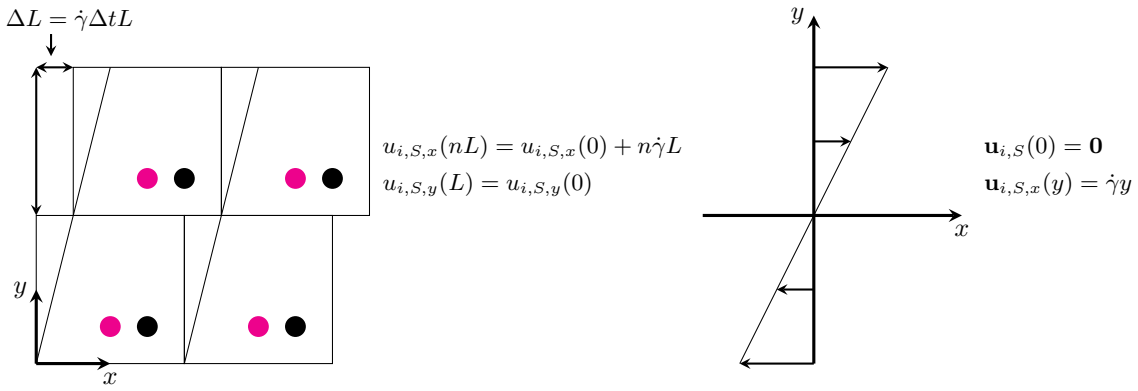

Figure 3.3: The left panel shows a periodic system of particles under a planar Couette flow. The streaming velocity $u_{i,S}$ at a particle position nL is given by the streaming velocity of the origin of the reference system superimposed by the contribution of the imposed flow. The right panel shows the velocity field of the applied (simple shear) flow.

face of a cell, the replacing image particle will not have the same laboratory velocity, nor necessarily the same x-coordinate.

We have depicted the Lees-Edwards boundary conditions in the so-called *sliding brick* representation. Consider now a simulation cube of side L, located so that the streaming velocity at the cube origin is zero (that is, the cube $(x, y, z) \in [0, L] \times [0, L] \times [0, L]$). The laboratory velocity of a particle i is then the sum of two parts: a peculiar or thermal velocity $\tilde{\boldsymbol{u}}_i$, and a streaming velocity $\boldsymbol{u}_{i,S}(\boldsymbol{r}_i)$, so the total momentum is

$$\dot{\boldsymbol{r}}_i = \tilde{\boldsymbol{u}}_i + \boldsymbol{u}_{i,S}(\boldsymbol{r}_i).$$

At $t = 0$ we have the usual periodic replication of the simulation cube where the boundary condition is

$$\boldsymbol{r}_i = (\boldsymbol{r}_i)_{\mathrm{mod}L}$$

with the modulus of a vector defined to be the vector of the moduli of the components. As the streaming velocity is a function of y, we need to consider explicitly boundary crossings in the y direction. At $t = 0$, $\boldsymbol{r}_i = (x_i, y_i)$ has images at $\boldsymbol{r}_i^{'} = \boldsymbol{r}_i + \hat{\boldsymbol{y}}L$, and $\boldsymbol{r}_i^{''} = \boldsymbol{r}_i - \hat{\boldsymbol{y}}L$. After time t, the positions of particle i and the two images are given by:

$$\boldsymbol{r}_i(t) = \boldsymbol{r}_i(0) + \int_0^t ds\dot{\boldsymbol{r}}_i(s) = \boldsymbol{r}_i(0) + \int_0^t ds(\tilde{\boldsymbol{u}}_i + \hat{\boldsymbol{x}}\dot{\gamma}y_i),$$

$$\boldsymbol{r}_i'(t) = \boldsymbol{r}_i(0) + \hat{\boldsymbol{y}}L + \int_0^t ds(\tilde{\boldsymbol{u}}_i' + \hat{\boldsymbol{x}}\dot{\gamma}(y_i + L)) = \boldsymbol{r}_i(0) + \hat{\boldsymbol{x}}\dot{\gamma}tL + \hat{\boldsymbol{y}}L + \int_0^t ds(\tilde{\boldsymbol{u}}_i' + \hat{\boldsymbol{x}}\dot{\gamma}y_i),$$

$$\boldsymbol{r}_i''(t) = \boldsymbol{r}_i(0) - \hat{\boldsymbol{y}}L + \int_0^t ds(\tilde{\boldsymbol{u}}_i'' + \hat{\boldsymbol{x}}\dot{\gamma}(y_i - L)) = \boldsymbol{r}_i(0) - \hat{\boldsymbol{x}}\dot{\gamma}tL - \hat{\boldsymbol{y}}L + \int_0^t ds(\tilde{\boldsymbol{u}}_i'' + \hat{\boldsymbol{x}}\dot{\gamma}y_i)$$

where $\tilde{\boldsymbol{u}}_i$ and y_i are functions of time. By definition, the peculiar velocities of a particle and its periodic images are equal, $\tilde{\boldsymbol{u}}_i = \tilde{\boldsymbol{u}}_i' = \tilde{\boldsymbol{u}}_i''$, so that

$$\begin{aligned}
\boldsymbol{r}_i(t) &= \boldsymbol{r}_i(0) + \int_0^t ds(\tilde{\boldsymbol{u}}_i + \hat{\boldsymbol{x}}\dot{\gamma} y_i), \\
\boldsymbol{r}_i'(t) &= \boldsymbol{r}_i(t) + \hat{\boldsymbol{x}}\dot{\gamma} t L + \hat{\boldsymbol{y}} L, \\
\boldsymbol{r}_i''(t) &= \boldsymbol{r}_i(t) - \hat{\boldsymbol{x}}\dot{\gamma} t L - \hat{\boldsymbol{y}} L.
\end{aligned}$$

If $\boldsymbol{r}_i(t)$ moves out horizontally from the primitive cube, it is physically replaced by the image particle at $\boldsymbol{r}_i'(t)$ and $\boldsymbol{r}_i^{\text{new}} = (\boldsymbol{r}_i')_{\text{mod}L}$. Else, if $\boldsymbol{r}_i(t)$ moves out of the simulation cube vertically, it is replaced by the image particle at $\boldsymbol{r}_i''(t)$, $\boldsymbol{r}_i^{\text{new}} = (\boldsymbol{r}_i'')_{\text{mod}L}$, or a combination of the two effects can happen. The change in the laboratory velocity of a particle is given by the time derivative of these two equations. There is a major difficulty with the boundary-driven algorithm. The way in which the boundaries induce a shearing motion to the particles takes time to occur, approximately given by the sound traversal time for the primitive cell. This is the minimum time taken for the particles to realize that the shear is taking place. The boundary-driven method above, therefore cannot be used to study time-dependent flows.

The SLLOD equations provide the way to skip the problem and have been proved to be valid for all homogeneous flows. They can be expressed as

$$\dot{\boldsymbol{r}}_i = \frac{\boldsymbol{p}_i}{m} + (\boldsymbol{r}_i \cdot \nabla)\boldsymbol{u} \qquad \dot{\boldsymbol{p}}_i = \boldsymbol{F}_i - (\boldsymbol{p}_i \cdot \nabla)\boldsymbol{u} \tag{3.5}$$

where the momenta $\boldsymbol{p}_i = m\tilde{\boldsymbol{u}}$ are taken to be *peculiar* (i.e. thermal) with respect to the streaming velocity $\boldsymbol{u}_{i,S}$ and its velocity gradient $\nabla\boldsymbol{u}$ (we omit the pedix). With this formulation we see well that any homogeneous motion represented by the velocity gradient $\nabla\boldsymbol{u}$, source of the mean velocity field, can be imposed on the system of periodic cells. The rate of change in position $\dot{\boldsymbol{r}}_i$ of a particle depends on the sum of its "thermal" fluctuation velocity and the streaming velocity at the position of the particle given by $\boldsymbol{u}(\boldsymbol{r}_i) = (\boldsymbol{r}_i \cdot \nabla)\boldsymbol{u}$. The second equation of 3.5 is the evolution of the peculiar momentum. The first term on the right-hand side denotes the sum $\boldsymbol{F}_i$ of the forces on particle i due to other particles. The second term couples the velocity field to the fluid. These equations of motion result in a homogeneous fluid in which all the particles are subjected to the same external field (i.e., velocity gradient), and their dynamics is described by the same evolution equations.

Even if SLLOD allow us to overcome difficulties in studying time-dependent flows and is luckily valid for all homogeneous flows it lacks of some important conservation properties about energy, pressure but also linear and angular momentum.

Equations (3.5) are used in conjunction with compatible Periodic Boundary Conditions (PBCs) and a homogeneous thermostat. For example, as reported in [62], in 1984 Nosé developed his now famous integral feedback thermostat and associated equations of motion that preserve initial canonical distribution for all time and for all size system. This approach was made more useful for simulations by Hoover and the resulting thermostat has been known thereafter as the Nosé-Hoover thermostat. For a system under influence of an external field, the Nosé-Hoover equations are given by

$$\begin{aligned}
\dot{\boldsymbol{r}}_i &= \frac{\boldsymbol{p}_i}{m} + (\boldsymbol{r}_i \cdot \nabla)\boldsymbol{u} \\
\dot{\boldsymbol{p}}_i &= \boldsymbol{F}_i - (\boldsymbol{p}_i \cdot \nabla)\boldsymbol{u} - \xi \boldsymbol{p}_i \\
\dot{\xi} &= \frac{1}{Q}\left[\sum_i \frac{\boldsymbol{p}_i^2}{m_i} - N_f k_B T\right]
\end{aligned}$$

where ξ is the Nosé-Hoover thermostat multiplier (inverse time units), and the target temperature T is related to the target kinetic energy K_0 by $T = 2K_0/N_f k_B$, where N_f is the number of degrees of freedom. Q is a parameter associated with an additional degree of freedom coupled to an external heat reservoir/bath and should be chosen to correctly determine the average kinetic energy and its fluctuations. This additional degree of freedom is what essentially scales the particle velocities to the desired kinetic temperature. For further details we refer the reader to Todd [62].

PBCs for extensional flows are a more sensitive issue. Kraynik & Reinelt [38] deviced a system of PBCs adapted to an extensional flow (uniaxial, biaxial and planar) sufficient to develop an algorithm to simulate boundary-driven extensional flows. In Fig. 3.2 is represented correctly the initial situation of the periodic system that should be, subsequently, rotated of an appropriate angle, as explained by KR, to satisfy the requirements of compatibility and reproducibility of particle lattice. The dynamics is generated through the SLLOD formulation of Newton's equations, that is still valid, as proved in the work by Daivis & Todd [10]. In this case, the motion is governed by the *strain rate* $\dot{\varepsilon} = \partial_x u_x = -\partial_y u_y$. The mean motion of a particle i (with vector position $\boldsymbol{r}_i$) is characterized by a "streaming" velocity that has two components

$$\boldsymbol{u}_{i,S}(\boldsymbol{r}_i) = \dot{\varepsilon} x_i \hat{\boldsymbol{x}} - \dot{\varepsilon} y_i \hat{\boldsymbol{y}}.$$

If particles move out of the simulation cell, they will be replaced by periodic images as illustrated previously in the simple shear case. The laboratory velocity of a particle is, again, the sum of a peculiar velocity and of the "streaming" one

$$\dot{\boldsymbol{r}}_i = \tilde{\boldsymbol{u}}_i + \boldsymbol{u}_{i,S}(\boldsymbol{r}_i).$$

For further details of PBCs in elongational flows we refer the reader to the next Chapter 4 about PBCs in mixed motions, which includes the extensional case as limit case. We referred also to Baranyiai & Cummings [3], B.Todd and P.J. Daivis [61], T. Hunt [32] and M. Dobson [11].

3.4 Reproducibility and compatibility

In MD simulations that we carried out for this study, the background flow was imposed by deforming the main simulation box. In the case of simple shear, the motion imposed by the Lees-Edwards conditions (sliding bricks) turns to be equivalent to the flow obtained through the direct shearing deformation of the box.

Deformation of the box over a long period of time can give some problems. In the extensional flow, for example, at a certain time t of the deformation it may happen that a particle is too close to some of its copies and starts to interact with them, altering the interaction force count. As we can observe in Figure 3.4 (right panel), when the box is too deformed, some of the copies of the magenta particle end up in the same interaction radius and also more than one copy of the green particle are interacting with the central magenta. This is not physically acceptable and computationally correct because the exact same interaction is counted several times for the purpose of calculating the forces.

In the case of simple shear this problem does not arise because the particles and their periodic copies are always at a distance equal to the size of the box L, even when the box is very elongated, see Figure 3.4 (left panel). And this guarantees that no more than one copy enters the range of interaction. However, when the box is too elongated, the algorithms to determine who the first neighbours are struggle and so we either flip the box when the deformation exceeds half the total length or re-initialize the deformed simulation box by mapping it onto the time $t = 0$ simulation box. In fact, this always contains exactly one periodic copy of each particle at each timestep, and so the simulation can continue undisturbed. The same re-initialization cannot be done at each timestep for extensional or mixed flows. In fact, as can be seen from the Figure 3.4 (right panel), by cutting out the initial box it will contain at time t more than one copy of each particle, making remapping to that situation inconvenient. For these reasons, the lattice points represented by the periodic system should meet *two requirements* for the simulation to be reliable and to be carried out for an indefinite time: *compatibility* and *reproducibility*.

Compatibility means that the minimum separation D of all lattice points (identical image particles) must exceed the cutoff range r_{cut} of interactions $D \gg r_{\text{cut}}$, since a particle must not interact with its copies or with more than one copy of other particles.

Reproducibility means instead that the lattice repeats itself periodically with the de-

formation. The correspondent period of time is called reproducibility period τ_p. The deformation of the system periodically returns to a state where replacing some of the original particles with their images the initial state boundaries are recovered. In correspondence to the time period the box should be re-initialized to allow the simulation to be still carried out. Reproducibility, usually, guarantees compatibility, but not viceversa. As already said, in simple shear the squared lattice is reproduced at any time, meaning at periods of time $\tau_p = 1$, thus can be re-initialized at any time. In the extensional case the lattice is not reproduced at any time. Kraynik & Reinelt [38] in 1992 found reproducibility conditions for the planar extensional motion, using a squared simulation box tilted of an angle $\vartheta = 0.55357435$, leading to a reproducibility period $\tau_p = 0.962424$.

In the next chapter, we are going to illustrate Periodic Boundary Conditions (PBCs) related to mixed flows and how we have been able to retrieve reproducibility for these cases.

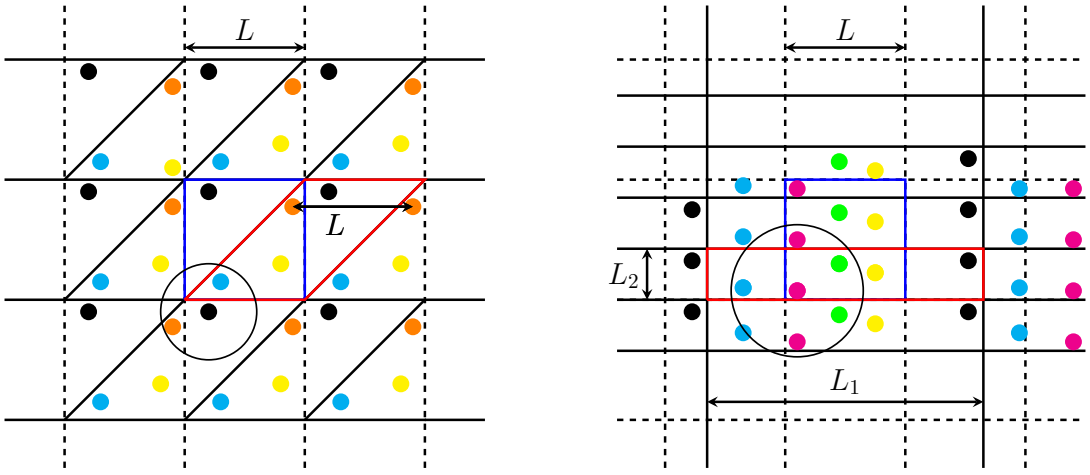

Figure 3.4: The left panel is representing the deformed lattice of points (undashed lines) under simple shear flow at a generic timestep t. Whatever t, in the initial simulation box (blue square) there is exactly a copy of each particle, thus, reproducibility is achieved. And compatibility guaranteed. In fact, each particle is interacting with only a copy of the other elements and is far from its images. In planar extensional motion (right panel) the situation is different. The deformed box (red rectangle), at a certain time t is too squashed. Compatibility is violated and reproducibility not guaranteed. In fact, the interaction area of the magenta particle contains two copies of the green particle and a copy of itself and this corrupts the right computation of pairwise forces. Moreover the initial box is including more than one image of the particles.

3.5 Force calculation

In our work, since we deal with pairwise additive interactions, we have to consider the contribution to the force on particle i due to all its *neighbors*, that are particles within the range of the potential cutoff r_{cut}. Once that is chosen and once the desired density for the system is established, the minimum box size is chosen r_{cut} much less than half the diameter L.

In that case we can always limit the evaluation of inter-molecular interactions between i and j to the interaction between i and the nearest periodic image of j. The vector distance between i and the nearest image of j is indicated by r_{ij} and is the first thing we compute. The list of neighbours is updated for each particle at each timestep.

Then all Cartesian components of r_{ij} are computed and finally r_{ij}^2. Next we test if r_{ij}^2 is less than r_{cut}^2, the square of the cutoff radius. If not, we immediately skip to the next value of j. If a given pair of particles is close enough to interact, we must compute the force contribution to the potential energy. The minimum image of particle j may be within the primitive cell, or in one of the surrounding image cells, see Fig. 3.2. One then finds all the minimum images particles for j, that lie within the potential cutoff distance $\boldsymbol{r}_c$ and compute the contributions to the force on i, $\boldsymbol{F}_i = \sum_{i<j} \boldsymbol{F}_{ij}$.

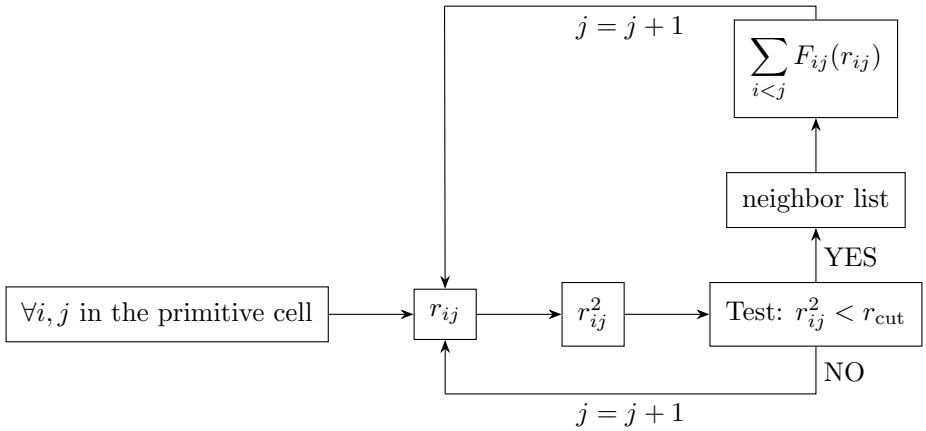

Figure 3.5: Schematic representation of the calculation of interaction forces between the particles in the primitive cell. For each particle i in the main cell we calculate its distance r_{ij} from every other particle of the primitive simulation box and check that this distance is less than the interaction radius r_{cut}, fixed by the potential. If so, particle j is inserted in the list of first neighbors (of i), the interaction force is calculated and we pass to consider a new particle j. Otherwise, particle j is not included in the list and the next ones are considered.

If, during the course of the motion, particle j leaves the primitive cell, it will be

replaced under the periodic boundary condition convention by an image of itself, travelling with exactly the same momentum, one lattice vector distant. A schematic representation of this process is shown in Fig. 3.5.

3.6 Integration of the equations of motion

Now that we have computed all forces between the particles, we can integrate SLLOD equations of motion for each particle. Omitting the pedix i to indicate that shown equations must be solved at any time for each particle, SLLOD equations can be written in our notation as

$$\begin{cases} \dot{\boldsymbol{r}} = \tilde{\boldsymbol{u}} + \boldsymbol{u}_S = \dfrac{\boldsymbol{p}}{m} + (\boldsymbol{r}\cdot\nabla)\boldsymbol{u} \\ \dot{\boldsymbol{p}} = m\dot{\tilde{\boldsymbol{u}}} = \boldsymbol{F}_\varphi - \boldsymbol{F}_S = \boldsymbol{F}_\varphi - (\boldsymbol{p}\cdot\nabla)\boldsymbol{u} \end{cases} \tag{3.6}$$

where $\boldsymbol{p} = m\tilde{\boldsymbol{u}}$ is the peculiar momentum and the "streming" velocity $\boldsymbol{u}_S$ is simply denoted by $\boldsymbol{u}$. If we set $\mathbf{A} = \nabla\boldsymbol{u}$ and $\boldsymbol{F}_\varphi = -\nabla\varphi$ we get

$$\begin{cases} \dot{\boldsymbol{r}} = \tilde{\boldsymbol{u}} + (\boldsymbol{r}\cdot\nabla)\boldsymbol{u} = \tilde{\boldsymbol{u}} + \mathbf{A}\boldsymbol{r} \\ \dot{\boldsymbol{u}} = m^{-1}\boldsymbol{F}_\varphi - (\tilde{\boldsymbol{u}}\cdot\nabla)\boldsymbol{u} = m^{-1}\boldsymbol{F}_\varphi - \mathbf{A}\tilde{\boldsymbol{u}} \end{cases} \tag{3.7}$$

thus, for each particle, at each timestep we must integrate two ODE equations

$$\begin{cases} \dot{\boldsymbol{r}} = \tilde{\boldsymbol{u}} + \mathbf{A}\boldsymbol{r} \\ \dot{\boldsymbol{u}} = m^{-1}\boldsymbol{F}_\varphi - \mathbf{A}\tilde{\boldsymbol{u}}. \end{cases} \tag{3.8}$$

Many algorithms have been designed to do this task. The Verlet methods in the *Velocity Verlet* formulation are seen as the gold-standard for molecular dynamics computations [24]. They require only one evaluation of $\nabla\varphi(\boldsymbol{r})$ per iteration, and offer a second-order symplectic evolution. It has a similar cost to the Euler method, if we measure cost in terms of force evaluations.

In our non-equilibrium simulations we use the Velocity Verlet algorithm directly applied to the SLLOD formulation of Newton's equations. It adds an intermediate step from a given vector $(\boldsymbol{r}^n, \boldsymbol{u}^n)$ to the next step vector $(\boldsymbol{r}^{n+1}, \boldsymbol{u}^{n+1})$ by the sequence of operations

$$\begin{cases} \boldsymbol{u}^{n+\frac{1}{3}} = e^{-\frac{\Delta t}{2}\mathbf{A}}\boldsymbol{u}^n \\ \boldsymbol{u}^{n+\frac{2}{3}} = \boldsymbol{u}^{n+\frac{1}{3}} + m^{-1}\boldsymbol{F}^{n+\frac{1}{3}}\Delta t \\ \boldsymbol{u}^{n+1} = e^{-\frac{\Delta t}{2}\mathbf{A}}\boldsymbol{u}^{n+\frac{2}{3}} \end{cases} \tag{3.9}$$

meaning with $\boldsymbol{F}^{n+\frac{1}{3}} = \boldsymbol{F}_\varphi(\boldsymbol{r}^{n+\frac{1}{3}})$, since we know that $\dot{\boldsymbol{u}} = -\mathbf{A}\boldsymbol{u} \rightarrow \boldsymbol{u}(t) = e^{-t\mathbf{A}}\boldsymbol{u}(0)$ and

$\dot{r} = \mathbf{A}\boldsymbol{r} \rightarrow \boldsymbol{r}(t) = e^{t\mathbf{A}}\boldsymbol{r}(0)$.

Parallel to the integration of the velocity $\boldsymbol{u}$, the integration of the position vectors $\boldsymbol{r}$ is performed in this way

$$\begin{cases} \boldsymbol{r}^{n+\frac{1}{3}} = e^{\frac{\Delta t}{2}\mathbf{A}}\boldsymbol{r}_n \\ \boldsymbol{r}^{n+\frac{2}{3}} = \boldsymbol{r}^{n+\frac{1}{3}} + \Delta t \boldsymbol{u}_n \\ \boldsymbol{r}^{n+1} = e^{\frac{\Delta t}{2}\mathbf{A}}\boldsymbol{r}^{n+\frac{2}{3}}. \end{cases} \tag{3.10}$$

3.7 Computation of the stress

We want to use MD to measure interesting properties of many-body systems, like quantities that can be compared with real experiments. Among these are the thermodynamic properties of the system under consideration, such as the temperature T, the pressure p, and the heat capacity C_V. The temperature is measured through equation (3.4).

While there are several different (but equivalent) ways to measure the pressure of a classical N-body system. The most common among these is based on the *virial equation* for the pressure, see Thompson [59] for references. `Lammps` makes use of an extension of the virial theorem written in tensorial form that allows to link the microscopic to the macroscopic pressure tensor of particles. Denoting, as usual, the peculiar velocities through $\tilde{\boldsymbol{u}}_i = \boldsymbol{u}_i - \boldsymbol{u}_{i,S}$, the pressure tensor can be expressed as

$$p = -\frac{1}{V}\left(\sum_i^N (m_i \tilde{u}_{i,\alpha}\tilde{u}_{i,\beta}) + \sum_i^N \sum_{j>i}^N (r_{ij,\alpha}F_{ij,\beta})\right)$$

where V is the volume and $\boldsymbol{r}_{ij}$ and $\boldsymbol{F}_{ij}$ are the distance and the force between particles i and j and $u_{i,\alpha}u_{i,\beta} = u_{i,\alpha} \otimes u_{i,\beta}$ and $r_{ij,\alpha}F_{ij,\beta} = r_{ij,\alpha} \otimes F_{ij}$ are tensorial products. The pressure tensor p corresponds to the opposite of the Cauchy stress tensor.

For what concerns the expression of the heat capacity at constant volume C_V we have

$$\langle K^2 \rangle_{\mathrm{NVT}} - \langle K \rangle^2_{\mathrm{NVT}} = \frac{3k_B^2 T^2}{2N}\left(1 - \frac{3k_B}{2C_V}\right)$$

where K is the average kinetic energy, N_f the number of degrees of freedom, k_B the Boltzmann constant and T the average temperature.

4

NEMD in mixed flows

In Chapter 2 we studied the velocity gradient $\nabla \boldsymbol{u}$ and the stress tensor $\boldsymbol{\sigma}$ in the basis of the eigenvectors $\hat{\boldsymbol{d}}_1, \hat{\boldsymbol{d}}_2$ of the strain rate tensor $\mathbf{D}$. However, it seems more convenient to use another frame of reference consisting of an eigenvector of the velocity gradient $\hat{\boldsymbol{v}}_1$ and its orthogonal complement $\hat{\boldsymbol{v}}_1^{\perp}$. In fact, we will see that using this basis which makes the gradient a superior triangular matrix will be particularly convenient for applying the deformation.

We will explain that to carry on a Molecular Dynamics simulation for an indefinite time, it is necessary to impose the right Periodic Boundary Conditions (PBCs), which guarantee reproducibility and compatibility of the lattice that forms our periodic system of particles. This allows the simulation box to be mapped back and to recover its initial shape, preserving physical properties and avoid simulation breakdown.

In simple shear motion the reproducibility is achieved at each timestep, because the initial cell contains always exactly one copy of each particle and to extend the simulation time indefinitely. For the extensional motion, however, Kraynik & Reinelt [38] showed that reproducibility of the lattice requires the introduction of an angle ϑ, popularly known as the magic angle, between one side of the initial box and an eigenvector of the velocity gradient $\nabla \boldsymbol{u}$. Baranyiai & Cummings [3] in 1999 applied the Kraynik and Reinelt PBCs (KR) to perform steady state nonequilibrium molecular dynamics simulation of planar elongation flow. Hunt, Bernardi and Todd [33] were the first in 2010 to extend the KR conditions to motions given by the linear combination between planar Couette and

extensional flows. They show that the most general form of mixed flow, in which the angle between the expanding, or contracting, direction and the velocity gradient axis varies, can be cast in a so-called canonical form, in which the angle assumes values that are multiples of π when a mixed flow exists, by an appropriate choice of the field parameters. In 2014, Dobson [11] generalized to the three-dimensional case the KR boundary conditions to flows represented by non-defective matrices. This has been done through multiple remappings of the simulation box. T. Hunt [32] in 2016 extended KR to the case of uniaxial extensional flows, obtaining simulations of arbitrary duration.

After this overview on NEMD extensional/mixed simulation techniques, we illustrate the method derived for planar intermediate flows, inspired by the work of Hunt, Bernardi and Todd [33], but using a different parameterization for $\nabla \boldsymbol{u}$ that leads to a different construction of the deforming cells. Our method follows more closely the derivation of KR PBCs. The reproducibility conditions require that the initial box will have aspect ratio a, orientation angle ϑ and reproducibility period τ_p that depend on a dimensionless flow-type parameter.

We implemented this algorithm in a software package that we called PMF (Planar Mixed Flows), written in C++ language. It has been inspired by the `UEF` package for simulating extensional flows by David Nicholson [51] that implements boundary conditions developed by Dobson [11] and Hunt [32].

Regarding this, there were several technical issues to deal with, but the crucial node is that the boundary conditions (and the relative integration of the motion) in `LAMMPS` require a simulation box that does not have a consistent alignment relative to the applied flow field: there is an angle ϑ between the eigenvector $\hat{\boldsymbol{v}}_1$ of the flow field and the initial position of one box side (let us say $\boldsymbol{l}_1(0)$). However, `LAMMPS` uses an upper-triangular matrix representing the evolving simulation box (meaning that the evolving box has always one side along the x direction), so it is not possible to express the evolved and evolving simulation box in the same coordinate system as the flow field, without changing basis at any time. So, `LAMMPS` keeps track of two systems: the `LAMMPS` frame in which one box side $\boldsymbol{h}_1(t)$ is aligned at any time to the x-axis (particularly convenient for computing positions, neighbours, potentials and forces) and the *flow frame* which is instead the natural frame for the integration of the motion, in which $\hat{\boldsymbol{v}}_1$ is aligned with the x-axis and have an angle $\vartheta + \psi(t)$ of separation with $\boldsymbol{l}'_1(t)$. We are going to outline the QR decomposition useful to pass from the representation of the box in the `LAMMPS` frame to its representation in the flow frame.

4.1 The velocity gradient in the flow frame

Following the pathway indicated by Kraynik and Reinelt [38], we found the conditions of reproducibility of a lattice under planar mixed flows, linear combination between the simple shear and the planar extension.

For convenience, we are going to use as flow parameter the amount of vorticity along the direction orthogonal to the flow plane β_3, as described in Chapter 2 and in Giusteri & Seto [25], but changed in sign, thus $\beta = -\beta_3$. In mixed conditions of flow this parameter spans $0 < \beta < 1$. We illustrate below a representation of the velocity gradient that is convenient for the implementation of periodic boundary conditions (pbcs) of mixed flows. Let us start from the representation of the velocity gradient with respect to the basis $\mathcal{B}$ of the eigenvectors $\boldsymbol{d}_1, \boldsymbol{d}_2$ of the strain rate tensor $\mathbf{D}$

$$(\nabla \boldsymbol{u})_{\mathcal{B}} = \begin{bmatrix} \dot{\varepsilon} & -\dot{\varepsilon}\beta \\ \dot{\varepsilon}\beta & -\dot{\varepsilon} \end{bmatrix} = \dot{\varepsilon} \begin{bmatrix} 1 & -\beta \\ \beta & -1 \end{bmatrix}.$$

Its symmetric part $\mathbf{D}$ and skew-symmetric part $\mathbf{W}$ take the form

$$\mathbf{D} = \dot{\varepsilon} \begin{bmatrix} 1 & 0 \\ 0 & -1 \end{bmatrix}, \qquad \mathbf{W} = \dot{\varepsilon} \begin{bmatrix} 0 & -\beta \\ \beta & 0 \end{bmatrix}$$

through the characteristic polynomial we find the eigenvalues of the velocity gradient

$$0 = \det\left((\nabla \boldsymbol{u})_{\mathcal{B}} - \lambda \mathbf{I}\right) = \lambda^2 + \dot{\varepsilon}^2\beta^2 - \dot{\varepsilon}^2 \quad \Rightarrow \quad \lambda_{1,2} = \pm\dot{\varepsilon}\sqrt{1-\beta^2}$$

and we search for the eigenvectors $\boldsymbol{v}_i$ in the kernel of the operator $f_i = (\nabla \boldsymbol{u})_{\mathcal{B}} - \lambda_i \mathbf{I}$, using, from this point on, the notation $(\nabla \boldsymbol{u})_{\mathcal{B}} = \nabla \boldsymbol{u}$

$$\mathrm{Ker}(f_i) = \{\boldsymbol{v}_i \in \mathbb{R}^2 \mid (\nabla \boldsymbol{u} - \lambda_i \mathbf{I})\boldsymbol{v}_i = 0\} \quad \forall i = 1, 2.$$

This leads to the resolution of the following trivial system of equations

$$(\nabla \boldsymbol{u})\, \boldsymbol{v}_1 = \lambda_1 \boldsymbol{v}_1, \qquad (\nabla \boldsymbol{u})\, \boldsymbol{v}_2 = \lambda_2 \boldsymbol{v}_2$$

setting $\boldsymbol{v}_1 = [x, y]^{\mathsf{T}}$ we get the following system of equations

$$\begin{bmatrix} \dot{\varepsilon} & -\dot{\varepsilon}\beta \\ \dot{\varepsilon}\beta & -\dot{\varepsilon} \end{bmatrix} \begin{bmatrix} x \\ y \end{bmatrix} = \dot{\varepsilon}\sqrt{1-\beta^2} \begin{bmatrix} x \\ y \end{bmatrix}, \qquad \begin{bmatrix} \dot{\varepsilon} & -\dot{\varepsilon}\beta \\ \dot{\varepsilon}\beta & -\dot{\varepsilon} \end{bmatrix} \begin{bmatrix} x \\ y \end{bmatrix} = -\dot{\varepsilon}\sqrt{1-\beta^2} \begin{bmatrix} x \\ y \end{bmatrix}$$

that transforms $\forall y, \forall \beta$ into

$$\begin{cases} x - \beta y = x\sqrt{1-\beta^2} \\ \beta x - y = y\sqrt{1-\beta^2} \end{cases} \quad \begin{cases} x - \beta y = x\sqrt{1-\beta^2} \\ x = \frac{y + y\sqrt{1-\beta^2}}{\beta} = \frac{y\left(1+\sqrt{1-\beta^2}\right)}{\beta} \end{cases} \quad \begin{cases} 0y = 0 \\ x = \frac{y\left(1+\sqrt{1-\beta^2}\right)}{\beta} \end{cases}$$

leading to the solution

$$\boldsymbol{v}_1 = \begin{bmatrix} \frac{1+\sqrt{1-\beta^2}}{\beta} \\ 1 \end{bmatrix}.$$

Setting $\boldsymbol{v}_2 = [x, y]^\mathsf{T}$ for the second eigenvector, we solve the algebraic equations and we obtain the following solutions $\forall y, \forall \beta$

$$\begin{cases} x - \beta y = -x\sqrt{1-\beta^2} \\ \beta x - y = -y\sqrt{1-\beta^2} \end{cases} \quad \begin{cases} x - \beta y = -x\sqrt{1-\beta^2} \\ x = \frac{y - y\sqrt{1-\beta^2}}{\beta} = \frac{y\left(1-\sqrt{1-\beta^2}\right)}{\beta} \end{cases} \quad \begin{cases} 0y = 0 \\ x = \frac{y\left(1-\sqrt{1-\beta^2}\right)}{\beta} \end{cases}$$

getting the second eigenvector

$$\boldsymbol{v}_2 = \begin{bmatrix} \frac{1-\sqrt{1-\beta^2}}{\beta} \\ 1 \end{bmatrix}.$$

Since $0 \leq \beta \leq 1$, we can check that the vectors are not unit-norm

$$\|\boldsymbol{v}_1\|^2 = \frac{2(1+\sqrt{1-\beta^2})}{\beta^2} \quad > 2(1+\sqrt{1-\beta^2}) > 2$$

$$\|\boldsymbol{v}_2\|^2 = \frac{2(1-\sqrt{1-\beta^2})}{\beta^2} \quad > 2(1-\sqrt{1-\beta^2}) > 1$$

thus, we normalize them obtaining the relative unit-norm eigenvectors

$$\begin{aligned} \hat{\boldsymbol{v}}_1 = \frac{\boldsymbol{v}_1}{\|\boldsymbol{v}_1\|} &= \left[\frac{1+\sqrt{1-\beta^2}}{\beta}, 1\right]^\mathsf{T} \cdot \frac{\beta}{\sqrt{2}\sqrt{1+\sqrt{1-\beta^2}}} \\ &= \left[\frac{\sqrt{2}}{2}\left(\sqrt{1+\sqrt{1-\beta^2}}\right), \frac{\sqrt{2}}{2\beta}\left(1-\sqrt{1-\beta^2}\right) \cdot \left(\sqrt{1+\sqrt{1-\beta^2}}\right)\right]^\mathsf{T} \end{aligned}$$

$$\begin{aligned} \hat{\boldsymbol{v}}_2 = \frac{\boldsymbol{v}_2}{\|\boldsymbol{v}_2\|} &= \left[\frac{1-\sqrt{1-\beta^2}}{\beta}, 1\right]^\mathsf{T} \cdot \frac{\beta}{\sqrt{2}\sqrt{1-\sqrt{1-\beta^2}}} \\ &= \left[\frac{\sqrt{2}}{2}\left(\sqrt{1-\sqrt{1-\beta^2}}\right), \frac{\sqrt{2}}{2\beta}\left(1+\sqrt{1-\beta^2}\right) \cdot \left(\sqrt{1-\sqrt{1-\beta^2}}\right)\right]^\mathsf{T}. \end{aligned}$$

We are going now to consider the vectorial basis $\mathcal{B}'$ in the Euclidean space $\mathbb{R}^2$, made of

one eigenvector and its orthogonal complement $\mathcal{B}' = \{\hat{\boldsymbol{v}}_1, \hat{\boldsymbol{v}}_1^{\perp}\}$. We denote with $\mathbf{M}_{\mathcal{B}\mathcal{B}'}$, the matrix of change of basis from $\mathcal{B}$ to $\mathcal{B}'$ that is a rotation in $\mathbb{R}^2$ and we use the following notation $\mathbf{R} = \mathbf{M}_{\mathcal{B}\mathcal{B}'}$ (and $\mathbf{R}^{\mathsf{T}} = \mathbf{M}_{\mathcal{B}'\mathcal{B}}$ for the inverse change of basis). The change of basis has the following representation

$$\mathbf{R} = \left[(\hat{\boldsymbol{d}}_1)_{\mathcal{B}'} \quad (\hat{\boldsymbol{d}}_2)_{\mathcal{B}'}\right] = \left[(\hat{\boldsymbol{v}}_1)_{\mathcal{B}} \quad (\hat{\boldsymbol{v}}_1^{\perp})_{\mathcal{B}}\right]^{\mathsf{T}}$$

$$= \begin{bmatrix} \frac{\sqrt{2}}{2}\left(\sqrt{1+\sqrt{1-\beta^2}}\right) & \frac{\sqrt{2}}{2\beta}\left(1-\sqrt{1-\beta^2}\right)\cdot\left(\sqrt{1+\sqrt{1-\beta^2}}\right) \\ -\frac{\sqrt{2}}{2\beta}\left(1-\sqrt{1-\beta^2}\right)\cdot\left(\sqrt{1+\sqrt{1-\beta^2}}\right) & \frac{\sqrt{2}}{2}\left(\sqrt{1+\sqrt{1-\beta^2}}\right) \end{bmatrix}$$

and the expression of the velocity gradient in the basis $\mathcal{B}'$ is retrieved through $\mathbf{R}$

$$(\nabla \boldsymbol{u})_{\mathcal{B}'} = \mathbf{R}(\nabla \boldsymbol{u})_{\mathcal{B}}\mathbf{R}^{\mathsf{T}} = \begin{bmatrix} \dot{\varepsilon}\sqrt{1-\beta^2} & -2\dot{\varepsilon}\beta \\ 0 & -\dot{\varepsilon}\sqrt{1-\beta^2} \end{bmatrix}.$$

Let $\mathbf{S}$ be the diagonalizing matrix of the velocity gradient and $\mathbf{S}^{-1}$ its inverse matrix, then $(\nabla \boldsymbol{u})_{\mathcal{B}} = \mathbf{S}\mathbf{D}_{\mathcal{B}}\mathbf{S}^{-1}$ with

$$\mathbf{S} = \begin{bmatrix} \frac{\sqrt{2}}{2}\left(\sqrt{1+\sqrt{1-\beta^2}}\right) & \frac{\sqrt{2}}{2}\left(\sqrt{1-\sqrt{1-\beta^2}}\right) \\ \frac{\sqrt{2}}{2\beta}\left(1-\sqrt{1-\beta^2}\right)\cdot\left(\sqrt{1+\sqrt{1-\beta^2}}\right) & \frac{\sqrt{2}}{2\beta}\left(1+\sqrt{1-\beta^2}\right)\cdot\left(\sqrt{1-\sqrt{1-\beta^2}}\right) \end{bmatrix}$$

$$\mathbf{S}^{-1} = \begin{bmatrix} \frac{\sqrt{\sqrt{1-\beta^2}+1}}{\sqrt{2}\sqrt{1-\beta_3^2}} & -\frac{\beta}{\sqrt{2}\sqrt{1-\beta^2}\sqrt{\sqrt{1-\beta^2}+1}} \\ \frac{\sqrt{1-\beta^2}-1}{\sqrt{2}\sqrt{1-\beta^2}\sqrt{1-\sqrt{1-\beta^2}}} & \frac{\beta}{\sqrt{2}\sqrt{1-\beta^2}\sqrt{1-\sqrt{1-\beta^2}}} \end{bmatrix}$$

and the relative diagonalized matrix is the following

$$\mathbf{D}_{\mathcal{B}} = \mathbf{S}^{-1}(\nabla \boldsymbol{u})_{\mathcal{B}}\mathbf{S} = \begin{bmatrix} \dot{\varepsilon}\sqrt{1-\beta^2} & 0 \\ 0 & -\dot{\varepsilon}\sqrt{1-\beta^2} \end{bmatrix}.$$

As a consequence, the matrix that diagonalizes $(\nabla \boldsymbol{u})_{\mathcal{B}'}$ is denoted with $\mathbf{S}'$

$$\mathbf{S}' = \mathbf{R}\mathbf{S} = \begin{bmatrix} 1 & \beta \\ 0 & \sqrt{1-\beta^2} \end{bmatrix}, \qquad \mathbf{S}'^{-1} = \mathbf{S}^{-1}\mathbf{R}^{\mathsf{T}} = \begin{bmatrix} 1 & -\frac{\beta}{\sqrt{1-\beta^2}} \\ 0 & \frac{1}{\sqrt{1-\beta^2}} \end{bmatrix}$$

since the following transformations are valid

$$\begin{aligned}(\nabla \boldsymbol{u})_{\mathcal{B}'} &= \mathbf{R}(\nabla \boldsymbol{u})_{\mathcal{B}}\mathbf{R}^{\mathsf{T}} \\ &= \mathbf{R}(\mathbf{S}\mathbf{D}_{\mathcal{B}}\mathbf{S}^{-1})\mathbf{R}^{\mathsf{T}} \\ &= (\mathbf{R}\mathbf{S})\mathbf{D}_{\mathcal{B}}(\mathbf{S}^{-1}\mathbf{R}^{\mathsf{T}}) \\ &= \mathbf{S}'\mathbf{D}_{\mathcal{B}}\mathbf{S}'^{-1}. \end{aligned} \tag{4.1}$$

The eigenvectors of $(\nabla \boldsymbol{u})_{\mathcal{B}'}$ have these components on the basis $\mathcal{B}'$

$$\hat{\boldsymbol{v}}_1 = \begin{bmatrix} 1 \\ 0 \end{bmatrix}, \qquad \hat{\boldsymbol{v}}_2 = \begin{bmatrix} \beta \\ \sqrt{1-\beta^2} \end{bmatrix}. \tag{4.2}$$

The need to express the velocity gradient $\nabla \boldsymbol{u}$ in the basis $\mathcal{B}'$ arises from the fact that `LAMMPS`, the software we use for Molecular Dynamics simulations, makes use of this frame to apply the flow deformation. For this reason it will be called *flow frame*. Furthermore, in `LAMMPS` all quantities are stored and used in another frame, called `LAMMPS` frame, which is the "intrinsic" frame of the simulation box, i.e. the frame in which one side of the box is always oriented along x.

4.1.1 The evolution operator

The deformation induced by an homogeneous velocity gradient $(\nabla \boldsymbol{u})_{\mathcal{B}'}$ on a fluid element of position $\boldsymbol{x} \in \mathbb{R}^2$ is described by the following ODE, which is an autonomous differential system with initial condition $\boldsymbol{x}_0 = \boldsymbol{x}(0) \in \mathbb{R}^2$

$$\begin{cases} \dot{\boldsymbol{x}} = (\nabla \boldsymbol{u})_{\mathcal{B}'}\boldsymbol{x} \\ \boldsymbol{x}_0 = \boldsymbol{x}(0). \end{cases}$$

Its flux is expressed by the matrix exponential applied to the vector $\boldsymbol{x}_0$

$$\boldsymbol{x}(t) = \Phi_t^{(\nabla \boldsymbol{u})_{\mathcal{B}'}}(\boldsymbol{x}_0) = \exp\left((\nabla \boldsymbol{u})_{\mathcal{B}'}t\right)\boldsymbol{x}_0.$$

In this case the velocity gradient is a diagonalizable matrix, thus, is easy to compute the matrix exponential as a function of time

$$\mathrm{F(t)} = \exp\left((\nabla \boldsymbol{u})_{\mathcal{B}'}t\right) = \begin{bmatrix} \exp\left(t\dot{\varepsilon}\sqrt{1-\beta^2}\right) & -\frac{\beta \exp\left(-t\dot{\varepsilon}\sqrt{1-\beta^2}\right)\left(-1+\exp\left(2t\dot{\varepsilon}\sqrt{1-\beta^2}\right)\right)}{\sqrt{1-\beta^2}} \\ 0 & \exp\left(-t\dot{\varepsilon}\sqrt{1-\beta^2}\right) \end{bmatrix} \tag{4.3}$$

that is an upper triangular matrix, depending from both the strain rate $\dot{\varepsilon}$ and the flow parameter β.

4.2 PBCs for planar mixed motions

Now we have the necessary tools to find the conditions under which a lattice of points in $\mathbb{R}^2$ turns out to be reproducible under mixed flow.

4.2.1 Reproducibility condition

Let us consider a lattice of points in $\mathbb{R}^2$, with a finite number m^2 of points. The coordinates of the i-th point in the lattice, expressed with respect to the basis $\mathcal{B}'$, are individuated at time $t = 0$ from the position vector $\mathbf{L}_i(0)$

$$\mathbf{L}_i(0) = \mathrm{N}_{i1}\mathbf{l}_1(0) + \mathrm{N}_{i2}\mathbf{l}_2(0), \qquad \mathrm{N}_{ij} \in \mathbb{Z}$$

which is a linear combination with integer coefficients of two basis vectors $\mathbf{l}_1(0), \mathbf{l}_2(0)$ that are collected in the matrix $\mathbf{L}(0)$

$$\mathbf{L}(0) = \begin{bmatrix} \mathbf{l}_1(0) & \mathbf{l}_2(0) \end{bmatrix}.$$

In our discussion, the base vectors represent the sides of the simulation box that evolve over time because of the applied flow field. Our simulation box is rectangular with longer side of length $||\mathbf{l}_1(0)|| = a$, the smaller side of length $||\mathbf{l}_2(0)|| = 1$ and rotated of an angle ϑ with respect to the first vector basis $\hat{\boldsymbol{v}}_1$. Thus, we have

$$\mathbf{l}_1(0) = \begin{bmatrix} a\cos\vartheta \\ a\sin\vartheta \end{bmatrix}, \qquad \mathbf{l}_2(0) = \begin{bmatrix} -\sin\vartheta \\ \cos\vartheta \end{bmatrix}.$$

and we search for the values of the initial angle of orientation ϑ that guarantees the reproducibility of the lattice.

Definition 4.2.1. *A lattice is reproducible if there* $\exists\, \tau_p \in \mathbb{R}_0^+$ *s.t. at time* $t = \tau_p$*, for each point in the lattice* $\forall i \in \{1, \ldots, m^2\}$*, there exists a couple* $(\mathrm{N}_{i1}, \mathrm{N}_{i2}) \in \mathbb{Z}^2$ *and some* j *s.t.*

$$\mathbf{L}_i(\tau_p) = \mathbf{L}_j(0) = \mathrm{N}_{i1}\mathbf{l}_1(0) + \mathrm{N}_{i2}\mathbf{l}_2(0).$$

The meaning of the previous equation is that, at a time τ_p, called *reproducibility period*, each point in the current (deformed) lattice individuated by position vector $\mathbf{L}_i$ overlaps some point $\mathbf{L}_j$ of the initial lattice, expressed thus with an appropriate linear

combination of initial vector basis. Since the lattice points are generated by basis vectors, it is sufficient to apply this condition to the basis vectors. The evolution of the initial vector basis at time τ_p is computed through the matrix exponential of the diagonalized velocity gradient

$$\begin{aligned}\mathbf{L}_i(t=\tau_p) &= \mathrm{F}(\tau_\mathrm{p})\,\mathbf{L}_i(0)\\ &= \exp\left((\nabla \boldsymbol{u})_{\mathcal{B}'}\tau_p\right)\mathbf{L}_i(0)\\ &= \exp\left(\mathbf{S}^{'}(\mathbf{D})_{\mathcal{B}}\mathbf{S}'^{-1}\tau_p\right)\mathbf{L}_i(0)\\ &= \mathbf{S}'\exp\left((\mathbf{D})_{\mathcal{B}}\tau_p\right)\mathbf{S}'^{-1}\mathbf{L}_i(0)\\ &= \mathbf{S}'\exp\left((\mathbf{D})_{\mathcal{B}}\tau_p\right)\mathbf{L}'_i(0)\end{aligned}$$

where $\mathbf{L}'_i(t) = \mathbf{S}'^{-1}\mathbf{L}_i(t)$ and $\mathbf{L}'_i(0) = \mathbf{S}'^{-1}\mathbf{L}_i(0)$, getting the transformed vectors

$$\mathbf{l}'_1(0) = \mathbf{S}'^{-1}\mathbf{l}_1(0) = \begin{bmatrix}1 & -\frac{\beta}{\sqrt{1-\beta^2}}\\ 0 & \frac{1}{\sqrt{1-\beta^2}}\end{bmatrix}\begin{bmatrix}a\cos\vartheta\\ a\sin\vartheta\end{bmatrix} = \begin{bmatrix}\frac{-a\beta\sin\vartheta + a\sqrt{1-\beta^2}\cos\vartheta}{\sqrt{1-\beta^2}}\\ \frac{a\sin\vartheta}{\sqrt{1-\beta^2}}\end{bmatrix}$$

$$\mathbf{l}'_2(0) = \mathbf{S}'^{-1}\mathbf{l}_2(0) = \begin{bmatrix}1 & -\frac{\beta}{\sqrt{1-\beta^2}}\\ 0 & \frac{1}{\sqrt{1-\beta^2}}\end{bmatrix}\begin{bmatrix}-\sin\vartheta\\ \cos\vartheta\end{bmatrix} = \begin{bmatrix}-\frac{\sqrt{1-\beta^2}\sin\vartheta + \beta\cos\vartheta}{\sqrt{1-\beta^2}}\\ \frac{\cos\vartheta}{\sqrt{1-\beta^2}}\end{bmatrix}.$$

Then, imposing the condition of reproducibility $\mathbf{L}'_i(\tau_p) = \mathrm{N}_{i1}\mathbf{l}'_1(0) + \mathrm{N}_{i2}\mathbf{l}'_2(0)$, we obtain for each lattice point $\forall i \in \{1,\dots,m^2\}$

$$\exp\left((\mathbf{D}_{\mathcal{B}})\tau_p\right)\mathbf{L}'_i(0) = \mathrm{N}_{i1}\mathbf{l}'_1(0) + \mathrm{N}_{i2}\mathbf{l}'_2(0) \tag{4.4}$$

with matrix exponential being

$$\exp\left((\mathbf{D}_{\mathcal{B}})\tau_p\right) = \exp\left(\begin{bmatrix}\dot{\varepsilon}\sqrt{1-\beta^2} & 0\\ 0 & -\dot{\varepsilon}\sqrt{1-\beta^2}\end{bmatrix}\tau_p\right)$$

and to simplify the notation we set $\lambda = e^{\tau_p\dot{\varepsilon}\sqrt{1-\beta^2}}$ and $\frac{1}{\lambda} = e^{-\tau_p\dot{\varepsilon}\sqrt{1-\beta^2}}$.

The existence of τ_p is strictly connected to the existence integer coefficients N_{ij} and is guaranted only for certain values of ϑ and aspect ratio a. We now impose the condition (4.4) onto the basis vectors

$$\exp\left((\mathbf{D})_{\mathcal{B}}\tau_p\right)\mathbf{l}'_i(0) = \mathrm{N}_{i1}\mathbf{l}'_1(0) + \mathrm{N}_{i2}\mathbf{l}'_2(0) \qquad i = 1,2$$

$$\begin{cases} i=1 \rightarrow & \exp\left((\mathbf{D})_{\mathcal{B}}\tau_p\right)\mathbf{l}'_1(0) = \mathrm{N}_{11}\mathbf{l}'_1(0) + \mathrm{N}_{12}\mathbf{l}'_2(0) \\ i=2 \rightarrow & \exp\left((\mathbf{D})_{\mathcal{B}}\tau_p\right)\mathbf{l}'_2(0) = \mathrm{N}_{21}\mathbf{l}'_1(0) + \mathrm{N}_{22}\mathbf{l}'_2(0) \end{cases}$$

and expliciting $\boldsymbol{l}'_i(0) = \left[\boldsymbol{l}'_{ix}(0), \boldsymbol{l}'_{iy}(0)\right]^{\mathsf{T}}$, with $i = 1, 2$, we obtain the following systems of scalar equations

$$\begin{cases} \lambda \mathrm{l}'_{1x}(0) = \mathrm{N}_{11}\mathrm{l}'_{1x}(0) + \mathrm{N}_{12}\mathrm{l}'_{2x}(0) \\ \frac{1}{\lambda}\mathrm{l}'_{1y}(0) = \mathrm{N}_{11}\mathrm{l}'_{1y}(0) + \mathrm{N}_{12}\mathrm{l}'_{2y}(0) \end{cases}, \qquad \begin{cases} \lambda \mathrm{l}'_{2x}(0) = \mathrm{N}_{21}\mathrm{l}'_{1x}(0) + \mathrm{N}_{22}\mathrm{l}'_{2x}(0) \\ \frac{1}{\lambda}\mathrm{l}'_{2y}(0) = \mathrm{N}_{21}\mathrm{l}'_{1y}(0) + \mathrm{N}_{22}\mathrm{l}'_{2y}(0) \end{cases}$$

that, re-combined, leads to the new systems

$$\begin{cases} \lambda \mathrm{l}'_{1x}(0) = \mathrm{N}_{11}\mathrm{l}'_{1x}(0) + \mathrm{N}_{12}\mathrm{l}'_{2x}(0) \\ \lambda \mathrm{l}'_{2x}(0) = \mathrm{N}_{21}\mathrm{l}'_{1x}(0) + \mathrm{N}_{22}\mathrm{l}'_{2x}(0) \end{cases} \qquad \begin{cases} \frac{1}{\lambda}\mathrm{l}'_{1y}(0) = \mathrm{N}_{11}\mathrm{l}'_{1y}(0) + \mathrm{N}_{12}\mathrm{l}'_{2y}(0) \\ \frac{1}{\lambda}\mathrm{l}'_{2y}(0) = \mathrm{N}_{21}\mathrm{l}'_{1y}(0) + \mathrm{N}_{22}\mathrm{l}'_{2y}(0). \end{cases}$$

If we set

$$\mathbf{l}'_x(0) = \begin{bmatrix} \mathrm{l}'_{1x}(0) \\ \mathrm{l}'_{2x}(0) \end{bmatrix}, \qquad \mathbf{l}'_y(0) = \begin{bmatrix} \mathrm{l}'_{1y}(0) \\ \mathrm{l}'_{2y}(0) \end{bmatrix}$$

we can re-write the systems in this compact matricial form

$$(\lambda \mathbf{I})\,\mathbf{l}'_x(0) = \begin{bmatrix} \mathrm{N}_{11} & \mathrm{N}_{12} \\ \mathrm{N}_{21} & \mathrm{N}_{22} \end{bmatrix} \mathbf{l}'_x(0), \qquad (\frac{1}{\lambda}\mathbf{I})\,\mathbf{l}'_y(0) = \begin{bmatrix} \mathrm{N}_{11} & \mathrm{N}_{12} \\ \mathrm{N}_{21} & \mathrm{N}_{22} \end{bmatrix} \mathbf{l}'_y(0)$$

and finally obtaining a spectral problem in $\mathbb{R}^2$

$$(\mathbf{N} - \lambda_k \mathbf{I})(\mathbf{l}'_k(0)) = 0, \qquad k = x, y \tag{4.5}$$

and $\mathbf{N} = [\mathrm{N}_{ij}] \in \mathrm{SL}(2, \mathbb{Z})$. To sum up, the problem we are trying to solve is the following: for a fixed homogeneous flow (β fixed), find an initial orientation angle ϑ and an aspect ratio a for the simulation box s.t. $\exists \mathbf{N} \in \mathrm{SL}(2, \mathbb{Z})$ that satisfies the equation (4.5).

Let us start by computing its characteristic polynomial (4.5)

$$p(z) = \lambda^2 - k\lambda + 1 = 0 \tag{4.6}$$

where the coefficients are characterized by these relations

$$\begin{aligned} k &= \lambda + \frac{1}{\lambda} = \mathrm{tr}\,\mathbf{N} = \mathrm{N}_{11} + \mathrm{N}_{22} \\ 1 &= \lambda\frac{1}{\lambda} = \det \mathbf{N} = \mathrm{N}_{11}\mathrm{N}_{22} - \mathrm{N}_{12}\mathrm{N}_{21}. \end{aligned} \tag{4.7}$$

The solution of the equation (4.6) is found for $\{k \leq 2 \cup k \geq 2\} \cap \mathbb{Z}$, but since $k = \lambda + \frac{1}{\lambda} > 0$ and excluding the trivial case $k = 2$, is represented by

$$\lambda, \frac{1}{\lambda} = \frac{k \pm \sqrt{k^2 - 4}}{2}, \qquad k \geq 3.$$

Equation (4.5) leads to two singular systems, whose first equations are

$$(\mathrm{N}_{11} - \lambda)\left(-a\beta \sin\vartheta + a\sqrt{1-\beta^2}\cos\vartheta\right) - \mathrm{N}_{12}\left(\sqrt{1-\beta^2}\sin\vartheta + \beta\cos\vartheta\right) = 0$$

$$a(\mathrm{N}_{11} - \frac{1}{\lambda})\sin\vartheta + \mathrm{N}_{12}\cos\vartheta = 0. \tag{4.8}$$

We consider a and ϑ as unknowns of the equation, while β, k, N_{11} and N_{12} as free parameters. β is the flux parameter and is set at the beginning, while $\mathrm{N}_{11}, \mathrm{N}_{12}$ and k are linked to τ_p. At this point, there are four possible scenarios that can happen

1. lucky case: nothing changes with respect to the extensional flow. The squared box with the same initial orientation angle $\vartheta = 0.553574$ and the same aspect ratio $a = 1$ is reproducible also under mixed flow fields
2. only the angle ϑ is adapting, while the aspect ratio a remains equal to the extensional case ($a = 1$)
3. only a is adapting, while $\vartheta = 0.553574$ is the same of the extension
4. both a and ϑ change and adapt to mixed conditions of flow.

We tried to get solutions from each of the three first cases, but none of them leads to meaningful results for the case of mixed motions. So the only way forward is the fourth one.

4.2.2 Parameters for mixed flows

Let us suppose to consider a specific mixed flow (β is fixed). We now look for solutions $(\mathrm{N}_{11}, \mathrm{N}_{12}) \in \mathbb{Z}^2$ to the equations (4.8).

Since $0 \leq \beta < 1$, for convenience, we interpret β as the cosine of an angle $0 \leq \Phi \leq \frac{\pi}{2}$

$$\beta = \cos\Phi, \qquad \sqrt{1-\beta^2} = \sin\Phi$$

which can be traced back, from (4.2), to the angle between the unit-norm eigenvectors $\hat{\boldsymbol{v}}_1$ and $\hat{\boldsymbol{v}}_2$ of the applied velocity gradient $(\nabla \boldsymbol{u})_{\mathcal{B}'}$. Let us divide by the cosine $\cos\vartheta$

equations (4.8), we get

$$-a\left(\mathrm{N}_{11}-\lambda\right)\left(\cos\Phi\tan\vartheta-\sin\Phi\right)-\mathrm{N}_{12}\left(\sin\Phi\tan\vartheta+\cos\Phi\right)=0$$

$$a\left(\mathrm{N}_{11}-\frac{1}{\lambda}\right)\tan\vartheta+\mathrm{N}_{12}=0.$$

N_{11} and N_{12} can be expressed with respect to the other parameters and take the expression

$$\mathrm{N}_{11}=\frac{\lambda^2+\cot\Phi\tan\vartheta-\lambda^2\cot\Phi\tan\vartheta+\tan^2\vartheta}{\lambda\left(1+\tan^2\vartheta\right)}$$
$$\mathrm{N}_{12}=\frac{a\tan\vartheta\left(1-\lambda^2-\cot\Phi\tan\vartheta+\lambda^2\cot\Phi\tan\vartheta\right)}{\lambda\left(1+\tan^2\vartheta\right)}.$$

We note that N_{11} does not depend on a. Since $\lambda=\frac{k+\sqrt{k^2-4}}{2}$, substituting this expression into N_{11} and N_{12} we get

$$\mathrm{N}_{11}=\frac{\cos^2\vartheta\left(-2+k^2+k\sqrt{k^2-4}-\left(-4+k^2+k\sqrt{k^2-4}\cot\Phi\tan\vartheta+2\tan^2\vartheta\right)\right)}{k+\sqrt{k^2-4}}$$
$$\mathrm{N}_{12}=-a\tan\vartheta\left(N_{11}-\frac{k-\sqrt{k^2-4}}{2}\right). \tag{4.9}$$

We look for solutions of the first equation proceeding by trial and errors with (N_{11} and N_{12}). We tried $\mathrm{N}_{11}=1$, but it does not lead to any solution, so we pass considering $\mathrm{N}_{11}=2$ and, using the following notation,

$$A=\cot\Phi$$
$$B=-4+k^2+k\sqrt{k^2-4}$$
$$C=k-1+\sqrt{k^2-4}$$
$$x=\cos^2\vartheta$$

from the first equation of (4.9), we get this second degree equation

$$B^2\left(A^2+1\right)x^2+\left(-A^2B^2-4BC\right)x+4C^2=0. \tag{4.10}$$

Let $x_{1,2}$ be its solutions, it is enough to keep the greater value, let us say x_1, and the relative angle of orientation with positive cosine $\vartheta=\arccos\left(\sqrt{x_1}\right)$, as k varies. From the second equation of (4.9), taking $\mathrm{N}_{12}=-1$ we get a meaningful expression for a, as k varies

$$a=\frac{1}{\tan\vartheta}\left(\mathrm{N}_{11}-\frac{k-\sqrt{k^2-4}}{2}\right).$$

And let us recall that the period of the reproducibility is linked to k through the following relation

$$\lambda = e^{\dot{\varepsilon}\tau_p\sqrt{1-\beta^2}} = \frac{k+\sqrt{k^2-4}}{2} \quad \Rightarrow \quad \tau_p = \frac{\log\left(\frac{k+\sqrt{k^2-4}}{2}\right)}{\dot{\varepsilon}\sqrt{1-\beta^2}}.$$

Through the software *Mathematica* we found easily the solutions reported in Table 4.1 about the the three parameters as functions of β, for values of k in the range $k \in \{3,4,5,6,7,8,9\}$.

k	ϑ	a	τ_p
3	$\frac{1}{2}\left(\arccos\beta - \arcsin\left(\frac{\sqrt{1-\beta^2}}{\sqrt{5}}\right)\right)$	$-\frac{2\sqrt{1-\beta^2}}{\sqrt{5}\beta-\sqrt{\beta^2+4}}$	$\frac{\log\left(\frac{3+\sqrt{5}}{2}\right)}{\dot{\varepsilon}\sqrt{1-\beta^2}}$
4	$\frac{\arccos\beta}{2}$	$\frac{\cot\left((\arccos\beta)/2\right)}{\sqrt{3}}$	$\frac{\log(2+\sqrt{3})}{\dot{\varepsilon}\sqrt{1-\beta^2}}$
5	$\frac{1}{2}\left(\arccos\beta + \arcsin\left(\frac{\sqrt{1-\beta^2}}{\sqrt{21}}\right)\right)$	$-\frac{2\sqrt{1-\beta^2}}{\sqrt{21}\beta-\sqrt{20+\beta^2}}$	$\frac{\log\frac{(5+\sqrt{21})}{2}}{\dot{\varepsilon}\sqrt{1-\beta^2}}$
6	$\frac{1}{2}\left(\arccos\beta + \arcsin\left(\frac{\sqrt{1-\beta^2}}{2\sqrt{2}}\right)\right)$	$\frac{\sqrt{2-2\beta^2}}{-4\beta+\sqrt{2}\sqrt{7+\beta^2}}$	$\frac{\log(3+2\sqrt{2})}{\dot{\varepsilon}\sqrt{1-\beta^2}}$
7	$\frac{1}{2}\left(\arccos\beta + \arcsin\left(\frac{\sqrt{1-\beta^2}}{\sqrt{5}}\right)\right)$	$\frac{2\sqrt{1-\beta^2}}{3(-\sqrt{5}\beta+\sqrt{4+\beta^2}}$	$\frac{\log\left(\frac{7+3\sqrt{5}}{2}\right)}{\dot{\varepsilon}\sqrt{1-\beta^2}}$
8	$\frac{1}{2}\left(\arccos\beta + \arcsin\left(\frac{2\sqrt{1-\beta^2}}{\sqrt{15}}\right)\right)$	$-\frac{\sqrt{1-\beta^2}}{\sqrt{15}\beta-\sqrt{11+4\beta^2}}$	$\frac{\log(4+\sqrt{15})}{\dot{\varepsilon}\sqrt{1-\beta^2}}$
9	$\frac{1}{2}\left(\arccos\beta + \arcsin\left(\frac{5\sqrt{1-\beta^2}}{\sqrt{77}}\right)\right)$	$-\frac{2\sqrt{1-\beta^2}}{\sqrt{77}\beta-\sqrt{52+25\beta^2}}$	$\frac{\log(9+\sqrt{77})}{\dot{\varepsilon}\sqrt{1-\beta^2}}$

Table 4.1: Orientation angles ϑ, aspect ratios a and reproducibility periods τ_p of a rectangular simulation box in mixed flows for different values of the parameter $k = \frac{1}{\lambda}$ related to the eigenvalues of the problem.

In Fig. 4.1 we have also shown the trends of a and ϑ, as k varies. The aspect ratio is a monotonically increasing function in β that tends to infinity for $|\beta| \to 1$ and tends to 1 for $\beta \to 0$. While it is a function with decreasing values as k increases. The orientation angle, instead, is a monotone function decreasing in β and increasing, as k changes. For $|\beta| \to 1$ we have $\theta \to 0$, and this is consistent with the fact that in simple shear motion the simulation box should not be initially rotated. For $|\beta| \to 0$ we recover the value of the

magic angle of the extensional case $\vartheta = 0.553574$. Looking at Fig. 4.2 it becomes clear that the reproducibility period has an increasing trend in k, monotonically increasing with respect to β and decreasing with respect to $\dot{\varepsilon}$. Any choice of k seems plausible and leads to sensible solutions, but it is more convenient to choose the smallest possible k because it corresponds to the smallest reproducibility period. The box will therefore be re-initialised at that timestep and this prevents it from being too deformed and from violating the flow compatibility requirement.

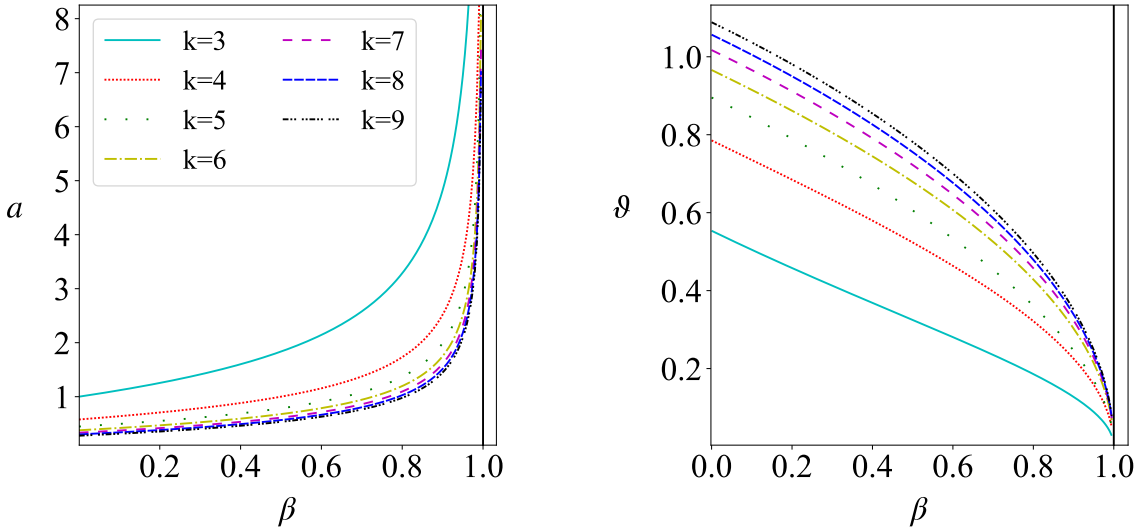

Figure 4.1: Aspect ratio a (left panel) and orientation angle (right panel) ϑ as functions of the flow parameter β of the initial simulation box in a mixed flow. Each colored line is representing the function for a precise value of the parameter $k = e^{\tau_p \dot{\varepsilon} \sqrt{1-\beta^2}}$, taken in the range $k \in \{3, 4, 5, 6, 7, 8, 9\}$. The aspect ratio in monotonously increasing in β and decreasing in k, assuming infinite value for $|\beta| \to 1$. The orientation angle is increasing in k and decreasing in β, reaching value zero as β approaches $|\beta| \to 1$.

To sum up, from the first equation of 4.9, substituting $k = 3$ we obtain

$$\mathrm{N}_{11} = \frac{1}{2}\left(3 - \sqrt{5}\left(\frac{\sin\left(2\vartheta - \Phi\right)}{\sin\Phi}\right)\right)$$

and, setting $\mathrm{N}_{11} = 2$, we obtai $\vartheta, \mathrm{N}_{12}$ as functions of the angle Φ and parameter a

$$\vartheta = \frac{1}{2}\left(\Phi - \arcsin\left(\frac{\sin\Phi}{\sqrt{5}}\right) + 2\pi c_1\right) \quad c_1 \in \mathbb{Z}$$

$$\mathrm{N}_{12} = \frac{1}{4}a\left(2\sqrt{5}\cos\Phi - \sqrt{2}\sqrt{9 + \cos\left(2\Phi\right)}\right)\frac{1}{\sin\Phi}.$$

Now, knowing that $\mathrm{N}_{12} = -1$ leads to meaningful solutions, we obtain this result for the

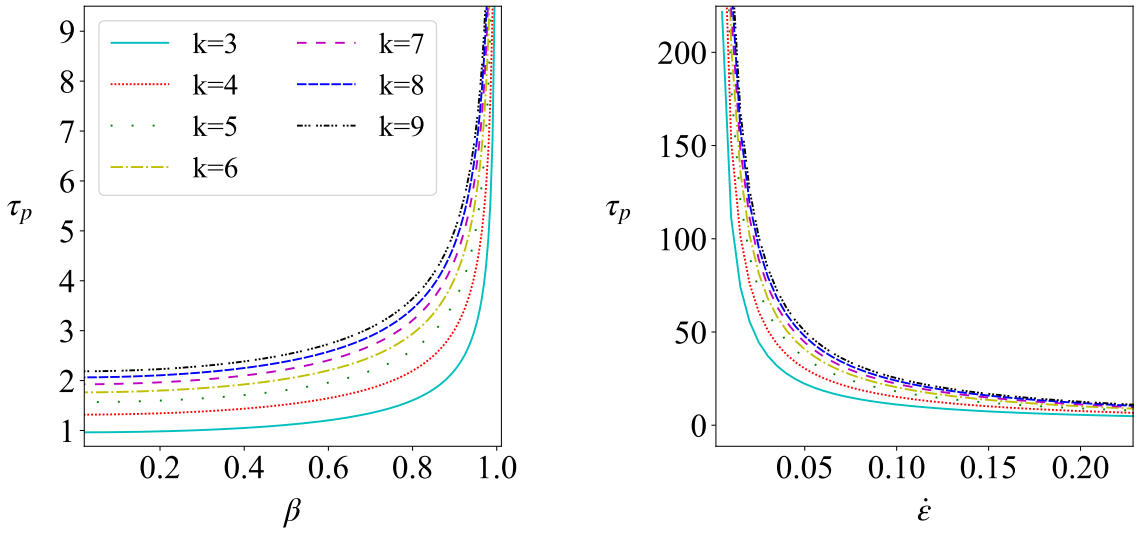

Figure 4.2: The period of reproducibility τ_p is a function of the flow parameter β and the strain rate $\dot{\varepsilon}$ and is here represented for $k \in \{3, 4, 5, 6, 7, 8, 9\}$. It is monotonic crescent function of β (left) and decrescent function of $\dot{\varepsilon}$ (right) with values that increase with k. The minimum value of k gives us the minimum period of reproducibility, that prevent us to have a too deformed simulation box.

aspect ratio

$$a = \frac{4 \sin \Phi}{-2\sqrt{5} \cos \Phi + \sqrt{2}\sqrt{9 + \cos(2\Phi)}}$$

and, since $\Phi = \arccos(\beta)$, we finally obtain a and ϑ as functions of β only

$$a = \frac{2\sqrt{1-\beta^2}}{\sqrt{4+\beta^2} - \sqrt{5}\beta} \tag{4.11}$$

$$\vartheta = \frac{1}{2}\left(\arccos\beta - \arcsin\left(\frac{\sqrt{1-\beta^2}}{\sqrt{5}}\right)\right) \tag{4.12}$$

and, as already said, for $k = 3$ the reproducibility period takes the form

$$\tau_p = \frac{\log\left(\frac{3+\sqrt{5}}{2}\right)}{\dot{\varepsilon}\sqrt{1-\beta^2}}. \tag{4.13}$$

$N_{11} = 2$ and $N_{12} = -1$ corresponds always to $N_{22} = 1$ and $N_{21} = -1$, for every chosen value of k. Let us further note that for $|\beta| \to 1$ the method has a singularity because $a \to \infty$, thus the found expression for the aspect ratio cannot be employed to simulate simple shear motion. For all the other values of $0 \leq \beta < 1$, choosing carefully an initial simulation box, with aspect ratio a tilted with an angle ϑ with respect to eigenvector $\hat{\boldsymbol{v}}_1$,

we are going to obtain reproducibility in mixed conditions of motion at periods of time τ_p: this means that, at such timestep, in the initial simulation box, we find exactly one copy of each particle. We can then re-initialize the box without losing relevant physical information and the simulation will proceed for, at least, the same period of time. In Fig. 4.3 there is a representation of the deformation of the box and the lattice reproducibility in the case $\beta = 0.6$.

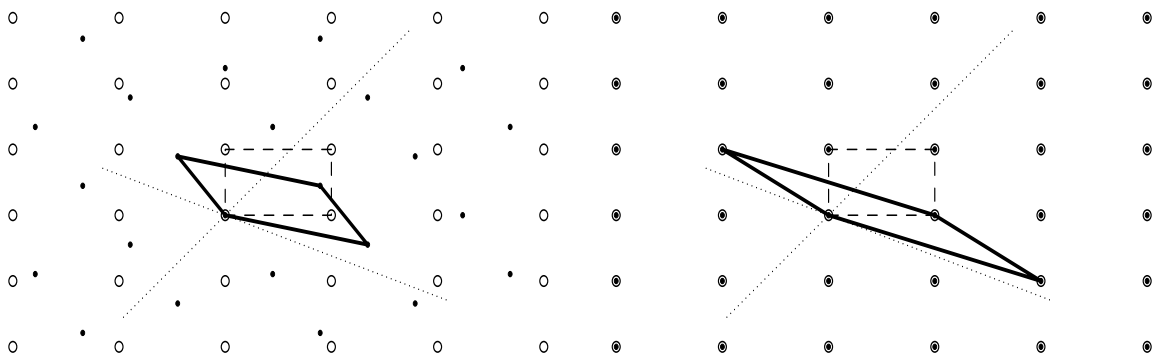

Figure 4.3: *Box deformation at a generic time $t \neq \tau_p$ (left) and at the reproducibility time $t = \tau_p$ (right) under a mixed motion of flow parameter* $\beta = 0.6$. Empty dots represent initial lattice points, while filled dots are the deformed points, dotted rectangle is the initial simulation box of aspect ratio $a = 2.143563$ and orientation angle $\vartheta = 0.28070777$. The correspondent reproducibility time amounts to $\tau_p = 1.20302956$. Bold box rectangle is the deformed box. Dotted lines are the (non-orthogonal) directions of the velocity gradient eigenvectors $\hat{\boldsymbol{v}}_1$, $\hat{\boldsymbol{v}}_2$.

4.3 PMF: a LAMMPS package for Planar Mixed Flows

In this section we would like to show the fundamental steps that have led to the construction of the software package in C++ for simulating planar mixed flows and that was included in the routines already implemented in `LAMMPS`. To do this, we have been inspired by the work of Kraynik & Reinelt [38] and by the work of Hunt, Bernardi and Todd [33]. The architecture of the code is, instead, based on the `UEF` package, designed by David Nicholson [51], and also the usage of two different frames (one for the integration of motion and the other for the rest of purposes). However we implemented a completely different algorithm, that has been applied to a different type of flows.

4.3.1 QR decomposition for the simulation box

Let us consider a planar mixed motion in three dimensions represented by the upper triangular velocity gradient $(\nabla \boldsymbol{u})_{\mathcal{B}'}$ and to the related evolution operator $\mathrm{F}_{\mathcal{B}'}(\Delta \mathrm{t})$ of equation 4.3 that is used in LAMMPS to perform the deformation of the simulation box.

As said in the introduction 4.2, LAMMPS makes use of two systems: the LAMMPS frame with one box side $\boldsymbol{h}_1(t)$ aligned at any time to the x-axis (particularly convenient for computing positions, neighbours, potentials and forces) and the *flow frame* where $\hat{\boldsymbol{v}}_1$ is aligned with the x-axis and has an angle $\vartheta+\psi(t)$ of separation with $\boldsymbol{l}_1'(t)$. The angle $\psi(t)$ is computed using the angle $\psi(\Delta t)$ that is added at any timestep because of the deformation (see right figure in Fig.4.4). Thus, the matrix of rotation from the LAMMPS frame to the flow frame during a timestep Δt is given by $\mathbf{Q} = \mathbf{Q}(\vartheta + \psi(t))$ where $\mathbf{Q} = \mathbf{Q}(\vartheta + N\psi(\Delta t))$ if N timesteps are already passed.

Since the product of rotations is commutative in $\mathbb{R}^2$, we can always decompose $\mathbf{Q}$ in the product of the two independent rotations of angle ϑ and $\psi(t)$, respectively

$$\mathbf{Q}(\vartheta + \psi(t)) = \mathbf{Q}(\psi(t)) \cdot \mathbf{Q}(\vartheta).$$

Therefore the evolution vectors of the box dimensions are the following in LAMMPS frame

$$\begin{cases} \boldsymbol{l}_1(t) = (x(t), 0, 0), & x(t) > 0 \quad \forall t \in \mathbb{R}^+ \\ \boldsymbol{l}_2(t) = (xy(t), y(t), 0), & y(t) > 0 \quad \forall t \in \mathbb{R}^+ \\ \boldsymbol{l}_3(t) = (xz(t), yz(t), z(t)), & z(t) > 0 \quad \forall t \in \mathbb{R}^+ \end{cases}$$

with $xz(t) = 0 = yz(t)$ and $z(t) = z(0),\ \forall t \in \mathbb{R}^+$ in planar motions. The three sides of the initial simulation box are codified in an upper triangular matrix

$$\mathbf{R}(t) = \left[\begin{array}{cc|c} x(t) & xy(t) & 0 \\ 0 & y(t) & 0 \\ \hline 0 & 0 & z(0) \end{array}\right].$$

At time $t = 0$ we have instead

$$\begin{cases} \boldsymbol{l}_1(0) = (l_x, 0, 0) & l_x = x(0) > 0 \\ \boldsymbol{l}_2(0) = (0, l_y, 0) & l_y = y(0) > 0 \\ \boldsymbol{l}_3(t) = (0, 0, l_z) & l_z = z(0) > 0 \end{cases}$$

where l_x, l_y, l_z are lenghts of the initial box sides.

During most molecular dynamics operations, the system is represented in the LAMMPS frame. Only when the positions and velocities must be updated the system is rotated to the flow frame, and then it is rotated back to the LAMMPS frame immediately afterwards. The simulation box $\mathbf{R}(t)$ is represented in the flow frame through the matrix $\mathbf{U}(t)$ obtained through the following QR decomposition

$$\mathbf{U}(\mathrm{t}) = \mathbf{Q}(\mathrm{t})\mathbf{R}(\mathrm{t})$$

where $\mathbf{Q}$ is the rotation matrix of the change of basis between the LAMMPS frame and the flow frame. Note that $\mathbf{R}$ is not the rotation matrix of the previous sections.

At any time, the angle $\vartheta + \psi(t)$, with $\psi(t) < 0$, is the angle between the deformed box side and the eigenvector $\hat{\boldsymbol{v}}_1$, as we can see in Figure 4.4.

$\mathbf{Q}(t)$ and $\mathbf{U}(t)$ have the following expression therefore

$$\mathbf{Q}(\mathrm{t}) = \left[\begin{array}{c|c} \tilde{\mathbf{Q}}(t) & \mathbf{0} \\ \hline \mathbf{0} & 1 \end{array}\right], \qquad \tilde{\mathbf{Q}}(t) = \begin{bmatrix} \cos(\vartheta + \psi(t)) & -\sin(\vartheta + \psi(t)) \\ \sin(\vartheta + \psi(t)) & \cos(\vartheta + \psi(t)) \end{bmatrix}$$

$$\mathbf{U}(t) = \begin{bmatrix} x(t)\cos(\vartheta + \psi(t)) & xy(t)\cos(\vartheta + \psi(t)) - y(t)\sin(\vartheta + \psi(t)) & 0 \\ x(t)\sin(\vartheta + \psi(t)) & xy(t)\sin(\vartheta + \psi(t)) - y(t)\cos(\vartheta + \psi(t)) & 0 \\ 0 & 0 & z(0) \end{bmatrix}.$$

4.3.2 Implementation issues

At this point we have involved four frames in this discussion

1. the basis of the orthogonal eigenvectors $\hat{\boldsymbol{d}}_1, \hat{\boldsymbol{d}}_2$ of the symmetric part $\mathbf{D}$ of velocity gradient $\nabla \boldsymbol{u}$, $\mathcal{B} = \{\hat{\boldsymbol{d}}_1, \hat{\boldsymbol{d}}_2\}$
2. the *flow frame* $\mathcal{B}' = \{\hat{\boldsymbol{v}}_1, \hat{\boldsymbol{v}}_1^{\perp}\}$, where $\hat{\boldsymbol{v}}_1$ is the eigenvector (elongation direction) of $(\nabla \boldsymbol{u})_{\mathcal{B}}$ and its orthogonal direction $\hat{\boldsymbol{v}}_1^{\perp}$. This basis is useful for the integration of the equations of the motion
3. the LAMMPS frame, anchored to one side of the simulation box $\boldsymbol{l}_1(t)$ and its orthogonal direction $\mathcal{B}'' = \{\hat{\boldsymbol{l}}_1(t), \hat{\boldsymbol{l}}_1^{\perp}(t)\}$. It is used for computing the updated positions, potential, forces and neighbors
4. the basis of the eigenvectors $\hat{\boldsymbol{v}}_1, \hat{\boldsymbol{v}}_2$ (extensional direction and contraction direction) of $\nabla \boldsymbol{u}$ is not orthogonal. This basis is particularly useful to compute the matrix exponential of the evolution. We denote it with $\mathcal{B}'''$.

In planar flows, during each timestep Δt, the orthogonal change of basis from $\mathcal{B}''$ to $\mathcal{B}'$ is made through the matrix $\tilde{\mathbf{Q}}(\vartheta + \psi(\Delta t))$

$$\tilde{\mathbf{Q}}(\vartheta + \psi(\Delta t)) = \begin{bmatrix} \cos(\vartheta + \psi(\Delta t)) & -\sin(\vartheta + \psi(\Delta t)) \\ \sin(\vartheta + \psi(\Delta t)) & \cos(\vartheta + \psi(\Delta t)) \end{bmatrix}$$

and the sides of the box (still to evolve $\boldsymbol{l}_i(0)$ and already evolved $\boldsymbol{l}'_i(t + \Delta t)$) in the two frames are linked in this way

$$\boldsymbol{l}'_i(t + \Delta t) = \tilde{\mathbf{Q}}(\vartheta + \psi(\Delta t))\boldsymbol{l}_i(t), \quad i = 1, 2.$$

and, since the product of rotations is commutative we have the following decomposition

$$\tilde{\mathbf{Q}}(\vartheta + \psi(\Delta t)) = \tilde{\mathbf{Q}}(\psi(\Delta t))\tilde{\mathbf{Q}}(\vartheta).$$

Moreover the deformation operator acting during the timestep Δt, in the basis $\mathcal{B}'$ is

$$\begin{aligned} F_{\mathcal{B}'}(\Delta t) &= \mathbf{S}' \exp\left((\nabla \boldsymbol{u})_{\mathcal{B}''' \Delta t}\right) \mathbf{S}'^{-1} \\ &= \begin{bmatrix} \exp(\dot{\varepsilon}\Delta t \sin\Phi) & \cot\Phi(\exp(-\dot{\varepsilon}\Delta t \sin\Phi) - \exp(\dot{\varepsilon}\Delta t \sin\Phi)) \\ 0 & \exp(-\dot{\varepsilon}\Delta t \sin\Phi) \end{bmatrix} \end{aligned}$$

where the velocity gradient in basis $\mathcal{B}'''$ is diagonal

$$(\nabla \boldsymbol{v})_{\mathcal{B}'''} = \dot{\varepsilon} \begin{bmatrix} \sin\Phi & 0 \\ 0 & -\sin\Phi \end{bmatrix}.$$

So, the box side $\boldsymbol{l}'_1(t)$ at time $t = t_0 + \Delta t$, i.e. evolved of only a timestep with respect to t_0, in the flow frame is obtained as

$$\begin{aligned} \boldsymbol{l}'_1(t + \Delta t) &= F_{\mathcal{B}'}(\Delta t)\boldsymbol{l}'_1(t) \\ &= \begin{bmatrix} \exp(\dot{\varepsilon}\Delta t \sin\Phi) & \cot\Phi(\exp(-\dot{\varepsilon}\Delta t \sin\Phi) - \exp(\dot{\varepsilon}\Delta t \sin\Phi)) \\ 0 & \exp(-\dot{\varepsilon}\Delta t \sin\Phi) \end{bmatrix} \begin{bmatrix} a\cos\vartheta \\ a\sin\vartheta \end{bmatrix} \\ &= \begin{bmatrix} \exp(\dot{\varepsilon}\Delta t \sin\Phi) a\cos\vartheta + \cot\Phi(\exp(-\dot{\varepsilon}\Delta t \sin\Phi) - \exp(\dot{\varepsilon}\Delta t \sin\Phi)) a\sin\vartheta \\ a\sin\vartheta \exp(-\dot{\varepsilon}\Delta t \sin\Phi) \end{bmatrix} \end{aligned} \tag{4.14}$$

and box sides $\boldsymbol{l}_i'(t)$ are periodic of period τ_p, meaning $\boldsymbol{l}_i'(t+\tau_p) = \boldsymbol{l}_i'(t)$, for $i = 1, 2$. The cosine and sine of the angle $\psi(t)$ can be retrieved by

$$\cos\psi(t) = \frac{\boldsymbol{l}_1'(t)\cdot\boldsymbol{l}_1'(0)}{a||\boldsymbol{l}_1'(t)||} \tag{4.15}$$

$$\sin\psi(t) = -\sqrt{1-\cos^2\psi(t)}. \tag{4.16}$$

The complete deformation operator, seen from the LAMMPS frame perspective, is

$$F_{\mathcal{B}''}(\Delta t) = \tilde{\mathbf{Q}}(\vartheta+\psi(t+\Delta t))^{\mathsf{T}} F_{\mathcal{B}'}(\Delta t)\tilde{\mathbf{Q}}(\vartheta+\psi(t)) \tag{4.17}$$

and this combination of transformation is illustrated in Figure 4.4. The side of the box $\boldsymbol{l}_1(t)$ in the LAMMPS frame is, first, rotated of an angle $\vartheta+\psi(t)$ (where ϑ is the angle between $\boldsymbol{l}_1(t)$ and $\hat{\boldsymbol{v}}_1$, while $\psi(t)$ is the accumulated angle from deformation at previous timesteps) and this brings the system in the flow frame. The deformation is then applied and a further angle $\psi(\Delta t)$ is accumulated. So, the system is remapped to the LAMMPS frame $\mathcal{B}''$ through the rotation $\tilde{\mathbf{Q}}(\vartheta+\psi(t+\Delta t))^{\mathsf{T}}$ of angle $-\vartheta-\psi(t)$. Through this operator we can find the evolved box sides in the LAMMPS frame $\mathcal{B}'$

$$\begin{bmatrix} x(t+\Delta t) \\ 0 \end{bmatrix} = F_{\mathcal{B}''}(\Delta t)\begin{bmatrix} x(t) \\ 0 \end{bmatrix}, \qquad \begin{bmatrix} xy(t+\Delta t) \\ y(t+\Delta t) \end{bmatrix} = F_{\mathcal{B}''}(\Delta t)\begin{bmatrix} xy(t) \\ y(t) \end{bmatrix}.$$

Thus, if $\boldsymbol{l}_1(0) = [l_x, 0]^{\mathsf{T}}$ and $\boldsymbol{l}_2(0) = [0, l_y]^{\mathsf{T}}$, with $l_x = a l_y$, and the evolved sides at time t are given by

$$x(t) = \frac{l_x}{2}e^{-\dot{\varepsilon}+\Delta t\sin\Phi}\left(1+e^{2\dot{\varepsilon}+\Delta t\sin\Phi}+\left(-1+e^{2\dot{\varepsilon}+\Delta t\sin\Phi}\right)\left(\frac{\sin 2\vartheta+3\Phi}{\sin\Phi}\right)\right)$$

$$y(t) = \frac{l_y}{2}e^{-\dot{\varepsilon}+\Delta t\sin\Phi}\left(1+e^{2\dot{\varepsilon}+\Delta t\sin\Phi}+\left(-1+e^{2\dot{\varepsilon}+\Delta t\sin\Phi}\right)\left(\frac{\sin 2\vartheta+3\Phi}{\sin\Phi}\right)\right)$$

$$xy(t) = l_y e^{-\dot{\varepsilon}+\Delta t\sin\Phi}\left(-1+e^{2\dot{\varepsilon}+\Delta t\sin\Phi}\right)\left(\frac{\sin(\vartheta+\Phi)}{\sin\Phi}\right).$$

4.4 User's Guide for the USER-PMF package

USER-PMF is a LAMMPS package for non-equilibrium molecular dynamics (NEMD) under mixed flow fields, linear combination between simple shear and extensional flow. With this package, simulations under intermediate flow may be carried out for an indefinite amount of time. It is an implementation of the boundary conditions developed in Section 4.2.

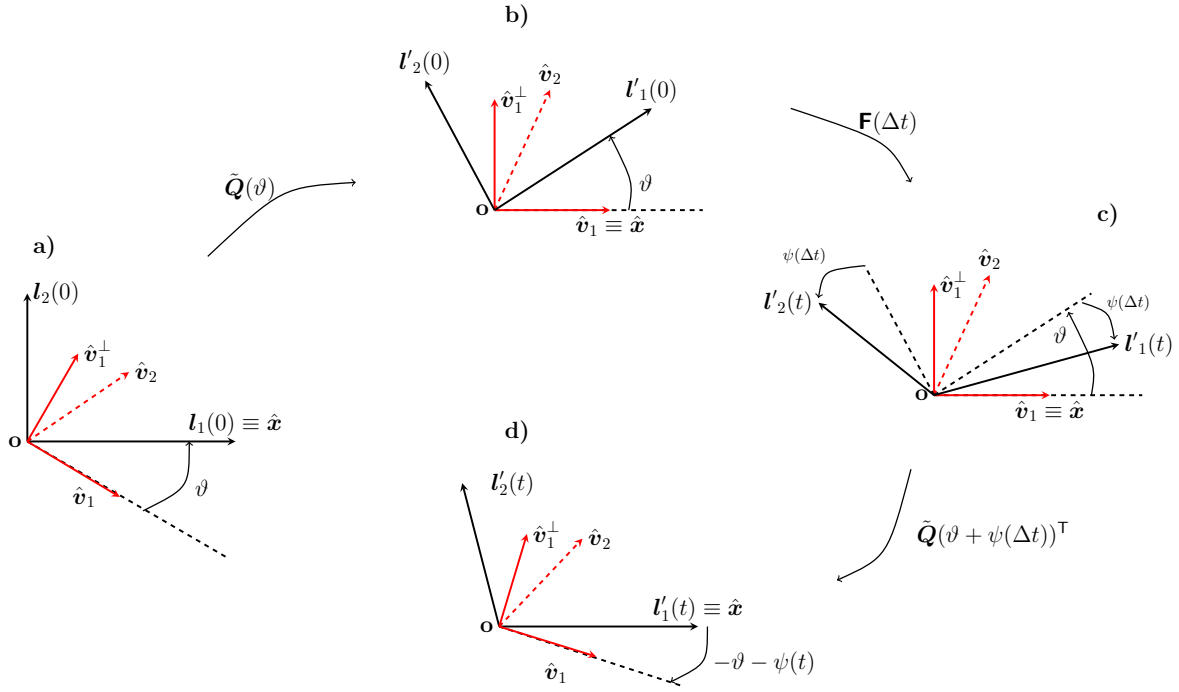

Figure 4.4: The figure a) is representative of the simulation box in the LAMMPS frame. Box sides $\boldsymbol{l}_1(0), \boldsymbol{l}_2(0)$ coincides with the x, y axis of the frame of reference. The box is orientated with an angle ϑ w.r.t. $\hat{\boldsymbol{v}}_1$. The transformation $\tilde{\mathbf{Q}}(\vartheta)$ leads the system in the flow frame, where is $\hat{\boldsymbol{v}}_1$ that is coinciding with the x-axis, panel b). Then, a deformation $\mathbf{F}(\Delta t)$ is applied to the box sides $\boldsymbol{l}'_1(t), \boldsymbol{l}'_2(t)$ that is adding an angle $\psi(\Delta t) < 0$ to ϑ, see panel c). To come back to the LAMMPS frame, we need to rotate the system with $\tilde{\mathbf{Q}}(\vartheta + \psi(t))^{\mathsf{T}}$ and $\boldsymbol{l}'_1(t)$ coincides again with the x-axis.

The package is intended for simulations of homogeneous flows, and integrates the SLLOD equations of motion.

4.4.1 Contents

- Usage
- fix nvt/pmf
- compute temp/pmf
- compute pressure/pmf
- dump cfg/pmf
- Implementation Details
- Error and Warning Messages

4.4.2 Usage

The package defines `fix nvt/pmf` and `fix npt/pmf` for constant volume controlled simulations, `compute pressure/pmf` and `compute temp/pmf` to compute the pressure and kinetic energy tensors, and `dump cfg/pmf` for outputting properly oriented atomic coordinates.

4.4.3 fix nvt/pmf

Syntax

```
fix ID group_ID nvt/pmf temp Tstart Tstop Tdamp strate eps beta b_value keywords
```

- `ID` = name for the fix
- `group_ID` = name of the group to which this compute is to be applied (if all atoms, use `all`)
- `Tstart, Tstop` = external temperature at start/end of run
- `Tdamp` = temperature damping parameter (time units)
- `eps` = strain rate in x dimension 1/(time units)
- `b_value` = vorticity value in the out-of-plane direction (adimensional)

Additional keywords:

- `strain` = initial level of strain (default=0). Use of this keyword is not recommended, but may be necessary when resuming a run from a data file. This keyword should be left unused when restart files are used.

The following additional keywords from `fix nvt` can be used with this fix: `tchain, tloop, drag`.

Usage notes

Due to requirements of the boundary conditions, when the `strain` keyword is unset, or set to zero, the initial simulation box must be rectangular with aspect ratio and tilting angle determined consistently with the value of the `b_value` keyword and have style triclinic. If the box is initially of type ortho, use the command `change box all triclinic` before invoking the fix.

This fix integrates the SLLOD equations of motion, which lead to an instability in the center of mass velocity, as for the extension. A `fix momentum` should be used to regularly reset the linear momentum. Additionally, this fix stores the peculiar velocity of each atom, defined as the velocity relative to the streaming velocity. This is in contrast to the `LAMMPS fix nvt/sllod` command, which stores the absolute velocity value in the lab-frame velocity.

This fix defines a `compute pressure/pmf` and `compute temp/pmf` that can be accessed at `c_ID_press` and `c_ID_temp` respectively for scalar values, or `c_ID_press[i]` and `c_ID_temp[i]` for the pressure and kinetic energy tensors.

When this fix is applied, any orientation-dependent vector or tensor-valued quantities computed, except for the tensors from `compute pressure/pmf` or `compute temp/pmf` and coordinates from `dump cfg/pmf`, will not be in the same coordinate system as the flow field. See the implementation details for further information.

This fix can be used with `write_restart` and `read_restart`, `run_style respa`, and `fix modify`, however custom pressure and temperature computes must be of type `pressure/pmf` and `temp/pmf`.

4.4.4 compute temp/pmf

Syntax

```
compute ID group_ID temp/pmf
```

- `ID` = name for the compute
- `group_ID` = name of the group to which this compute is to be applied (if all atoms, use `all`)

Examples

```
compute 1 all temp/pmf
```

Usage notes

This compute requires a `fix nvt/pmf` or `fix npt/pmf`. It computes the kinetic energy tensor in the reference frame of the flow field. See `LAMMPS` documentation for `compute temp` for further details on output.

4.4.5 compute pressure/pmf

Syntax

```
compute ID group_ID pressure/pmf temp-ID
```

- `ID` = name for the compute
- `group_ID` = name of the group to which this compute is to be applied (if all atoms, use `all`)
- `temp-ID` = ID of compute that calculates temperature

Additional keywords:

- The following additional keywords from `compute pressure` may be used with this fix: `ke` or `pair` or `bond` or `angle` or `dihedral` or `improper` or `kspace` or `fix` or `virial`.

Examples

```
compute 2 all pressure/pmf c_1_temp
```

Usage notes

This compute requires a `fix nvt/pmf` or `fix npt/pmf`. It computes the pressure tensor in the reference frame of the flow field.

The pressure tensor computed from `compute pressure/pmf` is only accurate if its temperature compute, specified by `temp-ID`, is a `compute temp/pmf`.

See the `LAMMPS` documentation for `compute pressure` for further details on output.

4.4.6 dump cfg/pmf

Syntax

```
dump ID group_ID cfg/pmf N file mass type xs ys zs keywords
```

- `ID` = name for the dump
- `group_ID` = name of the group to which this compute is to be applied (if all atoms, use `all`)
- `N` = dump every this many timesteps
- `file` = name of file to write dump info to.

Additional keywords:

- See the documentation for `dump cfg` for additional keywords.

Examples

```
dump 1 all cfg/pmf 100 dump.*.cfg mass type xs ys zs x y z ix iy iz
```

Usage notes

This command requires a `fix nvt/pmf` or `fix npt/pmf`. It outputs the atomic positions in the reference frame of the flow field. Only the positions are in the proper reference frame; if the atomic velocities are specified as an output, for example, they will not be in the flow field reference frame. See the `dump cfg` documentation for further information on writing trajectories with cfg files.

4.4.7 Implementation details

The simulation box used in the boundary conditions developed in section 4.2 does not have a consistent alignment relative to the applied flow field. `LAMMPS` utilizes an upper-triangular simulation box, making it impossible to express the evolving simulation box in the same coordinate system as the flow field. The PMF package keeps track of two coordinate systems: the flow frame, and the `LAMMPS` frame in which the box is represented by an upper triangular matrix. The coordinate systems are related to each other through the QR decomposition illustrated in Section 4.3.1.

During most molecular dynamics operations, the system is represented in the `LAMMPS` frame. Only when the positions and velocities are updated is the system rotated to the flow frame, and it is rotated back to the `LAMMPS` frame immediately afterwards. For this reason, all vector-valued quantities (except for the tensors from `compute pressure/pmf` and `compute temp/pmf` will be computed in the `LAMMPS` frame. Rotationally invariant scalar quantities like the temperature and hydrostatic pressure, on the other hand, will be computed correctly. Additionally, the system is in the `LAMMPS` frame during all of the output steps, and therefore trajectory files made using the dump command will be in the `LAMMPS` frame unless the `dump cfg/pmf` command is used.

4.4.8 Error and Warning Messages

The methods described with inherit error/warning messages from `fix npt/nvt`, `compute pressure` and `dump cfg`. Additional error messages associated with this package are the same founded fo the UEF package, explained in the relative section of git hub page, `https://github.com/RutledgeGroupMIT/UEF#error-and-warning-messages`. Just replace the word "`uef`" with "`pmf`".

5

The multiscale method

Modelling and computational simulation of non-Newtonian fluids is a challenging problem, since these fluids exhibit complex effects, such as shear thinning or thickening, viscoelasticity or flow-induced phase separation. A detailed analysis of the rheology of complex fluids can be obtained by particle-based simulations. Clearly, such micro-scale description is accurate but computationally very expensive and cannot be applied to engineering-scale problems. Consequently, new mathematical algorithms and hybrid multi-scale approaches have been proposed in recent years.

In the literature, we can find several hybrid models combining particle dynamics with a macroscopic continuum model, such as the heterogeneous multi-scale methods [12, 15, 14, 17, 23, 65], the triple-decker atomistic-mesoscopic-continuum method [20, 21], the seamless multi-scale methods [13, 16, 18], the equation-free multi-scale methods [35, 36, 37] or the internal-flow multi-scale method [4, 5]. In [50] software requirements and design principles are presented and illustrated for a prototype coupling between molecular dynamics and Lattice Boltzmann methods. Note that, in general, hybrid multi-scale approaches are successful when processes occurring on a small scale are only loosely coupled with the large-scale behavior, that is, in the presence of an effective scale separation [2]. In keeping with this, our method is applicable when the local flow conditions experienced by a fluid element change on a much larger timescale than the microscopic relaxation time necessary to achieve a statistically steady state of the molecular conformation and interactions.

We should mention also the Feigl's work [22] and Laso's [43] work on viscoelastic flows and Hulsen [30] on Brownian configurations who were among the first to use standard finite element

techniques for solving the momentum and continuity equations by replacing the integral or differential constitutive equation, traditionally used to compute polymer stresses, with stochastic simulations of polymer dynamics.

The aim of the study illustrated in Tedeschi [58] and reported in this chapter is to provide a new heterogeneous multi-scale method for the simulation of flows of complex fluids in generic geometries and different conditions of motion. We extend and generalize the idea presented in [56], where a heterogeneous multi-scale method is developed for polymeric solutions subjected to simple shear flows. Simple shear is very well investigated for it is more easily realized in experiments than other flows. It provides fundamental information that is often sufficient to characterize simple fluids. However, complex fluids show a molecular structure that is able to change with respect to different conditions of motion, geometries, but also time scales and deformation rates. Therefore, to retrieve important rheological information about the stress response of such fluids, their behavior is studied under conditions of flow different from steady simple shear, for example extensional motions, startup flows and oscillating shear [48]. Moreover, it is also fundamental, for these types of materials, to consider flows in complex geometries that contain holes, barriers, contractions or other irregular features, because in close proximity of these structures the fluid is subject to local motions that are not equivalent to simple shear and can manifests some unexpected behavior.

We focus our efforts on the development of a method to link the micro-scale rheological information, available from simulations in different local flow types, to macro-scale flows in complex geometries. The main aim of this work is to show that it is necessary to correctly take into account the local flow type, which plays an important role in modifying the stress response in non-viscometric flows of non-Newtonian fluids featuring a flow-type dependent rheology, such as polymeric fluids. While simulations based on constitutive assumptions do take into account, by construction, the possible flow type dependence incorporated at the level of constitutive laws, multi-scale methods for fluid mechanics application has so far considered simple shear flows as the only source of information for the micro-to-macro coupling. With our approach, we overcome this severe limitation. The method is applied to planar flows, but it can be extended to more general three-dimensional flows. The most challenging task for such an extension will be to implement MD simulations under arbitrary local flow conditions.

5.1 Micro-scale data and macro-scale simulations

At the heart of our proposal there is the understanding that the local kinematics of a generic planar flow must be identified by *at least* two parameters, one measuring the speed of the deformation and the other measuring the local flow type (see Chapter 2, Section 2.1 for a discussion of this point). While there is ample agreement about measuring the deformation rate in generic situations by means of $\dot{\varepsilon}$, different choices can be made for the flow-type parameter, depending on the type of material response that we envision (see [25], Section III). Here we

choose β_3 for its simplicity and we stress that, to make it a frame-indifferent parameter, we consider it as measured relative to the vanishing spin of a fixed inertial frame of reference. In other contexts, different choices may be appropriate (such as the relative rotation rate proposed by Schunk and Scriven [54]), but the structure of the scheme that we are going to present remains the same.

The local kinematic parameters $\dot{\varepsilon}$ and β_3 are the macro-scale input of micro-scale simulations that will in turn give an ensemble-averaged stress tensor $\boldsymbol{\sigma}$. To be able to use the micro-scale information encoded in $\boldsymbol{\sigma}$ we must express it in a form that is independent of the coordinates, because coordinates that are chosen for computational convenience cannot always be coherent when we pass from the micro- to the macro-scale simulation. We can achieve this independence by decomposing the stress to an orthogonal tensorial basis built on $\mathbf{D}$ (see [25] or Chapter 2, Section 2.3 for details and significance of this decomposition). For the case of planar incompressible flows, we have

$$\boldsymbol{\sigma} = -p\mathbf{I} + 2\eta\mathbf{D} + 2\lambda_3\mathbf{G}_3, \tag{5.1}$$

where $\mathbf{I}$ is the identity tensor and for $\mathbf{G}_3$ we use this straightforward expression

$$\mathbf{G}_3 = \tfrac{1}{2}\left(\mathbf{AD} - \mathbf{DA}\right) \quad \text{with} \quad \mathbf{A} = \begin{bmatrix} 0 & -1 \\ 1 & 0 \end{bmatrix}. \tag{5.2}$$

The coefficients of the linear decomposition (5.1) have been extensively described in Chapter 2, Section 2.3 and can be retrieved from the computational data in any coordinates by computing

$$p = -\frac{\boldsymbol{\sigma} : \mathbf{I}}{\|\mathbf{I}\|^2} = -\frac{1}{3}\mathrm{tr}\left(\boldsymbol{\sigma}\right), \qquad \eta = \frac{1}{2}\frac{\boldsymbol{\sigma} : \mathbf{D}}{\|\mathbf{D}\|^2}, \qquad \lambda_3 = \frac{1}{2}\frac{\boldsymbol{\sigma} : \mathbf{G}_3}{\|\mathbf{G}_3\|^2}. \tag{5.3}$$

For the sake of clarity, we indicate with $\tilde{\eta}$ and $\tilde{\lambda}_3$ the two material functions of the kinematic parameters $(\dot{\varepsilon}, \beta_3)$, reconstructed by sampling the two-dimensional parameter space. In this way, we obtain from computational rheological measurements the constitutive expression

$$\boldsymbol{\sigma} = -p\mathbf{I} + 2\tilde{\eta}(\dot{\varepsilon}, \beta_3)\mathbf{D} + 2\tilde{\lambda}_3(\dot{\varepsilon}, \beta_3)\mathbf{G}_3 \tag{5.4}$$

for the stress tensor, that can be used in performing the macro-scale continuum simulations. There is no need to define a pressure function because it is determined, at the macro-scale, as the Lagrange multiplier of the incompressibility constraint.

5.2 Micro-scale NEMD simulation

The NEMD simulation at the micro-scale is performed using LAMMPS (`lammps.sandia.gov`), see Plimpton [53]. We consider both monomeric and polymeric aggregates in a three-dimensional computational domain with periodic boundary conditions and undergoing two different planar flows: simple shear and extensional flow. The average velocity field is imposed by suitably de-

forming the computational box and the canonical ensemble statistics of the velocity fluctuations is achieved via the classical Nosé–Hoover thermostat [24]. For the case of simple shear we use the LAMMPS command `fix deform` in conjunction with the SLLOD algorithm [10], while the extensional flow is treated by means of the UEF package [51]. The latter implements boundary conditions developed by Dobson [11] and Hunt [32], that are an extension of the boundary conditions of Kraynik and Reinelt [38]. We will discuss results for monomers, $N_{\mathrm{pol}} = 1$, and polymers, $N_{\mathrm{pol}} = 20$, where N_{pol} is the number of monomers per molecule.

5.2.1 Interaction potentials

We choose an interatomic interaction potential of the FENE+WCA type, which has been extensively described in Chapter 3 (Section 3.1.1) and which is typical for modelling polymers as bead-spring systems

$$\varphi_{\mathrm{FENE+WCA}}\left(r_{ij}\right) = -0.5KR_0^2 \ln\left[1 - \left(\frac{r_{ij}}{R_0}\right)^2\right] + 4\epsilon\left[\left(\frac{\sigma}{r_{ij}}\right)^{12} - \left(\frac{\sigma}{r_{ij}}\right)^{6}\right] + \epsilon.$$

The attractive FENE part is only active between adjacent monomers, whereas the repulsive WCA part is also active between non-adjacent monomers.

5.2.2 Average stress coefficients

We considered values of the deformation rate $\dot{\varepsilon}$ ranging from 0.001 s^{-1} to 1 s^{-1}. For each value of $\dot{\varepsilon}$ we performed 21 simulations with different initial configurations of the particles. The simulations were conducted at a temperature (of the fluctuations around the mean motion) equal to $T = 1\frac{k_B}{\varepsilon}$, the density of the system is $\rho = 0.8\frac{m}{\sigma^2}$. The total number of particles involved depends on the type of the polymer: in the monomeric case is $N_1 = 1000$ while in the polymeric case is $N_{20} = 800$ and the length of the used simulation box is $L = 10.77217\sigma$. Equilibrium times range from $10\sqrt{\frac{m\sigma^2}{\epsilon}}$ for $\dot{\varepsilon} = 0.001$ and $N_{\mathrm{pol}} = 1$ in simple shear motion, up a $2000\sqrt{\frac{m\sigma^2}{\epsilon}}$ for $\dot{\varepsilon} = 0.2$ and $N_{\mathrm{pol}} = 20$ in planar extensional motion.

At each time, the average stress given as output by LAMMPS is projected onto the basis tensors through the formulae (5.3) and these projections are averaged over time. Finally, a mean over all initial configurations is taken. Figure 5.1 presents the data obtained for the generalized viscosity η and the reorientation factor λ_3. By fitting those data with Carreau and power functions we obtain, for the monomeric case with $N_{\mathrm{pol}} = 1$, the curves

$$\lambda_{3,\mathrm{ext}}(\dot{\varepsilon}) = 0, \qquad \eta_{\mathrm{ext}}(\dot{\varepsilon}) = 1.7/\left[1 + (0.108\,\dot{\varepsilon})^{1.05}\right]^{2.276},$$
$$\lambda_{3,\mathrm{sh}}(\dot{\varepsilon}) = 0.0706\,\dot{\varepsilon}^{1.2}, \qquad \eta_{\mathrm{sh}}(\dot{\varepsilon}) = \frac{1.806}{\left[1 + (1.6\,\dot{\varepsilon})^{1.65}\right]^{0.191}} + \frac{1.7 - 1.806}{\left[1 + (0.3\,\dot{\varepsilon})^{0.53}\right]^{22}}.$$

For the polymeric case with $N_{\mathrm{pol}} = 20$, the Gaussian Process Regression method was used to

obtain the fitting curves, see next SubSection 5.3.

By comparing the results obtained under simple shear and planar extension for $N_{\mathrm{pol}} = 1$ and $N_{\mathrm{pol}} = 20$, we find that the former fluid displays almost no rate dependence and very little flow-type dependence of the stress coefficients, while the latter features rate dependence and a strong flow-type dependence (Figure 5.1). The statistics of interaction between monomers in the two types of flow does not differ significantly, leading to a quasi-Newtonian rheology. On the contrary, the fact that polymer chains are kept in an elongated state by extensional flows, while they tend to tumble and keep a spherical shape in simple shear, generates a richer phenomenology. In fact, the shear-thinning trend displayed in simple shear is qualitatively similar to that of monomeric fluids, while we find an opposite trend—a shear-thickening behavior—in extensional flows at small deformation rates, followed by a non-monotonic behavior of the viscosity. The elastic effects generated by the bonds are crucial in this case and give rise, in simple shear, to the normal stress differences associated with the coefficient λ_3, also featuring a non-monotonic curve.

The statistical uncertainty observed at low strain rates is due to the definition of these functions η and λ_3 in our framework, see Eq. (5.3). The error bar on the stress is constant but when we divide by $\dot{\varepsilon}$ the error is amplified by $1/\dot{\varepsilon}$.

Furthermore, it would appear that the statistical uncertainty at low strain rates is much greater in the monomeric case than in the polymeric one. But this is due to the fact that higher viscosity values feel less the influence of fluctuations. They have similar fluctuations but on the viscosity scale of polymers they are less visible.

The direct connection between the statistics of chain conformation in the polymeric case and the observed rheology can be evinced from the probability distribution, presented in Figure 5.2, of the normalized radius of gyration R_g and asphericity α defined as follows. Let the components of the 3×3 gyration tensor be

$$\mathbf{R}_{\mu\nu} \equiv \frac{1}{M} \sum_{i=1}^{20} m_i (\boldsymbol{r}_i - \boldsymbol{r}_{\mathrm{cm}})_\mu (\boldsymbol{r}_i - \boldsymbol{r}_{\mathrm{cm}})_\nu,$$

with m_i the mass of the i-th monomer, $\boldsymbol{r}_i$ its position, $M = \sum_i m_i$, and $\boldsymbol{r}_{\mathrm{cm}}$ the center of mass of the polymeric chain. With R_0 the effective monomer radius, we set

$$R_g^2 \equiv \frac{1}{R_0^2 M} \sum_i m_i |\boldsymbol{r}_i - \boldsymbol{r}_{\mathrm{cm}}|^2 = \frac{\mathrm{tr}\,\mathbf{R}}{R_0^2}.$$

Moreover, the asphericity is given by

$$\alpha \equiv \frac{1}{R_0^2} \left[a_3 - \frac{1}{2}(a_1 + a_2) \right],$$

where $a_1 \leq a_2 \leq a_3$ are the eigenvalues of the gyration tensor $\mathbf{R}$.

At low deformation rate, the distributions obtained in simple shear and extensional flows are almost identical (blue curves in Figure 5.2) because the chains are equally and mildly stretched

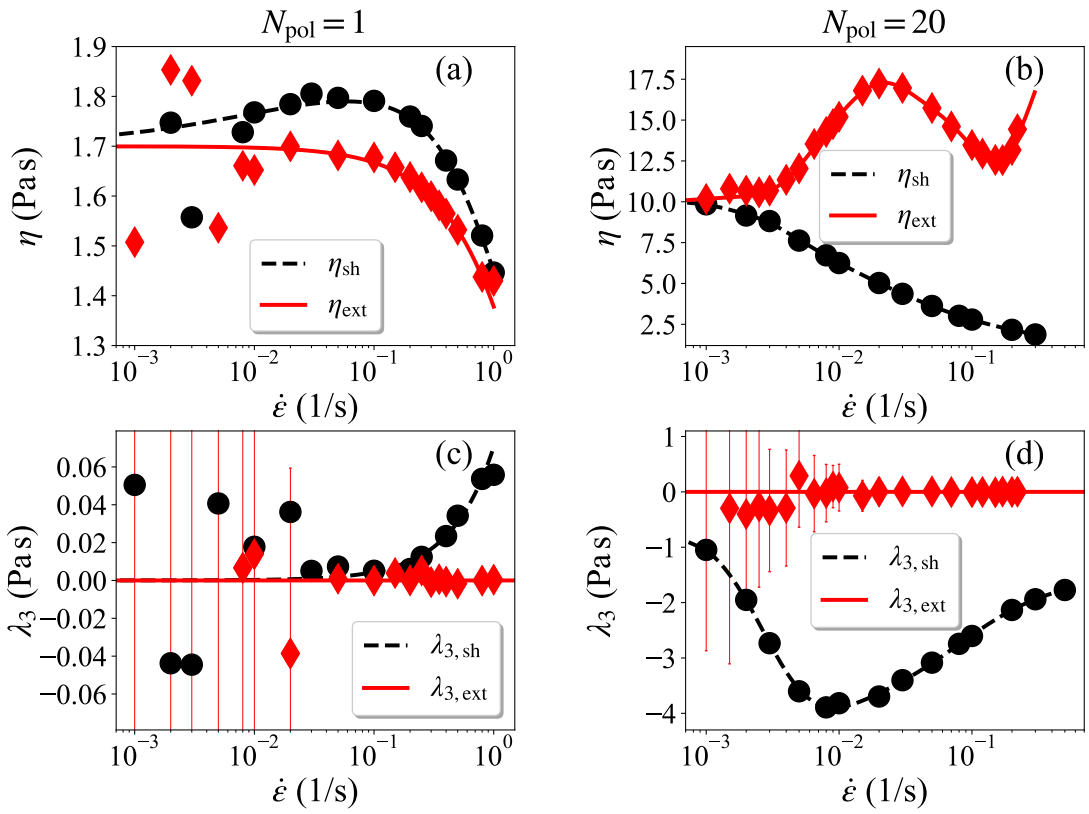

Figure 5.1: *The monomeric fluid displays almost no rate dependence and very little flow-type dependence of the stress coefficients, while the polymeric fluid features rate dependence and a strong flow-type dependence.* We compare the NEMD data for the stress coefficients η (top) and λ_3 (bottom) against $\dot{\varepsilon}$ obtained for the monomeric case with $N_{\mathrm{pol}} = 1$ (left) and the polymeric case $N_{\mathrm{pol}} = 20$ (right) under simple shear (circles and black dashed curves) and planar extension (diamonds and red solid curves). In the latter case, λ_3 fluctuates around zero, that is the expected value based on symmetry considerations. The presence of a strong flow-type dependence for the polymeric fluid is a key feature, originated by the different conformations of the long molecules. Fitting curves are obtained as described in the text.

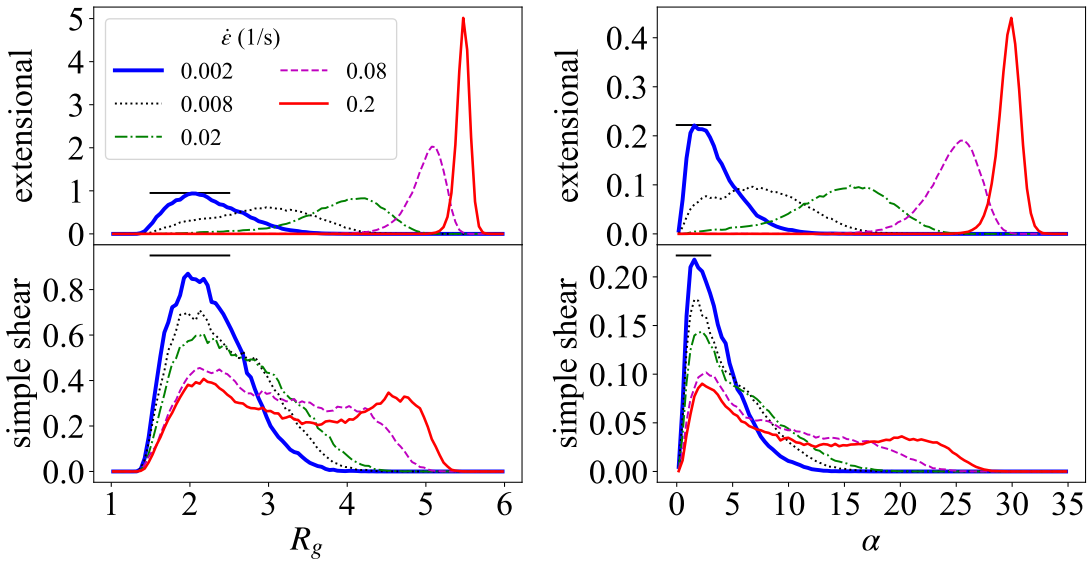

Figure 5.2: *The presence of a strong flow-type dependence for the polymeric fluid is a key feature, originated by the different conformations of the long molecules.* The probability distribution of radius R_g of gyration (divided by the effective monomer radius) and asphericity α for the polymeric chains under simple shear and extensional flow is reported for different values of $\dot{\varepsilon}$. The black bars indicate equal values for an easier comparison between the results under simple shear and planar extension. The curves are generated considering conformational data of five chains over 20,000 time steps of steady-state NEMD.

by the imposed flow. As $\dot{\varepsilon}$ grows larger, the extensional flow distributions feature a single peak that is progressively shifted rightward, toward more stretched configurations. On the other hand, in simple shear we notice a broadening of the distribution eventually leading to a doubly peaked shape (red curves in Figure 5.2). This indicates that chains spend roughly half of the time in a stretched configuration while frequently going back to a coiled configuration. In this very different microscopic behavior we find the origin of the strong flow-type dependence of the viscosity at larger $\dot{\varepsilon}$.

5.3 Fitting procedure for the micro-scale NEMD data

We report here the details about the fitting of micro-scale data that we performed using Gaussian Process Regression (GPR). Since some choices are involved in the procedure, it seems appropriate to give a brief account of ours. To do the fitting, we referred mainly to Neumann [49] that presents `pyGPs`, a Python software library implementing Gaussian processes (GPs) for Machine Learning (ML). The library provides a wide range of functionalities reaching from simple gp specification via mean and covariance and gp inference to more complex implementations of hyperparameter optimization, sparse approximations, and graph based learning. Then, we took

also some hints from [64], which is one of the main basic text for Gaussian Process in the context of ML.

GPR is a Bayesian approach to regression based on machine learning techniques. The fitting is done through a Gaussian stochastic process $f(x;\mathbf{w})$ that evolves along the variable x and depends on a list of hyper-parameters $\mathbf{w}$. The observed data are a finite number N of pairs $(x_i, y_i)_{i=1}^N$. The functional form of the Gaussian process is specified by its mean and covariance functions, $m(x;\mathbf{w}) = \mathbb{E}[f(x;\mathbf{w})]$ and $K(x,x';\mathbf{w}) = \mathbb{E}\big[(f(x;\mathbf{w}) - m(x;\mathbf{w}))\,(f(x';\mathbf{w}) - m(x';\mathbf{w}))\big]$, where $\mathbb{E}$ denotes the expected value. A fundamental feature of GPR is that it does not produce a definite value of the fitting parameters $\mathbf{w}$, but considers them random variables and seeks to determine suitable mean and variance for their distribution. This is achieved by an iterative optimization that takes into account the likelihood of the parameters distributions given the knowledge of the observed data [63].

What one needs to specify is the type of mean and covariance functions to be used for the GPR. Typical choices for the former are polynomial functions of x with coefficients given by $\mathbf{w}$, while for the latter are Radial Basis Functions

$$K_{\mathrm{RBF}}(x,x';\sigma,l) \equiv \sigma^2 \exp\left(-\frac{|x-x'|^2}{2l^2}\right)$$

with a set of two hyper-parameters $\mathbf{w} = (\sigma, l)$, or the Matérn covariance of degree ν given by

$$K_{\mathrm{M},\nu}(x,x';\sigma,\varrho) \equiv \sigma^2 \frac{2^{1-\nu}}{\Gamma(\nu)} \left(\sqrt{2\nu}\frac{|x-x'|}{\varrho}\right)^{\nu} K_\nu \left(\sqrt{2\nu}\frac{|x-x'|}{\varrho}\right),$$

where Γ is the Euler gamma function and K_ν is the modified Bessel function of the second kind. In our treatment, we took as x variable the quantity $\dot{\varepsilon}$ or $\log_{10}(\dot{\varepsilon})$, as y variable we took η, $\log_{10}(\eta)$, or λ_3. We tested regressions with mean function zero, constant, or polynomial up to degree four and, for the covariance function, RBF or Matérn kernel of degree up to 5 and pick the combinations that give the best results after optimization.

5.3.1 Data-driven material functions

Ideally, we would like to perform micro-scale simulations with many values of $\dot{\varepsilon}$ and β_3, since flows in generic geometries can easily feature variations of the flow type with β_3 ranging from minus to plus infinity and values of $\dot{\varepsilon}$ that cover many orders of magnitude. The implementation of simulation algorithms for mixed flows different from simple shear and planar extension is a nontrivial task that will be addressed in future works, but we still need, for our macro-scale simulations, a suitable definition of material functions that covers the whole range of kinematic parameters. We thus apply simple extrapolation strategies to build material functions out of the available computational data.

Specifically, we extend the fitted curves $\eta_{\mathrm{sh}}(\dot{\varepsilon})$, $\eta_{\mathrm{ext}}(\dot{\varepsilon})$, $\lambda_{3,\mathrm{sh}}(\dot{\varepsilon})$ and $\lambda_{3,\mathrm{ext}}(\dot{\varepsilon})$ out of their

natural domains by taking constant values. Then we set

$$\tilde{\eta}(\dot{\varepsilon}, \beta_3) \equiv \begin{cases} (1 - |\beta_3|)\eta_{\text{ext}}(\dot{\varepsilon}) + |\beta_3|\eta_{\text{sh}}(\dot{\varepsilon}), & \beta_3 \in [-1, 1] \\ \eta_{\text{sh}}(\dot{\varepsilon}), & |\beta_3| > 1 \end{cases} \tag{5.5}$$

that is an even function of β_3 with $\eta_{\text{ext}}(\dot{\varepsilon}) = \tilde{\eta}(\dot{\varepsilon}, 0)$ and $\eta_{\text{sh}}(\dot{\varepsilon}) = \tilde{\eta}(\dot{\varepsilon}, 1)$, and

$$\tilde{\lambda}_3(\dot{\varepsilon}, \beta_3) \equiv \begin{cases} \beta_3 \lambda_{3,\text{sh}}(\dot{\varepsilon}), & \beta_3 \in [-1, 1] \\ \pm\, \lambda_{3,\text{sh}}(\dot{\varepsilon}), & \beta_3 \gtrless \pm 1 \end{cases} \tag{5.6}$$

that is an odd function of β_3 and such that $\lambda_{3,\text{ext}}(\dot{\varepsilon}) = \tilde{\lambda}_3(\dot{\varepsilon}, 0) \approx 0$ and $\lambda_{3,\text{sh}}(\dot{\varepsilon}) = \tilde{\lambda}_3(\dot{\varepsilon}, 1)$. These operations in combination with (5.4) allow us to build a complete set of data for the stress tensor as a function of $\dot{\varepsilon}$ and β_3.

5.4 Macro-scale simulation

We consider the flow of an incompressible fluid with constant density ρ and velocity vector $\boldsymbol{u}$. As we have discussed in Chapter 1, from the macroscopic point of view the continuum description leads to the conservation of mass and the balance of linear momentum. In the incompressible case, they translate into the following partial differential equations on the domain Ω:

$$\nabla \cdot \boldsymbol{u} = 0, \tag{5.7}$$

$$\rho \left(\frac{\partial \boldsymbol{u}}{\partial t} + (\boldsymbol{u} \cdot \nabla)\, \boldsymbol{u} \right) = \nabla \cdot \boldsymbol{\sigma}(\boldsymbol{u}, p). \tag{5.8}$$

Here $\boldsymbol{\sigma}$ denotes the Cauchy stress tensor and p the pressure field. Equation (5.7) expresses the incompressibility constraint. We partition the boundary of the domain as disjoint union of inlet Γ_{in}, outlet Γ_{out}, and solid walls Γ_{w}, so that $\partial\Omega = \Gamma_{\text{in}} \cup \Gamma_{\text{out}} \cup \Gamma_{\text{w}}$. As usual, $\boldsymbol{n}$ is the outward unit normal to $\partial\Omega$.

A weak formulation of the problem is retrieved by multiplying equation (5.8) by a test function $\boldsymbol{v} \in H^1_{\Gamma_{\text{w}}}(\Omega) = \{\boldsymbol{f} \in H^1(\Omega) : \boldsymbol{f}|_{\Gamma_{\text{w}}} = \boldsymbol{0}\}$ and integrating over Ω. By applying Green's formula, we obtain the integral equation

$$\int_\Omega \rho \frac{\partial \boldsymbol{u}}{\partial t} \cdot \boldsymbol{v} + \int_\Omega \rho(\boldsymbol{u} \cdot \nabla)\boldsymbol{u} \cdot \boldsymbol{v} = \int_{\partial\Omega} \boldsymbol{\sigma}\boldsymbol{n} \cdot \boldsymbol{v} - \int_\Omega \boldsymbol{\sigma} : \nabla \boldsymbol{v}. \tag{5.9}$$

Moreover, (5.7) can be multiplied by a scalar test function $q \in L^2_0(\Omega) = \{g \in L^2_0(\Omega) : \int_\Omega g = 0\}$ and integrated over Ω to give

$$\int_\Omega q \nabla \cdot \boldsymbol{u} = 0. \tag{5.10}$$

We decompose the Cauchy stress tensor in spherical and deviatoric parts by introducing the traceless extra stress $\boldsymbol{\tau}$ such that $\boldsymbol{\sigma} = -(p + \bar{p})\mathbf{I} + \boldsymbol{\tau}$, where $\bar{p} \in L^2_0(\Omega)$ is a given pressure field used to impose a chosen pressure gradient from inlet to outlet. On top of the Dirichlet

boundary conditions for $\boldsymbol{u}$ on Γ_{w} we assume a form of periodicity for $\boldsymbol{u}$ and p, requiring that they take the same values on Γ_{in} and Γ_{out}. Thanks to the independence of the test functions $\boldsymbol{v}$ and q, we can take the sum of (5.9) and (5.10) and substitute the expression for $\boldsymbol{\sigma}$ to obtain the complete weak formulation of the problem:

Find $\boldsymbol{u} \in L^2(\mathbb{R}^+; H^1_{\Gamma_{\mathrm{w}}}(\Omega))$ *and* $p \in L^2(\mathbb{R}^+; L^2_0(\Omega))$, *such that for any suitable test functions* $\boldsymbol{v}$ *and* q *we have*

$$\int_\Omega \rho \frac{\partial \boldsymbol{u}}{\partial t} \cdot \boldsymbol{v} + \int_\Omega \rho(\boldsymbol{u} \cdot \nabla)\boldsymbol{u} \cdot \boldsymbol{v} + \int_\Omega \boldsymbol{\tau} : \nabla \boldsymbol{v} + \int_\Omega q \nabla \cdot \boldsymbol{u} - \int_\Omega (p + \bar{p}) \nabla \cdot \boldsymbol{v} = \int_{\Gamma_{\mathrm{in}} \cup \Gamma_{\mathrm{out}}} \bar{p} \boldsymbol{n} \cdot \boldsymbol{v}. \quad (5.11)$$

Equation (5.11) must be completed with suitable initial conditions for the velocity field, that we will assume to vanish identically at time $t = 0$. To exploit the reflection symmetry of some domains, we will consider a fictitious boundary Γ_{c} corresponding to the symmetry axis. On this boundary we will assume that the normal component of the velocity field and the tangential component of the traction $\boldsymbol{\tau}\boldsymbol{n}$ vanish.

For the time integration of (5.11) we apply a semi-implicit Euler scheme. In particular, the nonlinear convective term is approximated explicitly, the rest is approximated implicitly. This approximation is suitable to simulate flows at sufficiently low Reynolds number. Consequently, we have

$$\int_\Omega \rho \frac{\boldsymbol{u}^{n+1}}{\Delta t} \cdot \boldsymbol{v} + a(\boldsymbol{u}^{n+1}, \boldsymbol{v}) + b(\boldsymbol{v}, p^{n+1} + \bar{p}) - b(\boldsymbol{u}^{n+1}, q) = \int_\Omega \rho \frac{\boldsymbol{u}^n}{\Delta t} \cdot \boldsymbol{v} - \int_\Omega \rho(\boldsymbol{u}^n \cdot \nabla)\boldsymbol{u}^n \cdot \boldsymbol{v} + \int_{\Gamma_{\mathrm{in}} \cup \Gamma_{\mathrm{out}}} \bar{p} \boldsymbol{n} \cdot \boldsymbol{v} \quad (5.12)$$

with bilinear forms $b(\boldsymbol{u}, q) := -\int_\Omega q \nabla \cdot \boldsymbol{u}$ and $a(\boldsymbol{u}, \boldsymbol{v}) := \int_\Omega \boldsymbol{\tau}(\boldsymbol{u}) : \nabla \boldsymbol{v}$. Note that the latter is already linearized since the (nonlinear) material functions in (5.4) are computed using $\boldsymbol{u}^n$.

For each time step, Equation (5.12) is discretized in space and solved, in a standard way, by means of mixed finite elements P_2-P_0 for the approximation of the velocity-pressure pair, which are known to satisfy the Ladyzhenskaya–Babuška–Brezzi inf-sup condition for a stable solution of the associated saddle-point problem [6]. The numerical method is implemented within the Python library FEniCS [46] and some details pertaining the micro-to-macro coupling through the dynamic reconstruction of the extra stress are given in next section 5.5.

5.5 Multi-scale coupling in the code

The purpose of this section is to present the portion of code that implements the multi-scale coupling in the context of an otherwise standard Finite Element simulation of the flow equations, see [41] for an introduction to FEniCS, the Python library we used. The peculiarity of our method concerns the integration of NEMD data with the continuum solver and the construction of the stress tensor based on the general representation (5.4).

In our code, `numpy` arrays contain the interpolated curves η_{sh}, $\lambda_{3,\mathrm{sh}}$ and η_{ext}, while $\lambda_{3,\mathrm{ext}}$ is simply zero. In particular, the first column of the array `S` contains the values of $\dot{\varepsilon}$ on which the Carreau function or GPR is sampled and the second column the corresponding expected

values of η_{sh}. For an efficient use of those data in the stress computation, we transform them in projections on a Finite Element space defined on a one-dimensional mesh, the nodes of which are given by the sampled values of $\dot{\varepsilon}$. Considering, for instance, the curve η_{sh}, it becomes the function `etas` in the space `E` of P_1 elements defined on the mesh `mesh_etas`. Its construction is performed with the following lines of code. Similar commands are used to define the functions `etae` and `lambda3s` that represent η_{ext} and $\lambda_{3,\mathrm{sh}}$.

```
# 1D mesh for eta_sh

import numpy as np
from mshr import *

nodes = S[:,0]
n_nodes = nodes.shape[0]
n_cells = n_nodes - 1
cells = np.arange(n_cells)

# The geometry is inherited by a standard mesh
mesh0 = UnitIntervalMesh(n_cells)
gdim = mesh0.geometry().dim()
tdim = mesh0.topology().dim()
c_type = mesh0.type()
c_str = CellType.type2string(c_type.cell_type())

# Mesh nodes are specified from data
mesh_etas = Mesh()
editor = MeshEditor()
editor.open(mesh_etas, c_str, tdim, gdim)
editor.init_vertices(n_nodes)
editor.init_cells(n_cells)
[editor.add_vertex(int(i),[n]) for i,n in enumerate(nodes)]
[editor.add_cell(i,[i,i+1]) for i in range(cells.shape[0])]
editor.close()

# Definition of FE space and function
E = FunctionSpace(mesh_etas, 'P', 1)
etas= Function(E)
etas.vector().set_local(np.flip(S[:,1], axis=0))
etas.set_allow_extrapolation(True)
```

The second portion of code relevant to the multi-scale coupling is the local computation of the kinematic parameters $\dot{\varepsilon}$ and β_3 and the reconstruction, at each time step, of the spatial profile of the stress coefficients η and λ_3 by means of the material functions $\tilde{\eta}(\dot{\varepsilon}, \beta_3)$ and $\tilde{\lambda}_3(\dot{\varepsilon}, \beta_3)$. This is accomplished through the following definitions, where `mesh` is the two-dimensional triangular mesh defined on the flow domain, and `u` is the velocity and pressure fields, respectively.

```
from fenics import *

def Max(a, b):
    return (a+b+abs(a-b))/Constant(2)

def Min(a, b):
    return (a+b-abs(a-b))/Constant(2)

# Epsilondot from the velocity u_n
def eps(u_n):
    return sqrt(0.5*((u_n[0].dx(0))**2 + (u_n[1].dx(1))**2) + 0.25*(u_n
    [1].dx(0) + u_n[0].dx(1))**2)

# Epsilondot truncated for viscosity in shear
def eps_es(u):
    a = nodes[0]
    b = nodes[-1]
    ux, uy, p = split(u)
    return Max(a,Min(b, eps(u)))

# Epsilondot truncated for viscosity in extension
def eps_ee(u):
    a = nodes_e[0]
    b = nodes_e[-1]
    ux, uy, p = split(u)
    return Max(a,Min(b, eps(u)))

# Epsilondot truncated for lambda_3 in shear
def eps_ls(u):
    a = nodes_l[0]
    b = nodes_l[-1]
    ux, uy, p = split(u)
    return Max(a,Min(b, eps(u)))

# Beta3 from the velocity u_n truncated between -1 and 1
def beta(u_n):
    ux = u_n[0]
    uy = u_n[1]
    uxy= ux.dx(1)
    uyx= uy.dx(0)
    rot= uyx - uxy
    return Max(-1, Min(1, rot/(2*Max(1.e-12, eps(u_n)))))

# Initialize functions
Q = FunctionSpace(mesh, 'P', 1)
```

```
epsilondot_ = Function(Q)
beta3_ = Function(Q)
eta = Function(Q)
lambda3 = Function(Q)
```

At each time step, we need to compute the new stress coefficients based on the velocity field `u_n` obtained in the previous step. These will be used to update the stress. To this end, we apply the interpolation between simple shear and extensional data according to (5.5)–(5.6).

```
# Within the time evolution loop
    # Update kinematic parameters
    edot_es= project(eps_es(u_n), Q).vector().get_local()
    edot_ee= project(eps_ee(u_n), Q).vector().get_local()
    edot_ls= project(eps_ls(u_n), Q).vector().get_local()
    beta3= project(beta(u_n), Q).vector().get_local()
    # Evaluate material functions
    etas_temp= np.zeros(edot_es.shape[0])
    etae_temp= np.zeros(edot_ee.shape[0])
    eta_temp= np.zeros(edot_es.shape[0])
    lambda3_temp= np.zeros(edot_ls.shape[0])
    for i in range(edot_es.shape[0]):
        etas_temp[i]= etas(edot_es[i])
        etae_temp[i]= etae(edot_ee[i])
        lambda3_temp[i]= lambda3s(edot_ls[i])
    eta_temp= np.absolute(beta3)*etas_temp + (1-np.absolute(beta3))*
   etae_temp
    lambda3_temp= beta3*lambda3_temp
    # Casting the data into functions on the 2D mesh
    eta.vector().set_local(eta_temp)
    lambda3.vector().set_local(lambda3_temp)

#Reconstruction of stress tensor through functions eta and lambda3
def sigma(u, p, u_n, eta, lambda3):
    return 2*eta*epsilon(u) -p*Identity(len(u)) + 2*lambda3*g3(u, A)
```

5.6 Numerical results for different geometries

The aim of this section is to demonstrate the robustness and effectiveness of our heterogeneous multi-scale method by presenting the results of simulations in three different planar geometries: flows in a straight channel, through a 4:1 contraction, and past a deep hole. These are paradigmatic geometries frequently used to test the non-Newtonian behavior of fluid models [9].

5.6.1 Channel flow

The multi-scale method is firstly tested on the classical case of a planar channel flow. The total length of the channel is $L = 5\,\mathrm{m}$ along the x-axis and the system width is $W = 2\,\mathrm{m}$ along the y-axis. Exploiting the reflection symmetry of the problem, we discretized only the upper half of the channel on a mesh with 100 triangular elements along the x-axis and 20 elements along the y-axis, for a total of 4000 triangles in the entire computational domain. On the fictitious boundary that corresponds to the center of the channel we impose a vanishing vertical velocity and a vanishing normal traction to respect the reflection symmetry of the problem. We consider a fluid with unit density and drive the flow by imposing a constant horizontal pressure gradient $C = 1\,\mathrm{Pa/m}$. As for the velocity field $\boldsymbol{u}$, we assume periodic boundary conditions so that the velocity at inlet and outlet is the same. The time step is $\Delta t = 1 \times 10^{-3}\,\mathrm{s}$. We let the system evolve up to the time $T = 2\,\mathrm{s}$ to reach a steady state.

The flow type is everywhere equivalent to that of a simple shear. Indeed, this is a viscometric flow with $\beta_3 = 1$ in the top half of the domain and $\beta_3 = -1$ in the other half. A discontinuity would appear at the midline of the channel consistent with the fact that β_3 is not defined for $\dot{\varepsilon} = 0$. The homogeneity of the flow type makes the flow-type dependence of the stress tensor irrelevant. To assess the relevance of non-Newtonian effects, we compare the solution obtained from the multi-scale approach with the analytical solution of a reference Newtonian model, represented by the classical stress-strain relation

$$\boldsymbol{\sigma} = -p\mathbf{I} + 2\bar{\eta}\mathbf{D} \tag{5.13}$$

with $\bar{\eta}$ constant. We take $\bar{\eta} = 1.7\,\mathrm{Pa\,s}$ for $N_{\mathrm{pol}} = 1$ and $\bar{\eta} = 10\,\mathrm{Pa\,s}$ for $N_{\mathrm{pol}} = 20$, corresponding to the zero-rate limit of the interpolated shear viscosity from our NEMD simulations.

The comparison of velocity, deformation rate, and viscosity profiles is reported in Figure 5.3. In the case $N_{\mathrm{pol}} = 1$ the non-Newtonian solution is extremely close to the Newtonian one, as expected from the mild rate dependence of the viscosity and the small values of λ_3. In the case $N_{\mathrm{pol}} = 20$, we observe a much larger deviation that is small only around the center of the channel, where the shear rate vanishes and the viscosity approaches that of the reference Newtonian model. The validation of the values of the viscosity curves in simple shear was done by observing the range of values obtained in the study presented by Stalter *et al.* [56].

Due to the non-uniformity of the viscosity in the development of the flow and in its steady state, the characterization of the flow by means of dimensionless quantities such as the Reynolds number is not straightforward. Nevertheless, we can identify the range of local parameter values as follows. We take the channel width W as reference length and $P = CW$ as reference pressure drop. The local Reynolds number is then given by

$$\mathrm{Re} = \frac{W\sqrt{\rho CW}}{\eta}.$$

Another important dimensionless quantity is the reorientation angle φ, such that

$$\tan\varphi = \frac{\lambda_3}{\eta + \sqrt{\eta^2 + \lambda_3^2}},$$

which we have already discussed in Chapter 2 and whose geometric information is precisely the meaning of the first normal stress difference in simple shear flows, extended to generic local flows by the definition of λ_3 and η, see [25].

In the monomeric case, we have $\eta_{\min} = 1.6\,\mathrm{Pa\,s}$ and $\eta_{\max} = 1.8\,\mathrm{Pa\,s}$ so that $\mathrm{Re} \in [1.57, 1.77]$, while φ is negligible. In the polymeric case, we have $\eta_{\min} = 2\,\mathrm{Pa\,s}$ and $\eta_{\max} = 10\,\mathrm{Pa\,s}$ so that $\mathrm{Re} \in [0.28, 1.41]$. We can then consider our examples to be at low Reynolds number. Since $\dot{\varepsilon}_{\max} = 0.24\,\mathrm{s}^{-1}$, we have $\varphi \in [-22, 22]$ degrees, that includes quite significant values.

5.6.2 Flow through a contraction

As a first example of flow in a complex geometry we consider the 4:1 contraction. This flow is characterized by the presence of different local flow types: simple shear in regions that are sufficiently far from the ends of the contraction, extensional and mixed motion in proximity of entrance and exit of the contraction, and mixed rotational flow near the corners of the domain. The spatial non-uniformity of the flow type must be taken into account to obtain a precise macro-scale description of the fluid motion. To show this, we compare the prediction of the full non-Newtonian model with that of a *modified* non-Newtonian model, wherein the flow-type dependence is artificially suppressed. Specifically, β_3 is replaced by the function $\mathrm{sign}(\beta_3)$. In this way, only the micro-scale data obtained in simple shear (i.e., $\beta_3 = \pm 1$) are used, but the results cannot properly reflect the fluid behavior.

We discuss results obtained with a channel of length $L = 5\,\mathrm{m}$ and maximum width $W = 2\,\mathrm{m}$, only in the polymeric case $N_{\mathrm{pol}} = 20$, with time step $\Delta t = 10^{-3}$, letting the system evolve to reach a steady state for $T = 0.2\,\mathrm{s}$. We can appreciate the time convergence to the steady solution by looking at the evolution of the flow rate Q through vertical sections of the domain, reported in Figure 5.4, left panel. The discretization employs an unstructured triangular mesh with average diameter of the triangles $h \approx 0.03\,\mathrm{m}$. The mesh convergence of the multi-scale method is assessed by considering the L^2 norm of the difference between solutions obtained with mesh parameter h and $2h$. From the data reported in Figure 5.4, right panel, we see that the incremental correction scales linearly in h, thus showing convergence of our simulation.

The pressure gradient that drives the flow is $C = 0.3\,\mathrm{Pa/m}$. The velocity field $\boldsymbol{u}$ is assumed periodic so that it is matched at inlet and outlet and, to exploit symmetry and compute the numerical solution only in the upper half of the domain, we use the same conditions as in the straight channel simulation, namely, vanishing vertical velocity and vertical traction at the center of the channel. The flow is laminar with the characteristic increase of horizontal velocity u_x in correspondence of the contraction. The pressure gradient is concentrated along the narrower portion of the domain and features oblique isolines due to the presence of normal

stress differences in that region (Figure 5.5). The non-uniformity of the deformation rate $\dot{\varepsilon}$ and of the flow-type parameter β_3 have a strong influence on the local values of η, that ranges from 3.8 Pa s to 13 Pa s in the contracting region, and λ_3, that ranges from -4 Pa s to 4 Pa s, considering also the lower half of the domain (see Figure 5.6). From these values and taking now $W/4$ as reference length, we can estimate $\mathrm{Re} \in [0.015, 0.05]$ and $\varphi \in [-23.5, 23.5]$ degrees.

In this complex flow, the flow type measured by the parameter β_3 varies significantly through the domain (Figure 5.6b), ranging from pure extension ($\beta_3 = 0$) to simple shear ($|\beta_3| = 1$) to more rotational flows ($|\beta_3| > 1$). Regions of mixed and extensional motion cover a major part of the domain, going well within the contraction. Since the viscosity in the full non-Newtonian model is a function of $\dot{\varepsilon}$ and β_3, the effect of the flow type is clearly dominant in determining its value. The importance of correctly embedding the flow-type dependence in the multi-scale model can be highlighted by comparing the prediction of the full non-Newtonian model with that obtained from the modified non-Newtonian model (Figure 5.7). The viscosity in the modified model presents a very different profile in the extensional and mixed flow regions, where it happens to decrease instead of increasing, as predicted by the correct method and in line with the extensional rheology of the polymeric case. This has an immediate effect on the velocity profile, that features a more rapid flow and a clear asymmetry, due to the overemphasized role of the normal stress differences related to λ_3 in the modified model.

5.6.3 Flow past a deep hole

In this section we analyze a second example of flow in a complex geometry. We consider a channel of length $L = 5$ m and width $W = 1$ m. At a distance of 1.75 m from the inlet we find the hole of width $W_{\mathrm{hole}} = 1.5$ m and depth $H = 5$ m. The deep hole has to be built to certain proportions and we have taken our inspiration from what is described in Cochrane [7]. The discretization employs an unstructured triangular mesh with average diameter of the triangles $h \approx 0.06$ m. The time step is $\Delta t = 10^{-3}$ and we let the system evolve to reach a steady state for $T = 0.4$ s (see Figure 5.4, left panel). We present simulation results for the polymeric case $N_{\mathrm{pol}} = 20$, driving the flow with an outlet-to-inlet pressure gradient $C = 0.3$ Pa/m. The velocity field is again assumed to be periodic, and hence equal at inlet an outlet.

The flow past a deep hole features a complex distribution of local flow types with a consequent variation of the material response. Also in this case, a comparison of the viscosity and the horizontal velocity obtained with the full and the modified non-Newtonian models (Figure 5.8) confirms the need for a correct treatment of flow-type-dependent rheologies. The viscosity appears to be significantly different right above the deep hole. This has a mild but noticeable influence on the flow. The velocity depression is shifted rightward and, since the viscosity is lower, the flow is globally faster with the modified model, as seen also from the values of the flow rate reported in Figure 5.4.

From the component u_y of the velocity (Figure 5.9a) we can clearly see the region where the deep hole modifies the flow in the upper channel. Moreover, the presence of a clockwise-

rotating vortex can be inferred at the center of the shown portion of the hole. The deformation rate $\dot{\varepsilon}$ and the flow-type parameter β_3 highlight the presence of mixed flows and high-vorticity regions (Figure 5.9b and 5.9c). Specifically, β_3 confirms the presence of a vortex in the hole. The sharp contrast between yellow and green regions nearby the openings of the upper channel indicates the viscometric nature of the flow far from the hole. The values of λ_3 across the domain (Figure 5.9d) are a direct consequence of the non-Newtonian rheology and the complexity of the flow. The same applies to the viscosity shown in Figure 5.7c. For this flow, the relevant ranges of dimensionless parameters are $\mathrm{Re} \in [0.05, 0.12]$ and $\varphi \in [-20.8, 20.8]$ degrees. Hence, we have significant non-Newtonian effects while turbulent motions are prevented.

5.7 An analytical solution

This section stems from the need to solve a problem that arose when we simulated the flow of a non-Newtonian fluid in the straight channel: the isolines of the pressure, contrary to our expectations, were not vertical and created instabilities in the dynamics.

Finding the analytical solution of the motion in a channel for a special non-Newtonian model allowed us to highlight the origin of this problem and understand which boundary conditions were compatible with an admissible solution. In fact, imposing constant pressure at the boundary, as we did in a first attempt, turned out to be a wrong choice.

Moreover, not all discretization methods are able to capture this particularity of non-Newtonian fluids. Therefore, we had to abandon a less accurate pressure projection scheme in favor of a mixed finite elements approach, P_0 for pressure and P_2 for velocity.

Let us consider a Cartesian reference xOy and look for an analytical solution $(\boldsymbol{u}(x,y,t), p(x,y,t))$ to the flow of three types of fluid: Newtonian, quasi-Newtonian and non-Newtonian in a straight channel of height h and length L. The velocity gradient and the strain-rate tensor, written in components are

$$\nabla \boldsymbol{u} = \begin{bmatrix} \partial_x u_x & \partial_y u_x \\ \partial_x u_y & \partial_y u_y \end{bmatrix} \qquad \mathbf{D} = \frac{1}{2}\left(\nabla \boldsymbol{u} + \nabla \boldsymbol{u}^{\mathsf{T}}\right) = \frac{1}{2}\begin{bmatrix} 2\partial_x u_x & (\partial_x u_y + \partial_y u_x) \\ (\partial_x u_y + \partial_y u_x) & 2\partial_y u_y \end{bmatrix}$$

thus we compute the tensors

$$\mathbf{D}^2 = \frac{1}{4}\begin{bmatrix} 4(\partial_x u_x)^2 + (\partial_x u_y + \partial_y u_x)^2 & 2(\partial_x u_y + \partial_y u_x)(\partial_x u_x + \partial_y u_y) \\ 2(\partial_x u_y + \partial_y u_x)(\partial_x u_x + \partial_y u_y) & 4(\partial_y u_y)^2 + (\partial_x u_y + \partial_y u_x)^2 \end{bmatrix}$$

$$\operatorname{tr} \mathbf{D}^2 = \left((\partial_x u_x)^2 + (\partial_y u_y)^2\right) + \frac{1}{2}(\partial_x u_y + \partial_y u_x)^2$$

$$\mathbf{G}_3 = \frac{1}{2}(\mathbf{AD} - \mathbf{DA}) = \frac{1}{2}\begin{bmatrix} -(\partial_x u_y + \partial_y u_x) & (\partial_x u_x - \partial_y u_y) \\ (\partial_x u_x - \partial_y u_y) & (\partial_x u_y + \partial_y u_x) \end{bmatrix} \qquad \mathbf{A} = \begin{bmatrix} 0 & -1 \\ 1 & 0 \end{bmatrix}.$$

Let us consider the most generic case of a non-Newtonian fluid with both material functions

depending on both the strain rate $|\dot{\varepsilon}| = \sqrt{\frac{\text{tr}\,\mathbf{D}^2}{2}}$ and the flow parameter β_3

$$\eta = \eta(\dot{\varepsilon}, \beta_3) \qquad \lambda_3 = \lambda_3(\dot{\varepsilon}, \beta_3)$$

the stress tensor is given by

$$\boldsymbol{\sigma} = -p(x,y,t)\mathbf{I} + 2\eta(\dot{\varepsilon}, \beta_3)\mathbf{D} + 2\lambda_3(\dot{\varepsilon}, \beta_3)\mathbf{G}_3 = -p(x,y,t)\mathbf{I} + \boldsymbol{\tau}(\boldsymbol{u}(x,y,t))$$

and, written in components, has this expression

$$\boldsymbol{\sigma} = \begin{bmatrix} -p + 2\eta\partial_x u_x - \lambda_3(\partial_x u_y + \partial_y u_x) & \eta(\partial_x u_y + \partial_y u_x) + \lambda_3(\partial_x u_x - \partial_y u_y) \\ \eta(\partial_x u_y + \partial_y u_x) + \lambda_3(\partial_x u_x - \partial_y u_y) & -p + 2\eta\partial_y u_y + \lambda_3(\partial_x u_y + \partial_y u_x) \end{bmatrix}.$$

The stress tensor is inserted in the equation of motion

$$\rho\left(\frac{\partial \boldsymbol{u}}{\partial t} + (\boldsymbol{u}\cdot\nabla)\boldsymbol{u}\right) = -\nabla p + \nabla\cdot\boldsymbol{\tau}(\boldsymbol{u})$$

and since $(\boldsymbol{u}\cdot\nabla)\boldsymbol{u} = (u_x(\partial_x u_x) + u_y(\partial_y u_x), u_x(\partial_x u_y) + u_y(\partial_y u_y))$, the equation of motion projected onto the two dimensions becomes

$$\begin{cases} \rho\left(\dfrac{\partial u_x}{\partial t} + u_x(\partial_x u_x) + u_y(\partial_y u_x)\right) = -\partial_x p + \partial_x \tau_{xx} + \partial_y \tau_{xy} \\ \rho\left(\dfrac{\partial u_y}{\partial t} + u_x(\partial_x u_y) + u_y(\partial_y u_y)\right) = -\partial_y p + \partial_x \tau_{yx} + \partial_y \tau_{yy} \end{cases} \tag{5.14}$$

where the components of the extra-stress tensor are

$$\begin{aligned} \tau_{xx} &= 2\eta\partial_x u_x - \lambda_3(\partial_x u_y + \partial_y u_x) \\ \tau_{xy} &= \eta(\partial_x u_y + \partial_y u_x) + \lambda_3(\partial_x u_x - \partial_y u_y) \\ \tau_{yx} &= \eta(\partial_x u_y + \partial_y u_x) + \lambda_3(\partial_x u_x - \partial_y u_y) \\ \tau_{yy} &= 2\eta\partial_y u_y + \lambda_3(\partial_x u_y + \partial_y u_x). \end{aligned}$$

Thus, the equations take the following form

$$\begin{cases} \rho\left(\dfrac{\partial u_x}{\partial t} + u_x(\partial_x u_x) + u_y(\partial_y u_x)\right) = -\partial_x p + 2\eta\partial_{xx} u_x - \partial_x[\lambda_3(\partial_x u_y + \partial_y u_x)] + \eta(\partial_{yx} u_y + \partial_{yy} u_x) \\ \qquad\qquad + \partial_y[\lambda_3(\partial_x u_x - \partial_y u_y)] \\ \rho\left(\dfrac{\partial u_y}{\partial t} + u_x(\partial_x u_y) + u_y(\partial_y u_y)\right) = -\partial_y p + \eta(\partial_{xx} u_y + \partial_{xy} u_x) + \partial_x[\lambda_3(\partial_x u_x - \partial_y u_y)] + 2\eta\partial_{yy} u_y \\ \qquad\qquad + \partial_y[\lambda_3(\partial_x u_y + \partial_y u_x)]. \end{cases} \tag{5.15}$$

In the *straight channel*, instead, we have the additional assumptions that the vertical component of the velocity is null and that the horizontal velocity is nomore dependent from x because of

the continuity equation

$$\boldsymbol{u}(x,y,t) = u_x(x,y,t)\hat{\boldsymbol{x}} + u_y(x,y,t)\hat{\boldsymbol{y}} = u_x(x,y,t)\hat{\boldsymbol{x}} \qquad \text{i.e.} \quad u_y(x,y,t) = 0$$
$$\nabla \cdot \boldsymbol{u} = 0 \quad \rightarrow \partial_x u_x + \partial_y u_y = 0 \quad \rightarrow \partial_x u_x = -\partial_y u_y = 0 \quad \boldsymbol{u} = \boldsymbol{u}(y,t)$$

therefore, tensors and parameters of our flow become

$$\nabla \boldsymbol{u} = \begin{bmatrix} 0 & \partial_y u_x \\ 0 & 0 \end{bmatrix}, \qquad \boldsymbol{u} = \frac{1}{2}\begin{bmatrix} 0 & \partial_y u_x \\ \partial_y u_x & 0 \end{bmatrix}, \qquad \mathbf{G}_3 = \frac{1}{2}\begin{bmatrix} -\partial_y u_x & 0 \\ 0 & \partial_y u_x \end{bmatrix}$$
$$\mathbf{D}^2 = \frac{1}{4}\begin{bmatrix} (\partial_y u_x)^2 & 0 \\ 0 & (\partial_y u_x)^2 \end{bmatrix}, \qquad \operatorname{tr}\mathbf{D}^2 = \frac{1}{2}(\partial_y u_x)^2, \qquad |\dot{\varepsilon}| = \frac{\partial_y u_x}{2}$$

and since $(\boldsymbol{u}\cdot\nabla)\boldsymbol{u} = \boldsymbol{0}$ the equations reduce to

$$\begin{cases} \rho\dfrac{\partial u_x}{\partial t} = -\partial_x p - \partial_x(\lambda_3(\partial_y u_x)) + \eta(\partial_{yy} u_x) \\ 0 = -\partial_y p + \partial_y(\lambda_3(\partial_y u_x)). \end{cases} \tag{5.16}$$

Let us consider the Newtonian case

$$\eta = \overline{\eta}, \qquad \lambda_3 = 0$$

the equations of motion in the case of complex geometries

$$\begin{cases} \rho\left(\dfrac{\partial u_x}{\partial t} + u_x(\partial_x u_x) + u_y(\partial_y u_x)\right) = -\partial_x p + 2\overline{\eta}\partial_{xx} u_x + \overline{\eta}(\partial_{yx} u_y + \partial_{yy} u_x) \\ \rho\left(\dfrac{\partial u_y}{\partial t} + u_x(\partial_x u_y) + u_y(\partial_y u_y)\right) = -\partial_y p + \overline{\eta}(\partial_{xx} u_y + \partial_{xy} u_x) + 2\overline{\eta}\partial_{yy} u_y \end{cases} \tag{5.17}$$

while in the straight channel reduces to

$$\begin{cases} \rho\dfrac{\partial u_x}{\partial t} = -\partial_x p + \overline{\eta}(\partial_{yy} u_x) \\ 0 = \rho\dfrac{\partial u_y}{\partial t} = -\partial_y p. \end{cases} \tag{5.18}$$

thus $p = p(x,t)$ and making derivative in x of the first equation we obtain $-\partial_{xx} p = 0$, that means p linear in x, $p(x,t) = Cx + c(t)$. Adding the stationariety hypothesis $\partial_t u = \partial_t p = 0$ we obtain

$$\begin{cases} 0 = -C + \overline{\eta}\partial_{yy} u_x \\ p(x,y) = Cx + c \end{cases} \tag{5.19}$$

and from the first equation we have $u(y) = \frac{C}{2\overline{\eta}}\left(y^2 - 2c_1\right) + c_2$. Let us now impose the Dirichlet Boundary Conditions (DBCs) $u(0) = u(y) = 0$ obtaining $c_2 = 0$ e $c_1 = h/2$, therefore the

solution for the velocity is

$$u(y) = \frac{C}{2\overline{\eta}}(y^2 - hy)$$

while for the pressure it is sufficient to assign its value at inlet p_0 and the pressure drop C to obtain

$$p(x, y) = Cx + p_0.$$

Let us consider, finally, now the *quasi-Newtonian* case with λ_3 linear in $\dot{\varepsilon}$ and the constant viscosity

$$\eta = \overline{\eta} \qquad \lambda_3(\dot{\varepsilon}) = K\dot{\varepsilon}.$$

In complex geometries, where no symmetries are present, we have

$$\begin{cases} \rho\left(\dfrac{\partial u_x}{\partial t} + u_x(\partial_x u_x) + u_y(\partial_y u_x)\right) = -\partial_x p + 2\overline{\eta}\partial_{xx}u_x - K(\partial_x\dot{\varepsilon})(\partial_x u_y + \partial_y u_x) - K\dot{\varepsilon}(\partial_{xx}u_y + \partial_{xy}u_x) \\ \qquad\qquad + \overline{\eta}(\partial_{yx}u_y + \partial_{yy}u_x) + K(\partial_y\dot{\varepsilon})(\partial_x u_x - \partial_y u_y) + K\dot{\varepsilon}(\partial_{yx}u_x - \partial_{yy}u_y) \\ \rho\left(\dfrac{\partial u_y}{\partial t} + u_x(\partial_x u_y) + u_y(\partial_y u_y)\right) = -\partial_y p + \overline{\eta}(\partial_{xx}u_y + \partial_{xy}u_x) + K(\partial_x\dot{\varepsilon})(\partial_x u_x - \partial_y u_y) \\ \qquad\qquad + K\dot{\varepsilon}(\partial_{xx}u_x - \partial_{xy}u_y) + 2\overline{\eta}\partial_{yy}u_y \\ \qquad\qquad + K(\partial_y\dot{\varepsilon})(\partial_x u_y + \partial_y u_x) + K\dot{\varepsilon}(\partial_{yx}u_y + \partial_{yy}u_x) \end{cases} \tag{5.20}$$

where

$$|\dot{\varepsilon}| = \sqrt{\frac{\mathrm{tr}\,(\mathbf{D}^2)}{2}} = \sqrt{\frac{1}{2}\left((\partial_x u_x)^2 + (\partial_y u_y)^2\right) + \frac{1}{4}(\partial_x u_y + \partial_y u_x)^2}$$

$$\begin{aligned} \partial_x\dot{\varepsilon} &= \partial_x\left(\sqrt{\frac{1}{2}\left((\partial_x u_x)^2 + (\partial_y u_y)^2\right) + \frac{1}{4}(\partial_x u_y + \partial_y u_x)^2}\right) \\ &= \frac{1}{2}\left[\frac{1}{2}\left((\partial_x u_x)^2 + (\partial_y u_y)^2\right) + \frac{1}{4}(\partial_x u_y + \partial_y u_x)^2\right] * \\ &\quad * \left[\frac{1}{2}\left(2(\partial_x u_x)(\partial_{xx}u_x) + 2(\partial_y u_y)(\partial_{xy}u_y) + (\partial_x u_y + \partial_y u_x)(\partial_{xx}u_y + \partial_{xy}u_x)\right)\right] \\ &= \frac{\left[(\partial_x u_x)(\partial_{xx}u_x) + (\partial_y u_y)(\partial_{xy}u_y) + \frac{1}{2}(\partial_x u_y + \partial_y u_x)(\partial_{xx}u_y + \partial_{xy}u_x)\right]}{2\sqrt{\frac{1}{2}\left((\partial_x u_x)^2 + (\partial_y u_y)^2\right) + \frac{1}{4}(\partial_x u_y + \partial_y u_x)^2}} \\ \partial_y\dot{\varepsilon} &= \frac{\left[(\partial_x u_x)(\partial_{yx}u_x) + (\partial_y u_y)(\partial_{yy}u_y) + \frac{1}{2}(\partial_x u_y + \partial_y u_x)(\partial_{xy}u_y + \partial_{yy}u_x)\right]}{2\sqrt{\frac{1}{2}\left((\partial_x u_x)^2 + (\partial_y u_y)^2\right) + \frac{1}{4}(\partial_x u_y + \partial_y u_x)^2}}. \end{aligned}$$

For what concerns the *channel*, we have instead:

$$\begin{cases} \rho\dfrac{\partial u_x}{\partial t} = -\partial_x p - K(\partial_x\dot{\varepsilon})(\partial_y u_x) + \overline{\eta}(\partial_{yy}u_x) \\ \qquad 0 = \rho\dfrac{\partial u_y}{\partial t} = -\partial_y p + K(\partial_y\dot{\varepsilon})(\partial_y u_x) + K\dot{\varepsilon}(\partial_{yy}u_x) \end{cases} \tag{5.21}$$

$$\begin{cases} \rho\dfrac{\partial u_x}{\partial t} = -\partial_x p + \overline{\eta}\partial_{yy}u_x \\ 0 = -\partial_y p + \dfrac{K}{2}\dot{\varepsilon}\partial_y(\partial_y u_x)^2 \end{cases} \tag{5.22}$$

i.e. the presence of $\lambda_3 \neq 0$ leads to a non-null pressure gradient in y direction $\partial_y p \neq 0$. In the simple shear however $\dot{\varepsilon}$ is constant and the velocity profile is linear in y so $\partial_{yy}u = 0$, i.e. the solution is independent of λ_3. From the last equation of the system we obtain

$$p(x, y, t) = \frac{K}{2}(\partial_y u_x)^2 + c(x, t)$$

thus, $p(x, y)$ has a parabolic profile along the direction y. Making the derivative in x two times of the first equation of the system we obtain

$$0 = -\partial_{xx}c$$

thus, $c(x, t)$ is a linear function $c(x, t) = Cx + a(t)$, therefore the system becomes

$$\begin{cases} \rho\dfrac{\partial u_x}{\partial t} = -C + \overline{\eta}\partial_{yy}u_x \\ p(x, y, t) = \dfrac{K}{2}(\partial_y u_x)^2 + Cx + a(t). \end{cases} \tag{5.23}$$

We now look for the steady state solution $\partial_t u = \partial_t p = 0$ and adding the hypothesis of stationariety leads to

$$\begin{cases} 0 = -C + \overline{\eta}\partial_{yy}u_x \\ p(x, y) = \dfrac{K}{2}(\partial_y u_x)^2 + Cx + a \end{cases} \tag{5.24}$$

and from the first equation we obtain $u(y) = \frac{C}{2\overline{\eta}}\left(y^2 - 2c_1\right) + c_2$. Let us impose the DBCs $u(0) = u(y) = 0$ getting $c_2 = 0$ e $c_1 = h/2$, and we finally retrieve the solution for the velocity

$$u(y) = \frac{C}{2\overline{\eta}}(y^2 - hy).$$

Instead, to obtain the pressure, just impose the pressure at the centre of the channel (where I have the parabolic peak) at the inlet $p(0, h/2) = 5$ and at the outlet $p(L, h/2) = -5$. Or fix the pressure delta $C = -p_0/L$ and the reference pressure at the centre of the channel $p(L/2, h/2) = 0$, for instance

$$p(x, y) = \frac{k}{2}\left(\frac{C}{\overline{\eta}}\right)^2\left(y - \frac{h}{2}\right)^2 + C(x - \frac{L}{2})$$

obtaining solutions of the form

$$\begin{cases} u(y) = -\dfrac{p_0}{2L\overline{\eta}}(y^2 - hy) \\ p(x,y) = \dfrac{K}{2}\left(\dfrac{p_0}{L\overline{\eta}}\right)^2 \left(y - \dfrac{h}{2}\right)^2 - \dfrac{p_0}{L}(x - \dfrac{L}{2}). \end{cases} \tag{5.25}$$

With $\mathrm{N_{pol}} = 20$ the parameters are $K = 20, p_0 = 10, L = 5, \eta = 10, h = 1$, so the final solutions are

$$\begin{cases} u(y) = -\dfrac{1}{10}(y^2 - hy) \\ p(x,y) = \dfrac{2}{5}\left(y - \dfrac{h}{2}\right)^2 + 2(\dfrac{5}{2} - x) \end{cases} \tag{5.26}$$

while their derivatives are

$$\begin{cases} \partial_y u_x(y) = -\dfrac{1}{10}(2y - h) \\ \partial_y p(x,y) = \dfrac{2}{5}(2y - h) \\ \partial_x p(x,y) = -2. \end{cases} \tag{5.27}$$

Now that we found an analytical solution, we compute the values of the functions $\boldsymbol{u}, p$ in some points and we compare these analytical results with the numerical results found in simulations to check if they are in good agreement

$$\begin{aligned} & u_x(y) = 0 \quad \leftrightarrow \quad y = 0, \quad y = h \\ & \partial_y u_x(y) = 0 \quad \leftrightarrow \quad y = h/2 \quad \rightarrow \quad u_{xmax} = u_x(h/2) = \frac{1}{10}\frac{h^2}{4} = \frac{1}{10} = 0.1 \\ & p(x,y) = 0 \quad \leftrightarrow \quad \frac{2}{5}\left(y - \frac{h}{2}\right)^2 + 2(\frac{5}{2} - x) = 0 \quad \rightarrow \quad x = \frac{1}{5}\left(y - \frac{h}{2}\right)^2 + \frac{5}{2}. \end{aligned}$$

The pressure is geometrically a parabolic cylinder, i.e. the x-y and y-z sections are parabolas, while x-z sections are straight lines. Let us see what happens when we dissect, for example, with vertical lines

$$\begin{aligned} x = \frac{L}{2} \quad \rightarrow \quad & p(\frac{L}{2}, y) = \frac{kp_0}{2L\eta^2}\left(y - \frac{h}{2}\right)^2 \\ & p(\frac{L}{2}, y) = 0 \quad \rightarrow \quad y = \frac{h}{2} \qquad\qquad p(\frac{L}{2}, h) = \frac{kp_0h^2}{8L\eta^2} \\ & \partial_y p(\frac{L}{2}, y) = \frac{kp_0}{2L\eta^2}(2y - h) \qquad\qquad \partial_y p(\frac{L}{2}, y) = 0 \quad \rightarrow \quad y = \frac{h}{2} \end{aligned}$$

$$x = 0 \quad \rightarrow \quad p(0,y) = \frac{kp_0}{2L\eta^2}\left(y - \frac{h}{2}\right)^2 + \frac{p_0}{2}$$

$$p(0,y) = 0 \quad \rightarrow \quad \nexists y \qquad p(0,\frac{h}{2}) = \frac{p_0}{2} \quad p(0,h) = \frac{kp_0h^2}{8L\eta^2} + L > L$$

$$\partial_y p(0,y) = \frac{kp_0}{2L\eta^2}(2y-h) \qquad \partial_y p(0,y) = 0 \quad \rightarrow \quad y = \frac{h}{2}.$$

In the case of the *channel* with Npol=1 the parameters are $K = 20, p_0 = 10, L = 5, \eta = 1.7, h = 1$, therefore

$$\begin{cases} u(y) = -0,588235(y^2 - hy) \\ p(x,y) = 13,8408\left(y - \frac{h}{2}\right)^2 + 2(\frac{5}{2} - x) \end{cases} \tag{5.28}$$

while their derivatives are

$$\begin{cases} \partial_y u_x(y) = -0,588235(2y-h) \\ \partial_y p(x,y) = 13,8408(2y-h) \\ \partial_x p(x,y) = -2. \end{cases} \tag{5.29}$$

And, making some simple test and computations, we verify that analytical and numerical results are, effectively, in good agreement

$$u_x(y) = 0 \quad \rightarrow \quad y = 0, \quad y = h$$

$$\partial_y u_x(y) = 0 \quad \rightarrow \quad y = h/2 \quad \rightarrow \quad u_{xmax} = u_x(h/2) = 0,588235\frac{h^2}{4} = 0,588235$$

$$p(x,y) = 0 \quad \rightarrow \quad 13,8408\left(y - \frac{h}{2}\right)^2 + 2(\frac{5}{2} - x) = 0 \quad \rightarrow \quad x = 6,9204\left(y - \frac{h}{2}\right)^2 + \frac{5}{2}.$$

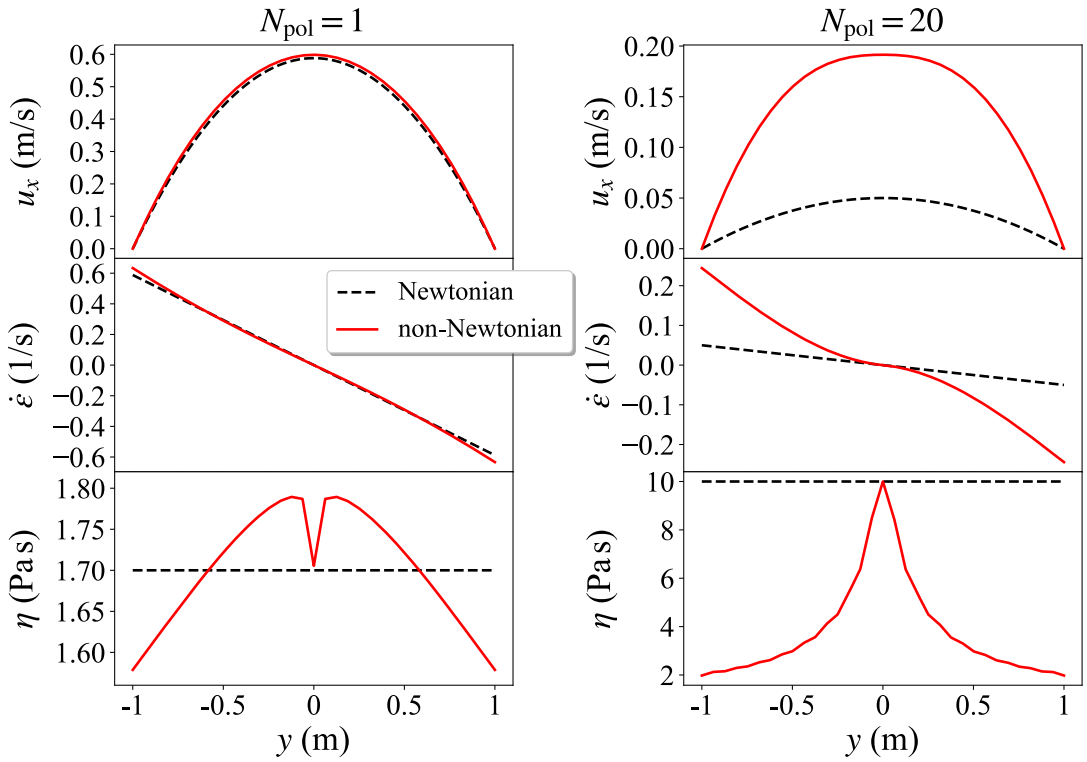

Figure 5.3: *Comparison of the horizontal velocity profile u_x, local deformation rate $\dot{\varepsilon}$, and viscosity η for the flow in a straight channel computed by our multi-scale method with a reference Newtonian solution.* In the case $N_{\text{pol}} = 1$, the non-Newtonian solution is extremely close to the Newtonian one, as expected from the mild rate dependence of the viscosity and the small values of λ_3. In the case $N_{\text{pol}} = 20$, we observe a much larger deviation with a shear-thinning character expected from the rate dependence of the viscosity. The motion in the channel has the property of spacing between various values of $\dot{\varepsilon}$, from $\dot{\varepsilon} = 0$ to $\dot{\varepsilon}_{\text{max}}$. If the pressure field generated for $N_{\text{pol}} = 20$ is large, the viscosity field that is generated is consistent with the figure shown which highlights a strong shear-thinning. The fact that the viscosity curves show approximately the same values at the edges is almost random. And it comes from the fact that u_x and $\dot{\varepsilon}$ for $N_{\text{pol}} = 1$ and $N_{\text{pol}} = 20$ are randomly very similar in values.

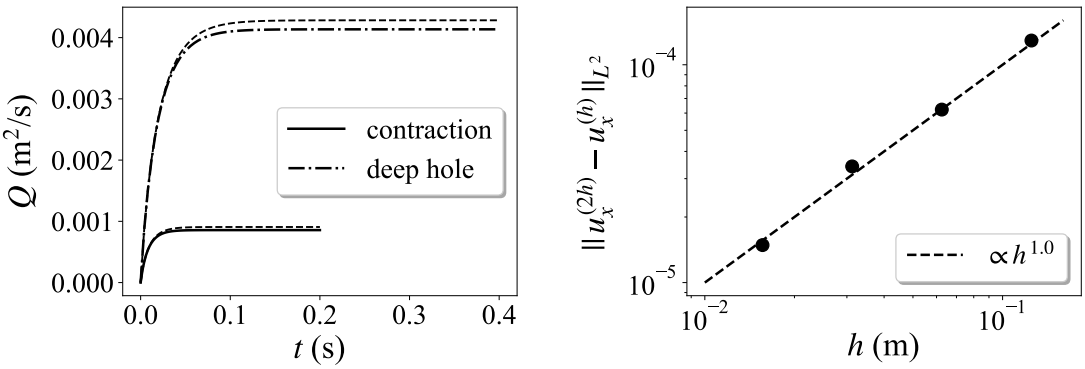

Figure 5.4: *Time convergence of the numerical solution to the steady flow (left) and mesh convergence of the method (right).* The attainment of steady flow conditions is confirmed by the evolution of the flow rate Q through vertical sections of the domain for the contraction and deep hole geometries (left, see legend) the dashed lines show the flow rate produced by the modified non-Newtonian model and highlight a measurable difference with the full model. The incremental correction obtained by successive mesh refinements is measured by the L^2 norm of the difference of the corresponding velocity fields and features a linear scaling with the mesh size parameter h, thus showing convergence of the method in a situation in which all the non-Newtonian contributions are activated.

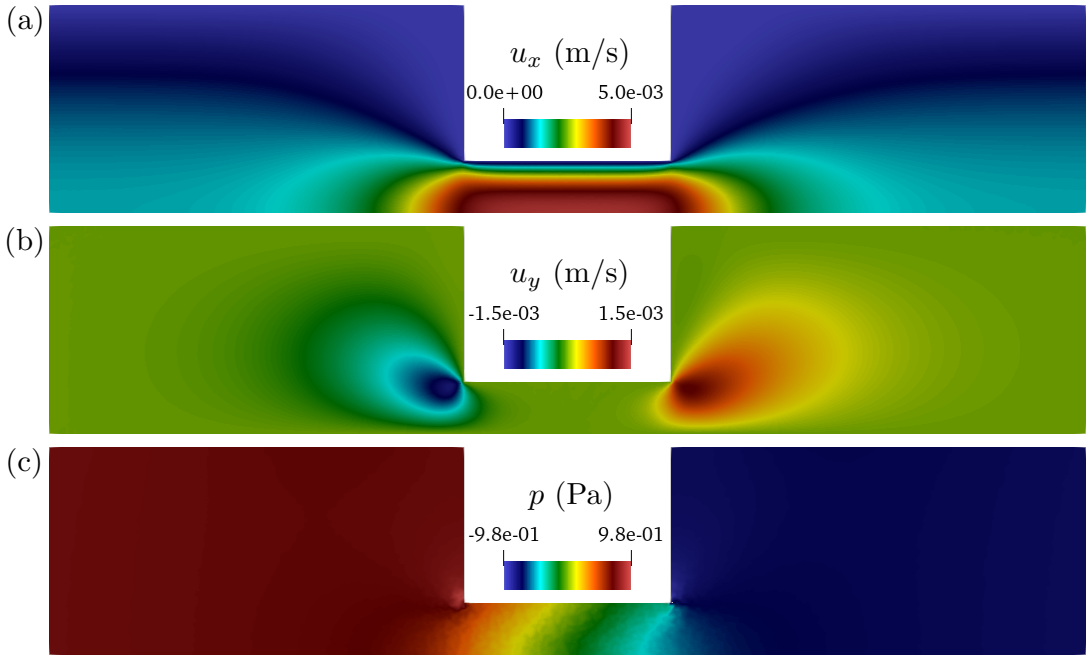

Figure 5.5: *The geometry of the domain induces a flow that features a broad spectrum of local flow types.* (a,b) The two components of the steady-state velocity field, u_x and u_y, in the flow through a contraction show that we are in a stable laminar regime. (c) The pressure field features oblique isolines due to the presence of normal stress differences.

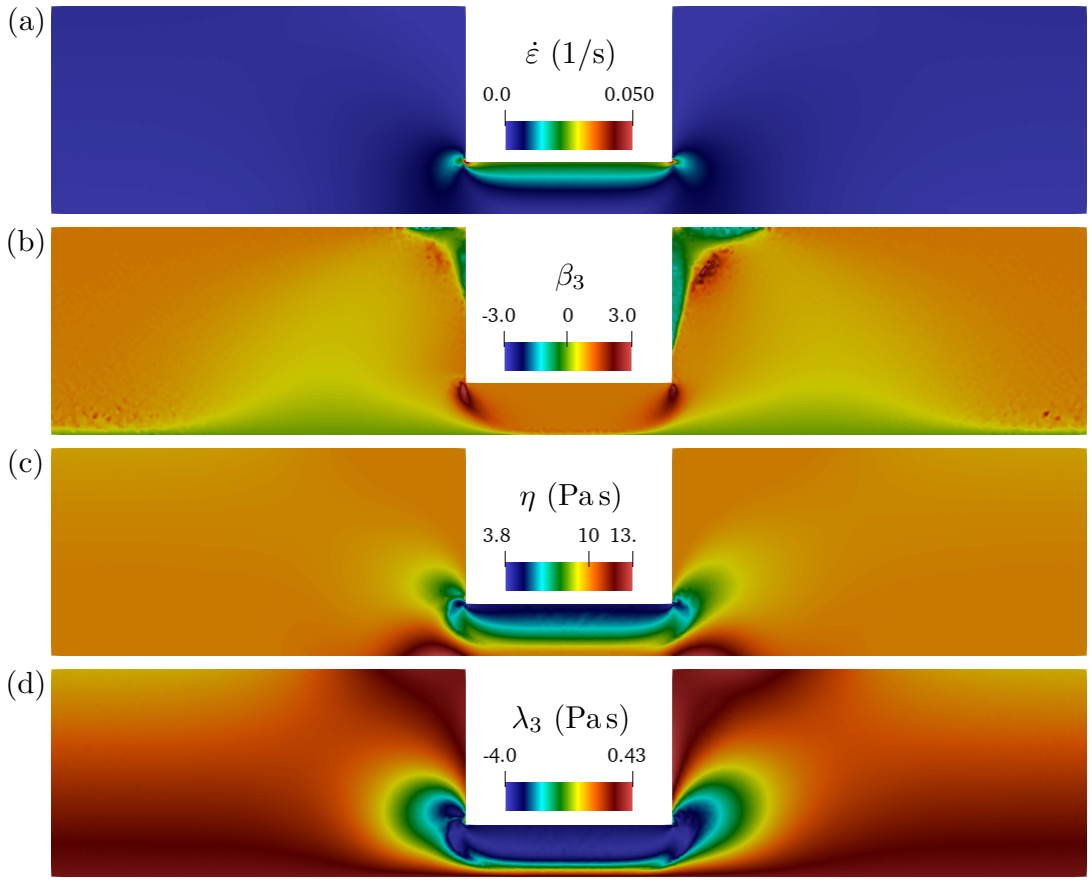

Figure 5.6: *The non-uniform flow type in complex flows can affect significantly the rheological response.* We measured (a) the deformation rate $\dot{\varepsilon}$ and (b) the local flow type β_3 in the flow through a contraction of a polymeric fluid ($N_{\text{pol}} = 20$) and computed the local values of the material parameters (c) η and (d) λ_3. In this case, they are strongly affected by changes in the flow type on top of the variations due to the deformation rate.

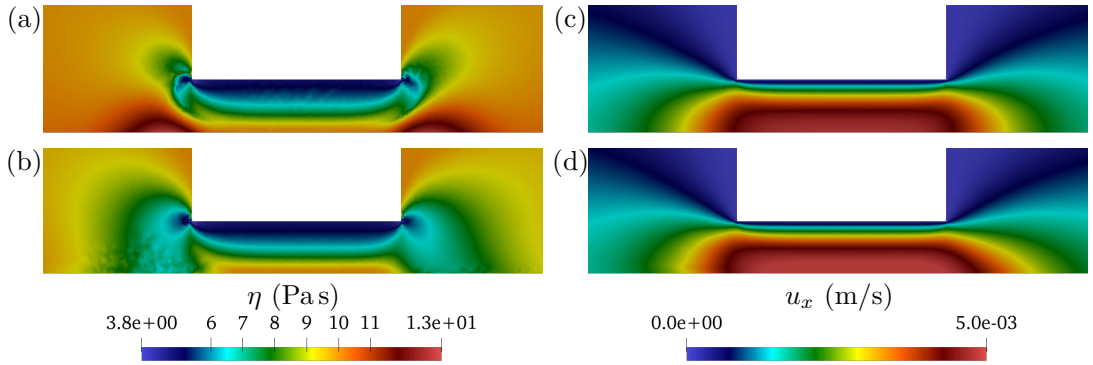

Figure 5.7: *The dependence of the stress on the local flow type must be taken into account to correctly predict the fluid behavior.* We compare the steady-state viscosity η and horizontal velocity u_x nearby the contraction, computed with (a,c) the full non-Newtonian model and (b,d) the modified one. The viscosity in the modified model presents a very different profile in the extensional and mixed flow regions, nearby entrance and exit of the restriction. This influences the velocity field, which features a clear asymmetry due to the overemphasized role of normal stress differences in the modified model.

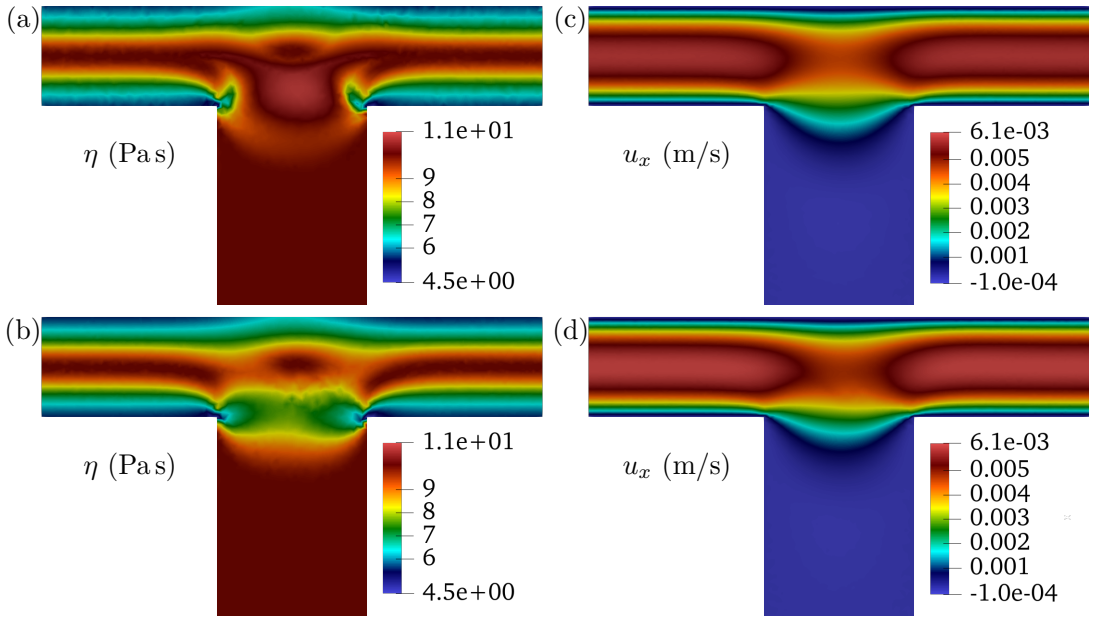

Figure 5.8: *Also in the flow past a deep hole the presence of mixed and extensional flow regions requires a proper treatment of the flow-type dependence of the stress.* We compare the steady-state viscosity η and horizontal velocity u_x computed with (a,c) the full non-Newtonian model and (b,d) the modified one. The viscosity appears to be significantly different right above the deep hole. The velocity depression is shifted rightward and the flow is globally faster.

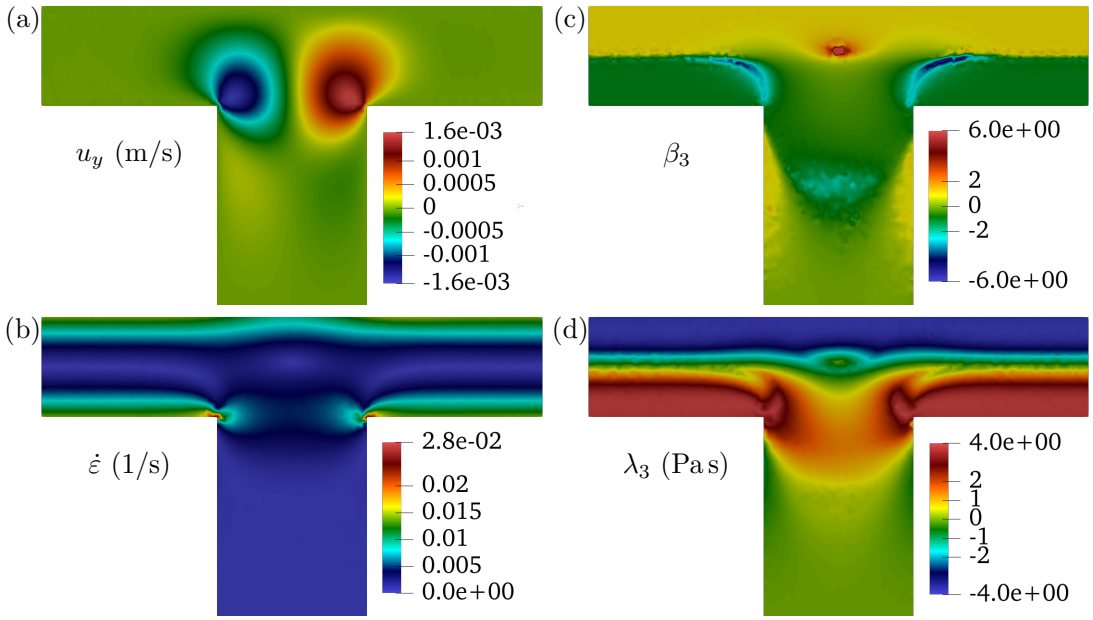

Figure 5.9: *The flow past a deep hole features a complex distribution of local flow types with a consequent variation of the material response.* (a) From the component u_y of the velocity we can see the region where the deep hole modifies the flow in the upper channel. (b,c) The deformation rate $\dot{\varepsilon}$ and the flow-type parameter β_3 highlight the presence of mixed flows and high-vorticity regions. (d) The values of λ_3 across the domain are a direct consequence of the non-Newtonian rheology and the complexity of the flow.

6

NEMD simulations with PMF package

NEMD simulations of mixed flows at the micro-scale have been performed using the software package `PMF` (Planar Mixed Flows), implemented in C++ taking inspiration, for the architecture of the code (but not for the algorithm) from the package `UEF` developed by David Nicholson [51]. The implemented algorithm is an extension of the Kraynik & Reinelt work [38] to the mixed flows. The `PMF` package has been tested with the stable version of LAMMPS [53, lammps.sandia.gov] of Oct 29th 2020.

6.1 Settings

We considered a simple model for polymeric chains in a three-dimensional computational domain with periodic boundary conditions and undergoing mixed motions. Different types of mixed motions were carried out for values of the flow parameter $\beta \in \{0.1, 0.2, 0.3, 0.4, 0.5, 0.6, 0.7, 0.8, 0.9\}$. We considered values of the deformation rate $\dot{\varepsilon}$ ranging from 0.001 s^{-1} to 0.22 s^{-1}. The averaged temperature of the fluctuations around the mean motion has been fixed at $T = 1\frac{k_B}{\varepsilon}$ while the density of the system at $\rho = 0.8\frac{m}{\sigma^2}$. The total number of particles involved depends on the flow parameter β. The proportion of the simulation box also varies according to the flow parameter β, as expressed by the equation (4.11) in Chap. 4. The shorter sides are always 10.77217σ while the longer sides range from 10.77217σ for $\beta = 0$ to 51.967008σ for $\beta = 0.9$. The equilibration times vary a lot, both on the basis of $\dot{\varepsilon}$ and β, so we do not think it appropriate to report them here. At each time, the average stress given as output by LAMMPS is projected onto the basis tensors through the formulae (5.3) and these projections are averaged over time. Finally,

a mean over all initial configurations is taken.

Fixed β, for each value of $\dot{\varepsilon}$ we performed 21 simulations with different initial configurations of the particles. The average velocity field is imposed by deforming the computational box and the canonical ensemble statistics of the velocity fluctuations is achieved via the Nosé–Hoover thermostat [24]. It has not been possible to realize the simple shear motion with the `PMF` package because the method has a singularity at $\beta = 1$, while it has been possible to simulate the planar extensional motion by simply setting $\beta = 0$. Thus, we used the NEMD data shown in the Chapter 5 obtained with the `fix deform` routine of `LAMMPS`, as a reference for $\beta = 1$. Polymers are modeled through a FENE+WCA potential, as usual and as explained in Chapter 3. We discuss results for $N_{\mathrm{pol}} = 20$, i.e. polymers with 20 bonded monomers in each chain.

6.2 Average stress coefficients

At each time, the average stress $\boldsymbol{\sigma}$ of the system was given as output by `LAMMPS` and has been projected onto the basis tensors illustrated in Chapter 2 to obtain the material functions of eq. (5.3). These projections are then averaged over time. Finally, an arithmetic mean over all initial configurations has been taken. Let us take a detailed look at the trends of the coefficients obtained, as $\dot{\varepsilon}$ and β vary.

6.2.1 Viscosity and reorientation of eigenvectors

In the top panel of Figure 6.1 we presented data about the dependence of the material coefficient $C_D = 2\dot{\varepsilon}\eta(\dot{\varepsilon}, \beta_3)$ (linked to the generalized viscosity η) on the strain rate $\dot{\varepsilon}$, for each value of β. Each curve is monotonically increasing in the strain rate $\dot{\varepsilon}$ while monotonically decreasing in the flow-type parameter β, as we expected from MD results of Chapter 5 (Sec. 5.2.2) that show higher values for the viscosity in extension than in simple shear.

While the bottom panel of Figure 6.1 shows the trend of the function $C_{G_3} = 2\dot{\varepsilon}\lambda_3(\dot{\varepsilon}, \beta_3)$, related to non-Newtonian effects due to some reorientation in eigenvectors of the stress $\boldsymbol{\sigma}$ (w.r.t. eigenvectors of the strain tensor $\mathbf{D}$) in the fluid. This coefficient takes on non-zero values apart for $\beta = 0$, as we expected, because we know that for polymers consisting of chains of length $\mathrm{N_{pol}} = 20$ the reorientation takes place if a component of simple shear is present. $\mathrm{C_{G_3}}$ assumes negative values (this depends on the sign of β) and each single curve, for β fixed, displays a monotonic decreasing trend with respect to $\dot{\varepsilon}$ (or increasing in absolute value).

A curious thing to note is that the material function is not monotonic with respect to the flux parameter β because it is increasing up to a value $\beta = 0.6$, while it is decreasing from $\beta = 0.7$ to $\beta = 1$. Initially, we considered the trend of $\eta = \frac{C_D}{2\dot{\varepsilon}}$, but dividing by very small $\dot{\varepsilon}$, of the order of 10^{-3} or 10^{-2} would amplify the error and deviate η from the null value it must assume near $\dot{\varepsilon} = 0$. For this reason we then chose to display the coefficients in their full form. We looked at the trend of η in β and noted again the monotonic behavior in β, but this representation shows a non-monotonic trend in $\dot{\varepsilon}$: for $0.0 \leq \beta \leq 0.7$ (β closer to extension) there is a clear

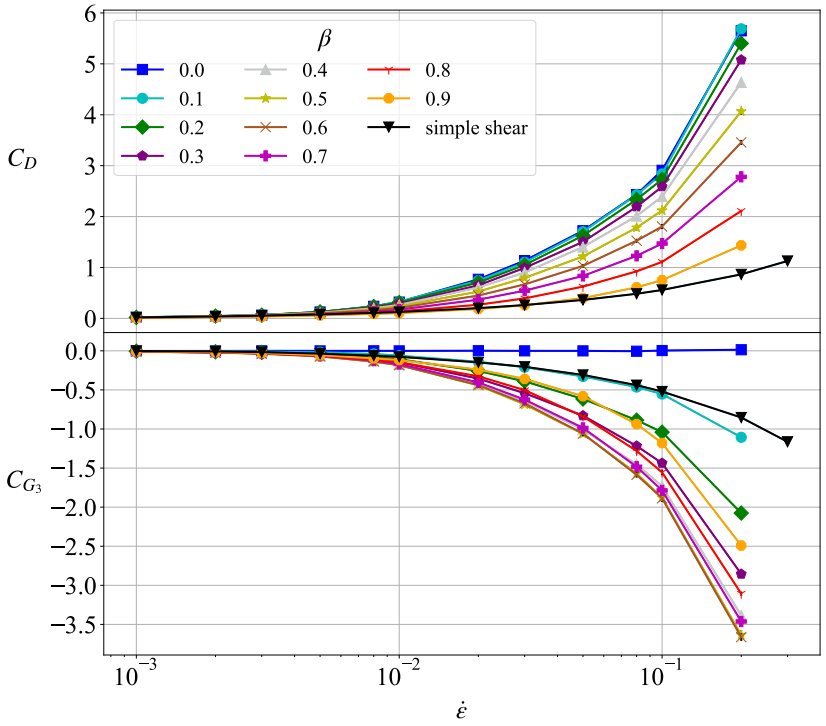

Figure 6.1: *The polymeric fluid displays rate dependence and strong flow-type dependence of the stress coefficients.* We compare the NEMD data for the stress coefficients $\mathrm{C_D}$ (top) and $\mathrm{C_{G_3}}$ (bottom) against $\dot{\varepsilon}$ obtained for the polymeric case with $N_{\mathrm{pol}} = 20$ under mixed motions, i.e. for $0 < \beta < 1$. The former displays monotonic increasing trends both in $\dot{\varepsilon}$ and β, while the latter displays decreasing monotonic trend in $\dot{\varepsilon}$ and non monotonic behavior in β. The presence of a strong flow-type dependence originates from the different conformations of the long molecules.

zone of shear-thickening for $0s^{-1} \leq \dot{\varepsilon} \leq 2 \cdot 10^{-2}s^{-1}$, followed by a zone of shear-thinning for $2 \cdot 10^{-2}s^{-1} \leq \dot{\varepsilon} \leq 1 \cdot 10^{-1}s^{-1}$ and a clear final hint of shear-thickening. This behaviour is more pronounced for betas closer and closer to $\beta = 0$. While for β approaching 1 the classical shear-thinning behavior of polymeric fluids (qualitatively similar to that of monomeric fluids) under simple shear is displayed. This spectrum of behavior is due to the different shapes assumed by conformation of molecules in the different types of motion (spherical in simple shear, elongated in extensional, both in mixed, ...). These data are coherent with what we expected from the NEMD data of Chapter 5. We looked also at λ_3, with its non-monotonic behavior. The elastic effects generated by the bonds are crucial in this case and when a little component of simple shear is present, normal stress differences are generated and displayed by nonvanishing values of λ_3. Even if not visible (because small), the error bars are reported in Fig. 6.1. Furthermore, the figure clearly shows that in the limit of $\dot{\varepsilon} \to 0$ all motions have the same values for the coefficients.

With the package `PMF` we were able to obtain reliable data in the range of flow parameter $0 \leq \beta < 1$ and for strain rates $0s^{-1} < \dot{\varepsilon} < 0\,22s^{-1}$ (we represented only up to $\dot{\varepsilon} = 0\,1s^{-1}$ for graphical convenience) that could not be explored with the techniques already implemented in `LAMMPS`. In Figures 6.2 and 6.3 we represented the colorplot of the surfaces of NEMD data that we have been able to produce.

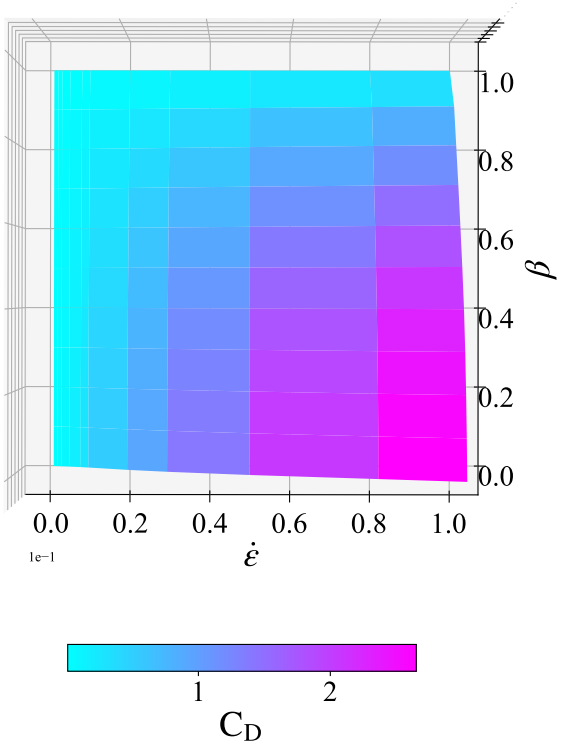

Figure 6.2: The figure shows a different representation of NEMD data previously seen about the viscosity coefficient C_D obtained for $0 < \beta < 1$ and $0s^{-1} < \dot{\varepsilon} < 0\,22s^{-1}$ with a colorplot of its values.

6.2.2 The other coefficients

We also represented the remaining coefficients C_E, C_{G1}, C_{G2} of the three dimensional decomposition, related, respectively, to the anisotropy in the distribution of the stress along eigenvectors and reorientation of the eigenvectors of $\boldsymbol{\sigma}$ (w.r.t those of $\mathbf{D}$) in the orthogonal planes to the x-axis and the y-axis, see Figure 6.4.

As we expected, the coefficients C_{G_1} and C_{G_2} fluctuate around zero, because, since the flow develop in $x - y$ plane, there is no reorientation of the eigenvectors in these directions, but only in the flow plane. Instead, anisotropy is present, as can be seen from the non-zero coefficient

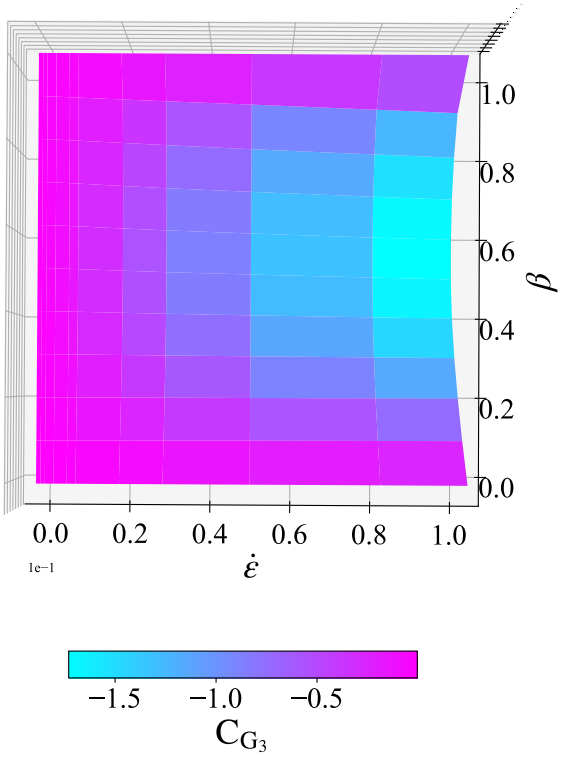

Figure 6.3: The figure shows a different representation of NEMD data previously seen about the viscosity coefficient C_{G_3} obtained for $0 < \beta < 1$ and $0s^{-1} < \dot{\varepsilon} < 0\,22s^{-1}$ with a colorplot of its values.

C_E. It shows an increasing (decreasing in absolute value) monotonous trend with the parameter β, and this is what we expected.

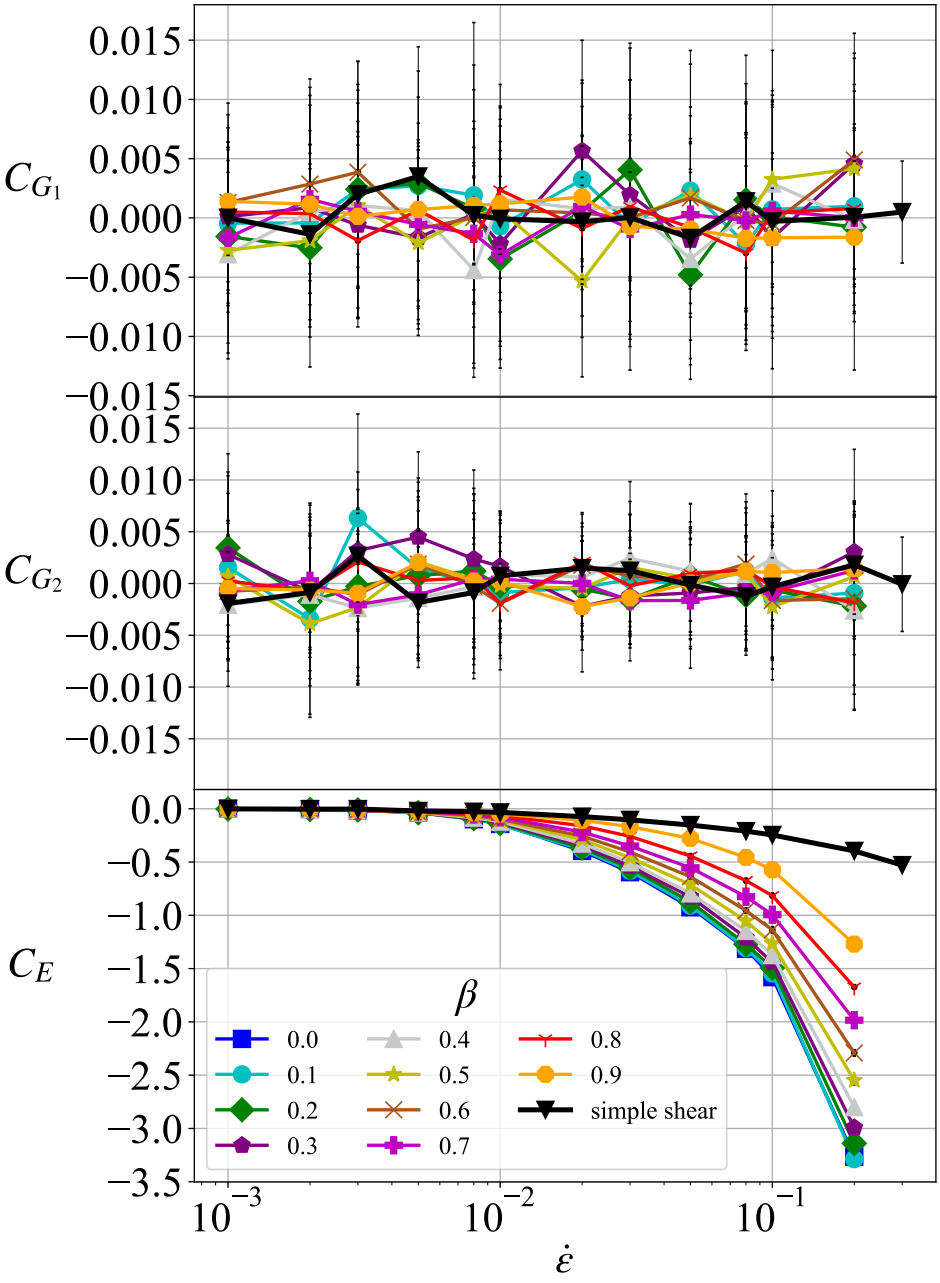

Figure 6.4: NEMD data about the material functions $\mathrm{C_{G_1}}(\dot{\varepsilon},\beta), \mathrm{C_{G_2}}(\dot{\varepsilon},\beta)$ and $\mathrm{C_E}(\dot{\varepsilon},\beta)$ of a polymeric fluid with chain length $\mathrm{N_{pol}} = 20$ under different mixed flows. Each colored curve represents a fixed value of β. As expected from the planarity of the motion, he reorientation coefficients $\mathrm{C_{G_1}}$ and $\mathrm{C_{G_2}}$ fluctuates around zero, while $\mathrm{C_E}$ is monotonically increasing with β.

7 Conclusions

A multi-scale method for the simulation of planar flows in arbitrary geometries for complex fluids has been proposed and tested. This is based on collecting the results of micro-scale simulations according to a general decomposition of the stress [25] that allows to correctly align its different components in flows that display a broad spectrum of local flow types. And, subsequently, to combine these data with macro-scale continuum equations to achieve a data-driven prediction of complex flows. We have shown that a proper treatment of the flow-type dependence, that was missing in previous multi-scale methods (exclusively focused on simple shear rheology) is essential to capture the macroscopic dynamics.

In our case, the micro-scale simulations are Non-Equilibrium Molecular Dynamics (NEMD) simulations of polymeric chains with internal FENE bonds and an effective repulsive Weeks-Chandler-Andersen interaction potential. We performed these simulations imposing simple shear and planar extension as average kinematic conditions under which we evaluate the stress response. From these, we built the rheological functions in mixed flows by means of a simple interpolation and extrapolation procedure. Nevertheless, our coupling scheme does not rely on a specific simulation strategy neither at the micro-scale nor at the macro-scale, but any other methods can in principle be employed. The macroscopic simulation of the continuum was implemented with a well-established mixed finite element method based on P_2-P_0 elements for the velocity-pressure pair to deal with the incompressibility constraint and a semi-implicit time integration scheme.

Polymeric fluids are well known to display a significant degree of flow-type dependence in their rheological properties. In fact, the different average conformation of the long molecular

chains in simple shear and extensional flows causes the same material to show opposite trends in the dependence of the viscosity on the rate of deformation. Our micro-scale simulation reproduced this feature. Hence, we were able to assess the relevance of properly taking into account the flow type dependence of the stress in the material response and, thus, the macro-scale simulation. From the results obtained with our multi-scale approach in three complex geometries (the straight channel, the contraction channel and the deep-hole), it is clear that the predictions of a model that suppresses the flow-type dependence are not reliable.

In fluids composed by molecules with longer microscopic relaxation times, it may happen that the local flow type experienced by a fluid element changes fast along streamlines. The method that we presented can in principle be extended to take this into account by devising MD simulations for which the flow type of the imposed background motion is slowly varying. The macroscopic material functions would then depend also on the derivative along streamlines of the flow-type parameter. Other directions for future work are the testing of our method in parameter ranges where elastic instabilities may be observed, that may lead to the presence of highly oscillatory material coefficients in space and time, and the implementation of an on-the-fly coupling between macro-scale and micro-scale simulations, to be able to sample the space of kinematic conditions in a problem-driven fashion.

In view of the impact on macroscopic flows in non-viscometric geometries of the local flow conditions, we expanded the micro-scale simulations to obtain data under mixed flows and we plan to extend our investigation also to rotational flow conditions in which we will have different orders of problems because the streamlines are elliptical and the method illustrated in the thesis cannot be directly applied to such case. The extension to mixed flows required the implementation of a suitable generalization of the Kraynik–Reinelt (KR) periodic boundary conditions for non-equilibrium molecular dynamics simulations.

In our MD simulations of steady, homogeneous flows, the mixed flow is imposed through the deformation of the simulation box, and can happen that image particles become arbitrarily close, causing a stop of the simulation because the compatibility requirement is violated. Our boundary conditions avoid this problem for intermediate flows between simple shear and planar extension. We found reproducibility conditions of the system lattice of points: specific orientation and proportions of the unit cell lead to periodic behavior (i.e. the initial state boundaries are recovered) with the minimum period. In correspondence to such period the box must be re-initialized (in a way that conserves image locations) to proceed for another equal period of time. Thus, through careful choice of the initial simulation box and by periodically remapping it, we have been able to theoretically extend indefinitely the time of the simulations of planar mixed flows. PBCs for Planar Mixed Flows have also been implemented by us in a software package named `PMF` for NEMD simulations. The package is written in C++ and is planned to be inserted in `LAMMPS`.

Bibliography

[1] G. Astarita. Objective and generally applicable criteria for flow classification. *Journal of Non-Newtonian Fluid Mechanics*, 6(1):69–76, 1979.

[2] Y. Bar-Yam. Separation of scales: Why complex systems need a new mathematics, in. *Cambridge, MA*, 2015.

[3] A. Baranyai and P. T. Cummings. Steady state simulation of planar elongation flow by nonequilibrium molecular dynamics. *The Journal of chemical physics*, 110(1):42–45, 1999.

[4] M. Borg, D. Lockerby, and J. Reese. Fluid simulations with atomistic resolution: a hybrid multiscale method with field-wise coupling. *J. Comput. Phys.*, 255:149–165, 2013.

[5] M. Borg, D. Lockerby, and J. Reese. A hybrid molecular–continuum method for unsteady compressible multiscale flows. *J. Fluid Mech.*, 768:388–414, 2015.

[6] F. Brezzi and M. Fortin. *Mixed and hybrid finite element methods*, volume 15. Springer Science & Business Media, 2012.

[7] T. Cochrane, K. Walters, and M. Webster. On newtonian and non-newtonian flow in complex geometries. *Philosophical Transactions of the Royal Society of London. Series A, Mathematical and Physical Sciences*, 301(1460):163–181, 1981.

[8] B. D. Coleman, H. Markovitz, and W. Noll. *Viscometric flows of non-Newtonian fluids: theory and experiment*, volume 5. Springer Science & Business Media, 2012.

[9] M. J. Crochet, A. R. Davies, and K. Walters. *Numerical simulation of non-Newtonian flow*. Elsevier, 2012.

[10] P. J. Daivis and B. Todd. A simple, direct derivation and proof of the validity of the sllod equations of motion for generalized homogeneous flows. *J. Chem. Phys.*, 124(19):194103, 2006.

[11] M. Dobson. Periodic boundary conditions for long-time nonequilibrium molecular dynamics simulations of incompressible flows. *J. Chem. Phys.*, 141(18):184103, 2014.

[12] A. Donev, J. B. Bell, A. L. Garcia, and B. J. Alder. A hybrid particle-continuum method for hydrodynamics of complex fluids. *SIAM J. Multiscale Model. Simul.*, 8:871–911, 2010.

[13] W. E. Seamless multiscale modeling of complex fluids using fiber bundle dynamics. *Commun. Math. Sci.*, 5(4):1027–1037, 2007.

[14] W. E and B. Enquist. The heterogeneous mutli-scale method. *Commun. Math. Sci.*, 1: 87–133, 2003.

[15] W. E and X. Li. Analysis of the heterogeneous multiscale method for gas dynamics. *Methods Appl. Anal.*, 11(4):557–572, 12 2004.

[16] W. E and J. Lu. Seamless multiscale modeling via dynamics on fiber bundles. *Commun. Math. Sci.*, 5(3):649–663, 09 2007.

[17] W. E, P. Ming, and P. Zhang. Analysis of the heterogeneous multiscale method for elliptic homogenization problems. *J. American Math. Soc.*, 18(01):121–157, 2005.

[18] W. E, W. Ren, and E. Vanden-Eijnden. A general strategy for designing seamless multiscale methods. *J. Comput. Phys.*, 228(15):5437–5453, 2009.

[19] D. J. Evans and G. Morriss. Nonlinear-response theory for steady planar couette flow. *Physical Review A*, 30(3):1528, 1984.

[20] D. A. Fedosov and G. E. Karniadakis. Triple-decker: Interfacing atomistic–mesoscopic–continuum flow regimes. *J. Comput. Phys.*, 228(4):1157–1171, 2009.

[21] D. A. Fedosov, G. E. Karniadakis, and B. Caswell. Dissipative particle dynamics simulation of depletion layer and polymer migration in micro- and nanochannels for dilute polymer solutions. *J. Chem. Phys.*, 128(14):144903, 2008.

[22] K. Feigl, M. Laso, and H. C. Oettinger. Connffessit approach for solving a two-dimensional viscoelastic fluid problem. *Macromolecules*, 28(9):3261–3274, 1995.

[23] E. G. Flekkoy, G.Wagner, and J. Feder. Hybrid model for combined particle and continuum dynamics. *Europhys. Lett.*, 271:271–276, 2000.

[24] D. Frenkel and B. Smit. *Understanding molecular simulation: from algorithms to applications*, volume 1. Elsevier, 2001.

[25] G. G. Giusteri and R. Seto. A theoretical framework for steady-state rheometry in generic flow conditions. *Journal of Rheology*, 62(3):713–723, 2018.

[26] M. E. Gurtin. *An introduction to continuum mechanics*. Academic press, 1982.

[27] R. Hartkamp, B. Todd, and S. Luding. A constitutive framework for the non-newtonian pressure tensor of a simple fluid under planar flows. *The Journal of chemical physics*, 138 (24):244508, 2013.

[28] W. G. Hoover. Nonequilibrium molecular dynamics. *Annual Review of Physical Chemistry*, 34(1):103–127, 1983.

[29] W. G. Hoover. *Computational statistical mechanics*. Elsevier, 2012.

[30] M. Hulsen, A. Van Heel, and B. Van Den Brule. Simulation of viscoelastic flows using brownian configuration fields. *Journal of Non-Newtonian Fluid Mechanics*, 70(1-2):79–101, 1997.

[31] T. A. Hunt. Periodic boundary conditions for the simulation of uniaxial extensional flow. *arXiv preprint arXiv:1310.3905*, 2013.

[32] T. A. Hunt. Periodic boundary conditions for the simulation of uniaxial extensional flow of arbitrary duration. *Molecular Simulation*, 42(5):347–352, 2016.

[33] T. A. Hunt, S. Bernardi, and B. Todd. A new algorithm for extended nonequilibrium molecular dynamics simulations of mixed flow. *The Journal of chemical physics*, 133(15): 154116, 2010.

[34] D. J Evans and G. P Morriss. *Statistical mechanics of nonequilbrium liquids*. ANU Press, 2007.

[35] I. G. Kevrekidis and G. Samaey. Equation-free multiscale computation: Algorithms and applications. *Ann. Rev. Phys. Chem.*, 60(1):321–344, 2009.

[36] I. G. Kevrekidis, C. W. Gear, J. M. Hyman, P. G. Kevrekidis, O. Runborg, and C. Theodoropoulos. Equation-free coarse-grained, multiscale computation: enabling microscopic simulators to perform system-level analysis. *Commun. Math. Sci.*, 1(4):715–762, 2003.

[37] I. G. Kevrekidis, C. W. Gear, and G. Hummer. Equation-free: The computer-aided analysis of complex multiscale systems. *AIChE J.*, 50(7):1346–1355, 2004.

[38] A. Kraynik and D. Reinelt. Extensional motions of spatially periodic lattices. *International journal of multiphase flow*, 18(6):1045–1059, 1992.

[39] A. J. Ladd and W. G. Hoover. Lorentz gas shear viscosity via nonequilibrium molecular dynamics and boltzmann's equation. *Journal of statistical physics*, 38(5):973–988, 1985.

[40] L. Landau and E. Lifshitz. *Fluid mechanics*, volume 6. Pergamon Press, 1987.

[41] H. P. Langtangen and A. Logg. *Solving PDEs in python: the FEniCS tutorial I*. Springer Nature, 2016.

[42] R. G. Larson. *The structure and rheology of complex fluids*, volume 150. Oxford university press New York, 1999.

[43] M. Laso and H. C. Öttinger. Calculation of viscoelastic flow using molecular models: the connffessit approach. *Journal of Non-Newtonian Fluid Mechanics*, 47:1–20, 1993.

[44] A. Lees and S. Edwards. The computer study of transport processes under extreme conditions. *Journal of Physics C: Solid State Physics*, 5(15):1921, 1972.

[45] B. Leimkuhler and C. Matthews. *Molecular Dynamics.* Springer, 2016.

[46] A. Logg and G. N. Wells. Dolfin: Automated finite element computing. *ACM Transactions on Mathematical Software (TOMS)*, 37(2):1–28, 2010.

[47] R. M. Miller, J. P. Singh, and J. F. Morris. Suspension flow modeling for general geometries. *Chemical Engineering Science*, 64(22):4597–4610, 2009.

[48] M. Minale, P. Moldenaers, and J. Mewis. Effect of shear history on the morphology of immiscible polymer blends. *Macromolecules*, 30(18):5470–5475, 1997.

[49] M. Neumann, S. Huang, D. E. Marthaler, and K. Kersting. pygps: a python library for gaussian process regression and classification. *J. Mach. Learn. Res.*, 16(1):2611–2616, 2015.

[50] P. Neumann, W. Eckhardt, and H.-J. Bungartz. Hybrid molecular-continuum methods: from prototypes to coupling software. *Comput. Math. Appl.*, 67(2):272–281, 2014.

[51] D. A. Nicholson and G. C. Rutledge. Molecular simulation of flow-enhanced nucleation in n-eicosane melts under steady shear and uniaxial extension. *The Journal of chemical physics*, 145(24):244903, 2016.

[52] N. Phan-Thien and N. Mai-Duy. *Understanding viscoelasticity: an introduction to rheology.* Springer, 2017.

[53] S. Plimpton. Fast parallel algorithms for short-range molecular dynamics. *J. Comput. Phys.*, 117(1):1–19, 1995.

[54] P. Schunk and L. Scriven. Constitutive equation for modeling mixed extension and shear in polymer solution processing. *Journal of rheology*, 34(7):1085–1119, 1990.

[55] R. Seto and G. G. Giusteri. Normal stress differences in dense suspensions. *Journal of Fluid Mechanics*, 857:200–215, 2018.

[56] S. Stalter, L. Yelash, N. Emamy, A. Statt, M. Hanke, M. Lukáčová-Medvid'ová, and P. Virnau. Molecular dynamics simulations in hybrid particle-continuum schemes: Pitfalls and caveats. *Comput. Phys. Commun.*, 224:198–208, 2018.

[57] R. Tanner. A theory of die-swell. *Journal of Polymer Science Part A-2: Polymer Physics*, 8(12):2067–2078, 1970.

[58] F. Tedeschi, G. G. Giusteri, L. Yelash, and M. Lukáčová-Medvid'ová. A multi-scale method for complex flows of non-newtonian fluids. *Mathematics in Engineering*, 4(6):1–22, 2022. doi: 10.3934/mine.2022050.

[59] A. P. Thompson, S. J. Plimpton, and W. Mattson. General formulation of pressure and stress tensor for arbitrary many-body interaction potentials under periodic boundary conditions. *The Journal of chemical physics*, 131(15):154107, 2009.

[60] R. L. Thompson and P. R. S. Mendes. Considerations on kinematic flow classification criteria. *Journal of non-newtonian fluid mechanics*, 128(2-3):109–115, 2005.

[61] B. Todd and P. J. Daivis. Nonequilibrium molecular dynamics simulations of planar elongational flow with spatially and temporally periodic boundary conditions. *Physical review letters*, 81(5):1118, 1998.

[62] B. D. Todd and P. J. Daivis. *Nonequilibrium molecular dynamics: theory, algorithms and applications*. Cambridge University Press, 2017.

[63] C. K. Williams and C. E. Rasmussen. Gaussian processes for regression. *Advances in Neural Information Processing Systems*, 1996.

[64] C. K. Williams and C. E. Rasmussen. *Gaussian processes for machine learning*, volume 2 (3). MIT press Cambridge, MA, 2006.

[65] S. Yasuda and R. Yamamoto. Multiscale modeling and simulation for polymer melt flows between parallel plates. *Phys. Rev. E*, 81(3), 2010.